

# Predicting Frictional Properties of Graphene Kirigami Using Molecular Dynamics and Neural Networks

*Designs for a negative friction coefficient.*

Mikkel Metzsch Jensen



Thesis submitted for the degree of  
Master in Computational Science: Materials Science  
60 credits

Department of Physics  
Faculty of mathematics and natural sciences

UNIVERSITY OF OSLO

Spring 2023



# Predicting Frictional Properties of Graphene Kirigami Using Molecular Dynamics and Neural Networks

*Designs for a negative friction coefficient.*

Mikkel Metzsch Jensen





© 2023 Mikkel Metzsch Jensen

Predicting Frictional Properties of Graphene Kirigami Using Molecular Dynamics and Neural Networks

<http://www.duo.uio.no/>

Printed: Reprocentralen, University of Oslo

# Abstract

Abstract.



# Acknowledgments

Acknowledgments.



# List of Symbols

$F_N$  Normal force (normal load)



# Acronyms

**AFM** Atomic Force microscope. 21, 22, 23, 25

**CM** Center of Mass. 19, 20, 34, 35

**FFM** Friction Force Microscopes. 21, 22, 23, 24, 25

**FK** Frenkel-Kontorova. 11, 16

**FKT** Frenkel-Kontorova–Tomlinson. 11, 20

**GAN** Generative Adversarial Networks. 2

**GS** Ground State. 16, 18

**LJ** Lennard-Jones. 39

**MD** Molecular Dynamics. 1, 2, 3, 4, 10, 11, 12, 14, 23, 24, 25, 26, 29, 30, 33, 41, 44, 51, 52, 53

**ML** Machine Learning. 2, 30, 54

**PT** Prandtl–Tomlinson. 11

**SFA** Surface force apparatus. 22, 23

**SFM** Scanning Force Microscopies. 21

**SPM** Scanning Probe Microscopy. 21

**std** Standard Deviation. 36, 37, 40, 42



# Contents

<b>1</b>	<b>Introduction</b>	<b>1</b>
1.1	Motivation . . . . .	1
1.2	Goals . . . . .	3
1.3	Contributions . . . . .	3
1.4	Thesis structure . . . . .	4
<b>I</b>	<b>Background Theory</b>	<b>5</b>
<b>2</b>	<b>Friction</b>	<b>7</b>
2.1	Friction across scales . . . . .	7
2.2	Macroscale . . . . .	7
2.2.1	Amontons' law . . . . .	7
2.3	Microscopic scale . . . . .	9
2.3.1	Asperity theories . . . . .	9
2.4	Nanoscale — Atomic scale . . . . .	10
2.4.1	Prandtl–Tomlinson . . . . .	11
2.4.1.1	Thermal activation . . . . .	12
2.4.1.2	Sliding speed . . . . .	14
2.4.1.3	Tip mass . . . . .	15
2.4.1.4	Friction Regimes: Smooth Sliding, Single Slip, and Multiple Slip . . . . .	15
2.4.2	Frenkel-Kontorova . . . . .	16
2.4.2.1	Commensurability . . . . .	16
2.4.2.2	Velocity resonance . . . . .	19
2.4.3	Frenkel-Kontorova-Tomlinson . . . . .	20
2.4.4	Shortcomings of reduced-models . . . . .	20
2.4.5	Experimental procedures . . . . .	21
2.4.5.1	Scanning Probe Microscopy . . . . .	21
2.4.5.2	Surface Force Apparatus . . . . .	22
2.5	Summary of previous results . . . . .	22
2.6	Research questions . . . . .	26
<b>II</b>	<b>Simulations</b>	<b>27</b>
<b>3</b>	<b>Pilot study</b>	<b>29</b>
3.1	Friction simulation parameters . . . . .	29
3.2	Force traces . . . . .	30
3.2.1	Force oscillations . . . . .	30
3.2.2	Decompositions . . . . .	34
3.2.3	Center of mass path . . . . .	34
3.3	Defining metrics for friction . . . . .	36
3.3.1	Kinetic friction . . . . .	36
3.3.2	Static friction . . . . .	37

3.4	Out-of-plane buckling . . . . .	38
3.5	Investigating default parameters . . . . .	40
3.5.1	Computational cost . . . . .	42
3.6	Load and stretch dependencies . . . . .	44
3.6.1	Pressure reference for normal load . . . . .	44
3.6.2	Strain dependency . . . . .	44
3.6.3	Load dependency . . . . .	47
3.6.4	Prospects of a negative friction coefficient . . . . .	48
<b>4</b>	<b>Summary</b>	<b>51</b>
4.1	Summary and conclusions . . . . .	51
4.1.1	Designing an MD simulation . . . . .	51
4.1.2	Generetig Kirigami patterns . . . . .	52
4.1.3	Control friction using Kirigami . . . . .	52
4.1.4	Capturing trends in friction data with machine learning . . . . .	53
4.1.5	Accelerated search . . . . .	54
4.1.6	Negative friction coefficient . . . . .	54
4.2	Outlook . . . . .	55
<b>Appendices</b>		<b>57</b>
<b>A</b>	<b>Appendix A</b>	<b>59</b>
<b>A</b>	<b>Appendix B</b>	<b>61</b>
<b>B</b>	<b>Appendix C</b>	<b>63</b>

# Chapter 1

## Introduction

### 1.1 Motivation

Friction is the force that prevents the relative motion of objects in contact. From our everyday life, we recognize it as the inherent resistance to sliding motion. Some surfaces appear slippery and some rough, and we know intuitively that sliding down a snow-covered hill is much more exciting than its grassy counterpart. Without friction, it would not be possible to walk across a flat surface, lean against the wall without falling over or secure an object by the use of nails or screws [p. 5] [1]. It is probably safe to say that the concept of friction is integrated into our everyday life to such an extent that most people take it for granted. However, the efforts to control friction date back to the early civilization (3500 B.C.) with the use of the wheel and lubricants to reduce friction in translational motion [2]. Today, friction is considered a part of the wider field *tribology* derived from the Greek word *tribos* meaning “rubbing” and includes the science of friction, wear and lubrication [2]. The most compelling motivation to study tribology is ultimately to gain full control of friction and wear for various technical applications. Especially, reducing friction is of great interest as this has advantages for energy efficiency. It has been reported that tribological problems have a significant potential for economic and environmental improvements [3]:

“On global scale, these savings would amount to 1.4% of the GDP annually and 8.7% of the total energy consumption in the long term.” [4].

On the other hand, the reduction of friction is not the only sensible application for tribological studies. Controlling frictional properties, besides minimization, might be of interest in the development of a grasping robot where finetuned object handling is required. While achieving a certain “constant” friction response is readily obtained through appropriate material choices, we are yet to unlock the full capabilities to alter friction dynamically on the go. One example from nature inspiring us to think along these lines are the gecko feet. More precisely, the Tokay gecko has received a lot of attention in scientific studies aiming to unravel the underlying mechanism of its “toggable” adhesion properties. Although geckos can produce large adhesive forces, they retain the ability to remove their feet from an attachment surface at will [5]. This makes the gecko able to achieve a high adhesion on the feet when climbing a vertical surface while lifting them for the next step remains relatively effortless. For a grasping robot, we might consider an analog frictional concept of a surface material that can change from slippery to rough on demand depending on specific tasks; Slippery and smooth when interacting with people and rough and firmly gripping when moving heavy objects.

In recent years an increasing amount of interest has gone into the studies of the microscopic origin of friction, due to the increased possibilities in surface preparation and the development of nanoscale experimental methods. Nano-friction is also of great concern for the field of nano-machining where the frictional properties between the tool and the workpiece dictate machining characteristics [3]. With concurrent progress in computational capacity and development of Molecular Dynamics (MD), numerical investigations serve as an invaluable tool for getting insight into the nanoscale mechanics associated with friction. This simulation-based approach can be considered as a “numerical experiment” enabling us to create and probe a variety of high-complexity systems which are still out of reach for modern experimental methods.

In materials science such MD-based numerical studies have been used to explore the concept of so-called *metamaterials* where the material compositions are designed meticulously to enhance certain physical properties [6–11]. This is often achieved either by intertwining different material types or removing certain regions completely. In recent papers by Hanakata et al. [6, 7], numerical studies have showcased that the mechanical properties of a graphene sheet, yield stress and yield strain, can be altered through the introduction of so-called *Kirigami* inspired cuts into the sheet. Kirigami is a variation of origami where the paper is cut additionally to being folded. While these methods originate as an art form, aiming to produce various artistic objects, they have proven to be applicable in a wide range of fields such as optics, physics, biology, chemistry and engineering [12]. Various forms of stimuli enable direct 2D to 3D transformations through folding, bending, and twisting of microstructures. While original human designs have contributed to specific scientific applications in the past, the future of this field is highly driven by the question of how to generate new designs optimized for certain physical properties. However, the complexity of such systems and the associated design space makes for seemingly intractable<sup>1</sup> problems ruling out analytic solutions.

Earlier architecture design approaches such as bioinspiration, looking at gecko feet for instance, and Edisonian, based on trial and error, generally rely on prior knowledge and an experienced designer [9]. While the Edisonian approach is certainly more feasible through numerical studies than real-world experiments, the number of combinations in the design space rather quickly becomes too large for a systematic search, even when considering the computation time on modern-day hardware. However, this computational time constraint can be relaxed by the use of machine learning (ML) which has proven successful in the establishment of a mapping from the design space to physical properties of interest. This gives rise to two new styles of design approaches: One, by utilizing the prediction from a trained network we can skip the MD simulations altogether resulting in an *accelerated search* of designs. This can be further improved by guiding the search accordingly to the most promising candidates, for instance, as done with the *genetic algorithm* based on mutation and crossing of the best candidates so far. Another more sophisticated approach is through generative methods such as *Generative Adversarial Networks* (GAN) or diffusion models. The latter is being used in state-of-the-art AI systems such as OpenAI's DALL-E2 [13] or Midjourney [14]. By working with a so-called *encoder-decoder* network structure, one can build a model that reverses the prediction process. This is often referred to as *reverse design*, where the model predicts a design from a set of physical target properties. In the papers by Hanakata et al. [6, 7] both the *accelerated search* and the *inverse design* approach was proven successful to create novel metamaterial Kirigami designs with the graphene sheet.

Hanakata et al. attributes the variation in mechanical properties to the non-linear effects arising from the out-of-plane buckling of the sheet. Since it is generally accepted that the surface roughness is of great importance for frictional properties it can be hypothesized that Kirigami-induced out-of-plane buckling can also be exploited for the design of frictional metamaterials. For certain designs, we might hope to find a relationship between the stretching of the sheet and frictional properties. If significant, this could give rise to an adjustable friction behavior beyond the point of manufacturing. For instance, the grasping robot might apply such a material as artificial skin for which stretching or relaxing of the surface could result in a changeable friction strength.

In addition, the Kirigami graphene properties can be explored through a potential coupling between the stretch and the normal load, through a nanomachine design, with the aim of altering the friction coefficient. This invites the idea of non-linear friction coefficients which might in theory also take on negative values. The latter would constitute a rare property only found a few cases. These are mainly for the unloading phase of adhesive surfaces [15] or the loading phase of particular heterojunction materials [16, 17].

To the best of our knowledge, Kirigami has not yet been implemented to alter the frictional properties of a nanoscale system. However, in a recent paper by Liefferink et al. [18] it is reported that macroscale Kirigami can be used to dynamically control the macroscale roughness of a surface through stretching. They reported that the roughness change led to a changeable frictional coefficient by more than one order of magnitude. This supports the idea that Kirigami designs can be used to alter friction, but we believe that taking this concept to the nanoscale would involve a different set of governing mechanisms and thus contribute to new insight in this field.

---

<sup>1</sup>In computer science we define an *intractable* problem as a problem with no *efficient* algorithm to solve it nor any analytical solutions. The only way to solve such problems is the *brute-force* approach, simply trying all possible solutions, which is often beyond the capabilities of computational resources.

## 1.2 Goals

In this thesis, we investigate the prospects of altering the frictional properties of a graphene sheet through the application of Kirigami-inspired cuts and stretching of the sheet. With the use of molecular dynamics (MD) simulations, we evaluate the frictional properties of various Kirigami designs under different physical conditions. Based on the MD results, we investigate the possibility to use machine learning for the prediction of frictional properties and subsequently using the model for an accelerated search of new designs. The main goals of the thesis can be summarized as follows.

1. Design an MD simulation procedure to evaluate the frictional properties of a Kirigami graphene sheet under specified physical conditions.
2. Develop a numerical framework to generate various Kirigami designs, both by seeking inspiration from macroscale designs and by the use of a random walk based algorithm.
3. Investigate the frictional behavior under varying load and stretch for different Kirigami designs.
4. Develop and train a machine learning model to predict the MD simulation result and perform an accelerated search of new designs with the scope of optimizing certain frictional properties.

## 1.3 Contributions

By working towards the goals outlined above (Sec. 1.2), I have discovered a non-linear relationship between the kinetic friction and the strain for certain Kirigami patterns. This phenomenon was found to be associated with the out-of-plane buckling of the Kirigami sheet but with no clear relationship to the contact area or the tension in the sheet. I found that this method does not provide any mechanism for a reduction in friction, in comparison to a non-cut sheet, but the straining of certain Kirigami sheets allows for both a relative increase and decrease in friction [Henrik](#). The relationship to normal load was proven negligible in this context and I have demonstrated that a coupled system of load and strain (through sheet tension) can exhibit a negative friction coefficient in certain load ranges. Moreover, I have created a dataset of roughly 10,000 data points for assessing the employment of machine learning and accelerated search of Kirigami designs. I have found, that this approach might be useful, but that it requires an extended dataset in order to produce reliable results for search.

During our investigations, I have built three numerical tools, beyond the regular scripts associated with data analysis, which can be found on Github [\[19\]](#). The tools are summarized in the following.

- I have written a LAMMPS-based [\[20\]](#) tool for simulating and measuring the frictional properties of a graphene sheet sliding on a substrate. The code is generally made flexible concerning the choice of sheet configuration, system size, simulation parameters and MD potentials, which makes it applicable for further studies within this topic. I have also built an automated procedure to carry out multiple simulations under varying parameters by submitting jobs to a computational cluster via an ssh connection. This was done by adding minor additions to the python package developed by E. M. Nordhagen [\[21\]](#).
- I have generated a Python-based tool for generating Kirigami patterns and exporting these in a compatible format with the simulation software. The generation of molecular structures is done with the use of ASE [\[22\]](#). Our software includes two classes of patterns inspired by macroscale designs and a random walk algorithm which allow for a variety of different designs through user-defined biases and constraints. Given our system size of choice, the first two pattern generators are capable of generating on the order of  $10^8$  unique designs while the random walk generator allows for significantly more.
- I have built a machine learning tool based on Pytorch [\[23\]](#) which includes setting up the data loaders, a convolutional network architecture, a loss function, and general algorithms for training and validating the results. Additionally, I have written several scripts for performing grid searches and analyzing the model predictions in the context of the frictional properties of graphene.

All numerical implementations used for this thesis have been originally developed for the purpose with the exception of the usage of libraries as mentioned above and commonly known Python libraries such as Numpy and Matplotlib.

## 1.4 Thesis structure

The thesis is divided into two parts. In Part I we introduce the relevant theoretical background, and in Part II we present the numerical implementations and the results of this thesis.

Part I contains a description of the theoretical background related to Friction (Chapter 2), Molecular Dynamics (??) and Machine Learning (??). In Sec. 2.6 we will formulate our research questions in the light of the friction theory.

In Part II, we begin by presenting our definition and setting up of the system in ???. This includes the MD simulations and the generation of Kirigami designs. This is followed by a pilot study in Chapter 3 where we evaluate the simulation results for various physical conditions and compare a non-cut sheet to two different Kirigami designs. Further explorations of the Kirigami configurations are carried out in ??? which includes the generation of a dataset and the employment of machine learning and an accelerated search. We use the results from the pilot study to demonstrate the possibility to achieve a negative friction coefficient for a system with coupled load and strain in ???. Finally, we summarize our results and provide an outlook for further studies in Chapter 4. Additional figures are shown in ???, ?? and ??.

# Part I

# Background Theory



# Chapter 2

## Friction

Since we aim for controlling frictional properties, we will review the relevant theoretical understanding of friction in this chapter. We limit ourselves to the tribological subcategory, wear-less dry friction, meaning that we consider friction in the absence of lubricant and wear between the contacting surfaces. We will direct the review towards our system of interest which will serve as a basis for a formal definition of our research questions at the end of this chapter.

### 2.1 Friction across scales

Tribological systems span a wide range of time and length scales, from geological stratum layers involved in earthquakes [3] to atomistic processes, such as the gliding motion of nanoclusters or nanomotors [24]. This vast difference in scale leads to different dominant frictional mechanisms. At the macroscale, the experimental systems are typically subjected to relatively high loads and sliding speeds, resulting in significant contact stress and wear. This makes for a macroscale friction that is often reduced into a few variables such as load, material type, sliding speed and surface roughness. On the other hand, the micro-/nanoscale regime is usually studied in the opposite domain operating under a relatively small load and sliding speed with negligible wear [3] [2, p. 5]. This reveals a change in the dominant mechanism at play with an emphasis on the importance of surface properties. The works of Bhushan and Kulkarni [25] showed that the friction coefficient decreased with scale even though the materials used were unchanged. This reveals an intrinsic relationship between friction and scale as the contact condition is altered. The phenomenological descriptions of macroscale friction cannot yet be derived from the fundamental atomic principles, and bridging the gap between different length scales in tribological systems remains an open challenge [24]. Hence, the following sections will be organized into macroscale (Sec. 2.2), microscale (Sec. 2.3) and nanoscale (Sec. 2.4) representing the theoretical understanding governing each scale regime. Realizing that the field of friction across all scales is a vastly broad topic, we will only introduce the most essential findings for each scale while keeping a main focus on features associated with our system on at the nanoscale.

### 2.2 Macroscale

Our working definition of the *macroscale* is everything on the scale of millimeters and above [26]. This represents the scale of visible objects and includes objects from everyday interactions to big geological systems.

#### 2.2.1 Amontons' law

In order to start and keep a solid block moving against a solid surface we must overcome certain frictional forces  $F_{\text{fric}}$  [1]. The static friction force  $F_s$  corresponds to the minimum tangential force required to initiate the sliding while the kinetic friction force  $F_k$  corresponds to the tangential force needed to sustain such a sliding at a steady speed. The work of Leonardo da Vinci (1452–1519), Guillaume Amontons (1663–705) and Charles de Coulomb (1736–1806) all contributed to the empirical law, commonly known as *Amontons' law*, which serves as a common base for macroscale friction. Amontons' law states that the frictional forces are entirely independent of contact area and sliding velocity. Instead, it relies only on the normal force  $F_N$ , acting perpendicular to the surface, and

the material-specific friction coefficient  $\mu$  as

$$F_{\text{fric}} = \mu F_N. \quad (2.1)$$

Notice that the term *normal force* is often used interchangeably with *load* and *normal load* although the load and normal load refer to the applied force that pushes the object into the surface, whereas the normal force is the reaction force acting from the surface on the object. In equilibrium, these forces are equal in magnitude and opposite in direction, and for the scope of our thesis, we will not make a distinction between these terms as well. On the same note, we point out that the frictional force is different from a conventional force which in the Newtonian definition acts on a body from the outside and makes it accelerate [27]. Rather than being an independent external force the friction force is an internal *reaction* force opposing the externally applied “sliding” force.

The friction coefficient  $\mu$  is typically different for the cases of static ( $\mu_s$ ) and kinetic ( $\mu_k$ ) friction, usually both with values lower than one and  $\mu_s \geq \mu_k$  in all cases [1, p. 6]. The friction coefficient is taken to be a constant defined by either [27]

$$\mu_1 = \frac{F_{\text{fric}}}{F_N}, \quad (2.2a) \quad \text{or} \quad \mu_2 = \frac{dF_{\text{fric}}}{dF_N}. \quad (2.2b)$$

The first definition Eq. (2.2a) requires zero friction at zero load, i.e.  $F_{\text{fric}} = 0$  at  $F_N = 0$ , while the second definition Eq. (2.2b) allows for a finite friction force at zero load as the coefficient is defined by the slope of the friction-load curve. The consequences of these definitions are illustrated in Fig. 2.1, for selected friction-load-curves in Fig. 2.1a and corresponding friction coefficients in Fig. 2.1b and Fig. 2.1c. For adhesive contacts, the friction force will not be zero under zero load [27] (red curve: Linear + shift) which can be mitigated by adding an extra constant to Eq. (2.1). Using Eq. (2.2a) for adhesive contacts would make the friction coefficient diverge for decreasing load as illustrated in Fig. 2.1b. Thus, we find the second definition Eq. (2.2b) more robust and versatile. This also allows for a better interpretation of the friction coefficient in the case where friction depends non-linearly on load as seen with the purple curve in Fig. 2.1.

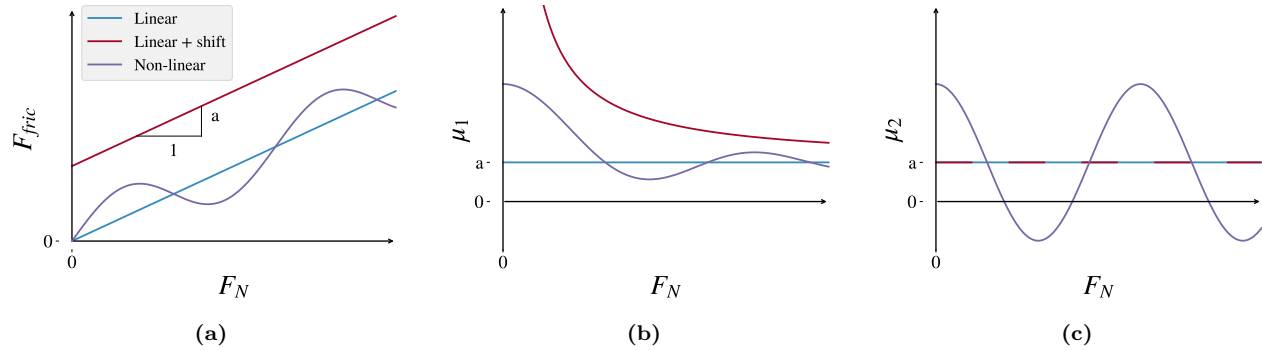


**Figure 2.1:** Illustration of the consequences for the two definitions of the friction coefficient in Eq. (2.2). (a) Three examples of friction-load curves consisting of a typical linear curve (blue), a linear curve with a shift representing an adhesive contact (red), and a non-linear curve (purple). The corresponding friction coefficients  $\mu_1$  and  $\mu_2$  are shown for the first definition Eq. (2.2a) in (b) and the second definition Eq. (2.2b) in (c).

Amontons' law represents the behavior relatively accurately for many surfaces in contact, involving both dry and lubricated, ductile and brittle and rough and smooth surfaces (as long as they are not adhesive) under a variety of conditions [27]. But it has its limitations. For instance, at low velocities, Amontons' model breaks down due to thermal effects, and for high velocities due to inertial effects [1, pp. 5–6]. Additionally, static friction depends on the so-called contact history, with increasing static friction as the logarithm of time in stationary contact [28].

In cases where Amontons' law breaks down, we might still use the conceptual definition of the friction coefficient as defined by Eq. (2.2b). Especially, in the context of achieving negative friction coefficients (for certain load ranges), we would refer to this definition, since Eq. (2.2a) would imply a truly unphysical situation

of the frictional force acting in the same direction as the sliding motion. This would accelerate the object indefinitely<sup>2</sup>.

Due to the empirical foundation of Amontons' law, it does not provide any physical insight into the underlying mechanisms of friction. However, as we will later discuss in more detail, we can understand the overall phenomena of friction through statistical mechanics by the concept of *equipartition of energy* [24]. A system in equilibrium has its kinetic energy uniformly distributed among all its degrees of freedom. When a macroscale object is sliding in a given direction it is clearly not in equilibrium since one of its degrees of freedom carries considerably more kinetic energy. Thus, the system will tend to transfer kinetic energy to the remaining degrees of freedom in the form of heat dissipating to the surroundings. This will make the object slow down if not continuously driven forward by an external energy source. Hence, we can understand the overall concept of friction simply as the tendency of going toward equilibrium energy equipartitioning among many interacting degrees of freedom [24]. From this point of view, it is clear that friction is an inevitable part of contact physics, but even though friction cannot be removed altogether, we are still capable of manipulating it in useful ways.

The attentive reader might point out that we have already moved the discussion into the microscopic regime as *statistical mechanics* generally aim to explain macroscale behavior by microscopic interactions. This highlights the necessity to consider smaller scales in order to achieve a more fundamental understanding of friction.

We note that more advanced models for macroscale friction exist. For instance, the earthquake-like (EQ) model, also known as the *spring-and-block* model or the *multi-contact* model [24], developed by Burridge and Knopoff [29]. This has been used in many studies of earthquake friction [30] and similar schemes have since been used to model the failure of fiber bundles and faults [31, 32]. Also, *rate and state* models have been used for such macroscale modeling [33]. However, these extensions are beyond the scope of this thesis as we will mainly focus on the nanoscale description.

## 2.3 Microscopic scale

Going from a macro- to a microscale perspective, at a length scale on the order  $10^{-6}$  m, it was realised that most surfaces are in fact rough [34]. The contact between two surfaces consists of numerous smaller contact points, so-called *asperities*, which form junctions due to contact pressure and adhesion as visualized in Fig. 2.2 [3]. In the macroscale perspective of Amonton's law, we refer to time- and space-averaged values, i.e. the apparent contact area and the average sliding speed [27]. However, microscopically we find the real contact area to be much smaller than the apparent area [3], and the shearing motion of local microjunctions to happen at large fluctuations rather than as one synchronized movement throughout the surface.

It is generally accepted that friction is caused by two mechanisms: Mechanical friction and chemical friction [3]. Mechanical friction is the “plowing” of the surface by hard particles or said asperities with an energy loss attributed to deformations of the asperity. While plastic deformations, corresponding to wear, gives rise to an obvious attribution for the energy loss, elastic deformations are also sufficient in explaining energy loss due to phonon excitations. The assumption of plastic deformations has been criticized as this is theorized only to be present at the beginning of a surface contact while it is negligible for prolonged or repeated contacts [35]. That is, when machine parts slide against each other for millions of cycles, the plastic deformation would only take place at the beginning for which the system then reaches a steady state with only elastic deformations. The chemical friction arises from adhesion between microscopic contacting surfaces, with an energy loss attributed to the breaking and forming of chemical bonds between the interacting surfaces.

### 2.3.1 Asperity theories

Asperity theories have their foundations in the adhesion model proposed by Bowden and Tabor [36] which is based on the fundamental reasoning that friction is governed by the adhesion between two surfaces [37]. Adhesion is proportional to the real contact area defined by asperity junctions, and interfacial shear strength  $\tau$  between such contacting junctions. For an asperity contact area  $A_{\text{asp}}$  we get a true contact area  $\sum A_{\text{asp}}$  leading to

$$F_{\text{fric}} = \tau \sum A_{\text{asp}}.$$

---

<sup>2</sup>You would most likely have a good shot at the Nobel Prize with that paper.

Note that this is still compatible with Amontons' law in Eq. (2.1) by having a linear relationship between the real contact area and the applied load. In fact, this is exactly how the theoretical model explains the friction dependency of load. By increasing the normal load it is hypothesized that the real contact area will increase as the asperity tips are deformed (plastically or elastically) into broader contact points as visualized qualitatively in Fig. 2.2.

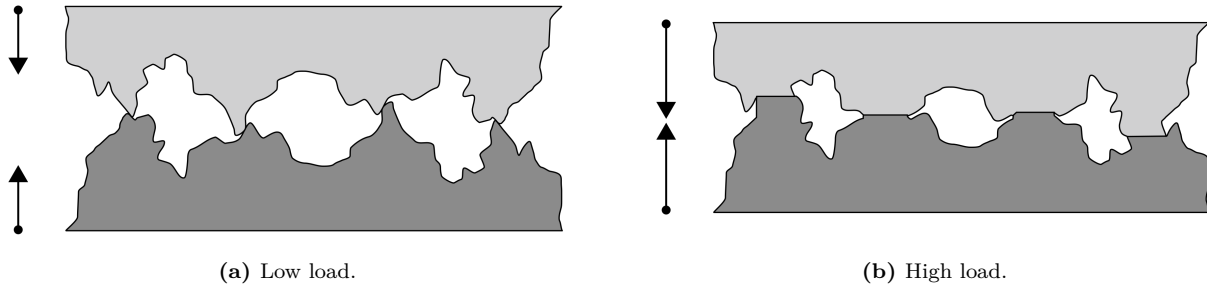


**Figure 2.2:** Qualitative illustration of the microscopic asperity deformation under increasing load from frame (a) to (b) [38]. While this figure seemingly portrays plastic deformation the concept of increased contact area with increased load applies to elastic deformation as well.

Many studies have focused on single asperity contacts to reveal the relationship between the contact area and load [39–41]. By assuming perfectly smooth asperities, with radii of curvature from micrometers all the way down to nanometers, continuum mechanics can be used to predict the deformation of asperities as load is applied. A model for non-adhesive contact between homogenous, isotropic, linear elastic spheres was first developed by Hertz [42], which predicted  $A_{\text{asp}} \propto F_N^{2/3}$ . Later adhesion effects were included in a number of subsequent models, including Maugis-Dugdale theory [43], which also predicts a sublinear relationship between  $A_{\text{asp}}$  and  $F_N$ . Thus, the common feature of all single-asperity theories is that  $A_{\text{asp}}$  is a sublinear function of  $F_N$ , leading to a similar sublinear relationship for  $F_{\text{fric}}(F_N)$ . This fails to align with the macroscale observations modeled by Amontons' law (eq. (2.1)).

Concurrently with single-asperity studies, roughness contact theories are being developed [44–47] to bridge the gap between single asperities and macroscopic contacts [34]. A variety of multi-asperity theories has attempted to combine single asperity mechanics by statistical modeling of the asperity height and spatial distributions [35]. This has led to partial success in the establishment of a linear relationship between  $A_{\text{asp}}$  and  $F_N$ . Unfortunately, these results are restricted in terms of the magnitude of the load and contact area, where multi-asperity contact models based on the original ideas of Greenwood and Williamson [46] only predicts linearity at vanishing low loads, or Persson [45] which predicts linearity for more reasonable loads up to 10–15% of the macroscale contact area. However, as the load is further increased all multi-asperity models predict the contact area to fall into the sublinear dependency of normal force as seen for single asperity theories as well [35].

## 2.4 Nanoscale — Atomic scale

Going from a micro- to a nanoscale, on the order of  $10^{-9}$  m, it has been predicted that continuum mechanics will start to break down [48] due to the discreteness of individual atoms. In a numerical MD study by Mo et al. [34], considering asperity radii of 5–30 nm, it has been shown that the asperity area  $A_{\text{asp}}$ , defined by the circumference of the contact zone, is sublinear with  $F_N$ . This is accommodated by the observation that not all atoms within the circumference make chemical contact with the substrate. By modeling the real contact area  $A_{\text{real}} = N A_{\text{atom}}$ , where  $N$  is the number of atoms within the range of chemical interaction and  $A_{\text{atom}}$  the associated surface area for a contacting atom, they found a consistent linear relationship between friction and the real contact area. Without adhesive forces, this leads to a similar linear relationship  $F_{\text{fric}} \propto F_N$ , while adding van der Waals adhesion to the simulation gave a sublinear relationship matching microscale single asperity theory, even though the  $F_{\text{fric}} \propto A_{\text{real}}$  was maintained. This result emphasizes that the predictions of continuum mechanisms might still apply at the nanoscale and that the contact area can be expected to play an important role for nanoscale asperity contacts. It is simply the definition of the contact area that changes when transitioning from micro- to nanoscale.

While the study by Mo et al. [34] considers a single asperity on a nanoscale, some models take this even further to what we will denote as the atomic scale. This final leap is motivated by the fact that our system of interest, an atomically flat graphene sheet imposed on a flat silicon substrate, lacks the presence of nanoscale asperities in its initial uncut undeformed state. In the lack of noteworthy structural asperities, friction can instead be modeled as a consequence of the “rough” potential laid out by the atomic landscape. A series of so-called *reduced-order* models build on a simplified system of atomic-scale contacts based on three essential parts: 1) A periodic potential modeling the substrate as a rigid crystalline surface. 2) An interacting particle, or collection of particles, placed in the potential. 3) A moving body, moving at a steady speed, connected to the particles through a harmonic spring. In figure Fig. 2.3 three of the most common 1D models are displayed which we will address in the following sections. The time-honored Prandtl-Tomlinson (PT) model describes a point-like tip sliding over a space-periodic fixed crystalline surface with a harmonic coupling to the moving body. This is analog to that of an experimental cantilever used for Atomic Force Microscopy which we will introduce in more detail in Sec. 2.4.5.1. Further extensions were added in the Frenkel-Kontorova (FK) model by substituting the tip with a chain of harmonically coupled particles dragged from the end, and finally combined in the Frenkel-Kontorova-Tomlinson (FKT) with the addition of a more rigorous harmonic coupling between the moving body and each of the atoms in the chain. While these models cannot provide the same level of detail as atomistic simulations, such as MD, they enable investigation of atomic friction under most conditions, some of which are inaccessible to MD [49]. This makes these models an appropriate tool for investigating individual parameters and mechanisms governing friction.

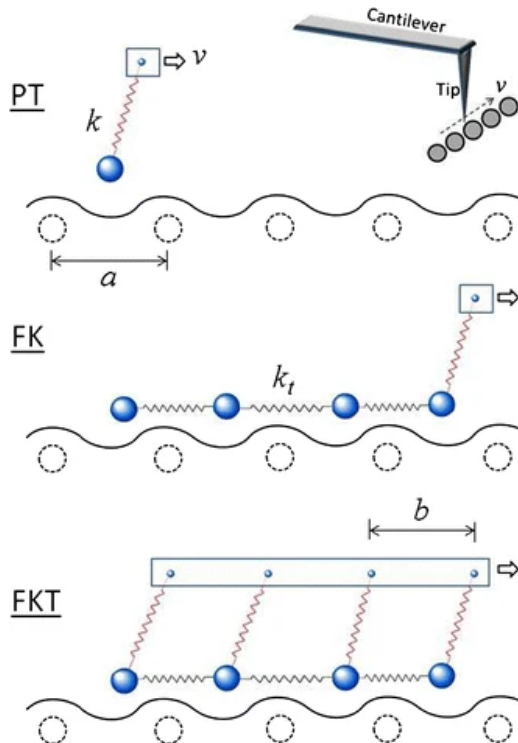


**Figure 2.3:** Illustration of the key features of the Prandtl-Tomlinson (PT), Frenkel-Kontorova (FK) and Frenkel-Kontorova-Tomlinson (FKT) respectively [49]. Rights and permissions Be careful to align the notation on the figures with the text later on. consider to cut up and put side by side.

#### 2.4.1 Prandtl–Tomlinson

The Prandtl–Tomlinson model (PT) considers a 1D simplification of the frictional system as a single ball-tip sliding along the rigid substrate as shown in Fig. 2.3. The tip is coupled harmonically to a moving support, moving at a constant speed, which drives the tip forward. The interaction between the tip and the substrate is modeled by a sinusoidal corrugation potential mimicking the periodicity found in a crystalline substrate. We will consider the Prandtl–Tomlinson model with added thermal activation as proposed by Gnecco et al. [50]. For the

theoretical foundation of this section, we generally refer to [49]. The potential energy for the tip at position  $x$  for time  $t$  is given as

$$V(x, t) = \frac{1}{2}K(vt - x)^2 - \frac{1}{2}U_0 \cos\left(\frac{2\pi x}{a}\right). \quad (2.3)$$

The first term describes the harmonic coupling with spring constant  $K$ , between the tip at position  $x$  and the moving body at position  $vt$ , given by its constant speed  $v$ . The second term describes the corrugation potential with amplitude  $U_0$  and period  $a$  representing the lattice spacing of the substrate. The dynamics of the tip can be described by the Langevin equations

$$m\ddot{x} + m\mu\dot{x} = -\frac{\partial V(x, t)}{\partial x} + R(t), \quad (2.4)$$

where  $m$  is the mass of the tip,  $\mu$  the viscous friction and  $R(t)$  the thermal activation term. The equation is solved for tip position  $x$  and the friction force is retrieved as the force acting on the moving body

$$F_{\text{fric}} = K(vt - x).$$

The governing equation Eq. (2.4) belongs to a family of stochastic differential equations composed of both deterministic dynamics and stochastic processes. In this case, the deterministic term is the viscous friction,  $m\mu\dot{x}$ , to resist the movement of the tip and the force acting from the corrugation potential. The stochastic term is a random force field modeling thermal noise according to the Fluctuation-dissipation relation. Thus, there is no single path but rather multiple paths the tip can take. While the Langevin equation is one of the most common ways to handle thermal activation other methods exist to solve this problem such as Monte Carlo sampling methods. We omit the numerical scheme for the solving of the Langevin equations here and refer instead to a more in-depth discussion of the Langevin equation regarding the MD simulations in ??.

#### 2.4.1.1 Thermal activation

The solving of the Langevin equation, as opposed to Newton's equation of motion, introduces thermal effects to the system. Generally, when the energy barrier comes close to  $k_B T$  (0.026 eV at room temperature) thermal effects can not be neglected. In the case of a single asperity contact the energy barrier is on the order 1 eV which makes thermal activation significant [49]. Due to the moving body traveling at a constant speed, the potential energy will increase steadily. Without any temperature,  $T = 0$ , the slip will only occur when the energy barrier between the current potential well ( $i$ ) and the adjacent ( $j$ ) is zero  $\Delta V_{i \rightarrow j} = 0$ . However, in the presence of temperature, we get thermal activation, meaning that the tip can slip to the next potential well sooner at  $\Delta V_{i \rightarrow j} > 0$ . Provided that the sliding speed is slow enough the transition rate  $\kappa$  for a slip from the current to the next well is given by

$$\kappa = f_0 e^{-\Delta V/k_B T}, \quad (2.5)$$

with  $\Delta V$  being the energy barrier and  $f_0$  the attempt rate. The attempt rate following Kramer's rate theory [51] and is related to the mass and damping of the system and can be thought of as the frequency at which the tip "attempts" to overcome the barrier. Notice that Eq. (2.5) resembles a microstate probability in the canonical ensemble with  $f_0$  in place of the inverse partition function  $Z^{-1}$  which provides an additional interpretation of  $f_0$ . The probability  $p_i$  that the tip occupies the current well ( $i$ ) relative to the adjacent well ( $j$ ), as illustrated in Fig. 2.4 is governed by

$$\frac{dp_i}{dt} = -\kappa_{i \rightarrow j} p_i + \kappa_{j \rightarrow i} p_j. \quad (2.6)$$

This probability is related to temperature, speed and mass [49].

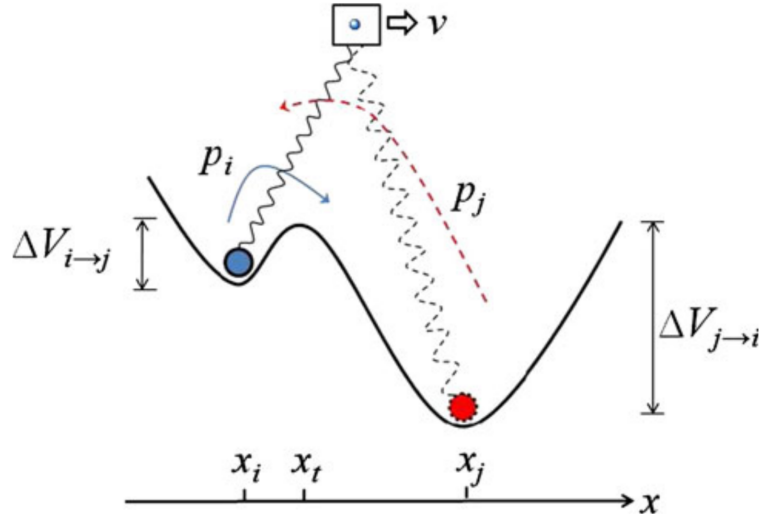


**Figure 2.4:** An illustration of slip between two adjacent energy minima.  $p_i$  is the probability of the tip residing in the current potential well,  $i$ , where the energy barrier is  $\Delta V_{i \rightarrow j}$ .  $p_j$  is the probability of the tip residing at the next minima,  $j$ , where  $\Delta V_{j \rightarrow i}$  is the corresponding energy barrier. Figure and caption from [49]. Rights and permission

Generally, there exist two temperature regimes in the Prandtl–Tomlinson model: The *thermal activation* regime at low temperatures and the *thermal drift* at high temperatures as shown in Fig. 2.5. At lower temperatures, the system is subject to standard thermal activation with a much lower energy barrier for slipping forward than backward  $\Delta V_{j \rightarrow i} \gg \Delta V_{i \rightarrow j}$ . This results in a higher transition rate for forward slips,  $\kappa_{j \rightarrow i} \ll \kappa_{i \rightarrow j}$ , which effectively inhibits any backward slip. This leads to the simplified expression for Eq. (2.6)

$$\frac{dp_i}{dt} = -\kappa_{i \rightarrow j} p_i,$$

which makes the relationship between friction, temperature and speed follow Sang et al.'s prediction [52]

$$F = F_c - \left| \beta k_B T \ln \left( \frac{v_c}{v} \right) \right|^{2/3}, \quad v_c = \frac{2f_0 \beta k_B T}{3C_{\text{eff}} \sqrt{F_c}}, \quad (2.7)$$

where  $F_c$  is the maximum friction at  $T = 0$ ,  $v_c$  a critical velocity,  $f_0$  is the attempt rate,  $c_{\text{eff}}$  the effective stiffness, and  $\beta$  a parameter determined by the shape of the corrugation well. Eq. (2.7) characterizes the decrease in friction with temperature in the thermal activation regime, shown in Fig. 2.5a at low temperature. This corresponds with the assumption of only forward slips, as seen in the force trace in Fig. 2.5a. When the temperature is high enough for the system to be consistently close to thermal equilibrium, it enters the regime of thermal drift [53]. This regime transition can be understood through a comparison between two time scales: The time it takes for the moving body to travel one lattice spacing  $t_v = a/v$  and the average time for a slip to occur due to thermal activation  $\tau = 1/\kappa = f^{-1} \exp(\Delta V/k_B T)$ . If  $t_v \gg \tau$  the system falls within the thermal drift regime, where slips happens both in the forward and backward direction as shown in the force trace in Fig. 2.5b. For the thermal drift regime, the friction follows the prediction by Krylov et al. [53–55]

$$F \propto \frac{v}{T} e^{1/T}. \quad (2.8)$$

Notice that the friction dependence on sliding speed changes from Eq. (2.7) to Eq. (2.8) as it transitions from the thermal activation to the thermal drift regime.

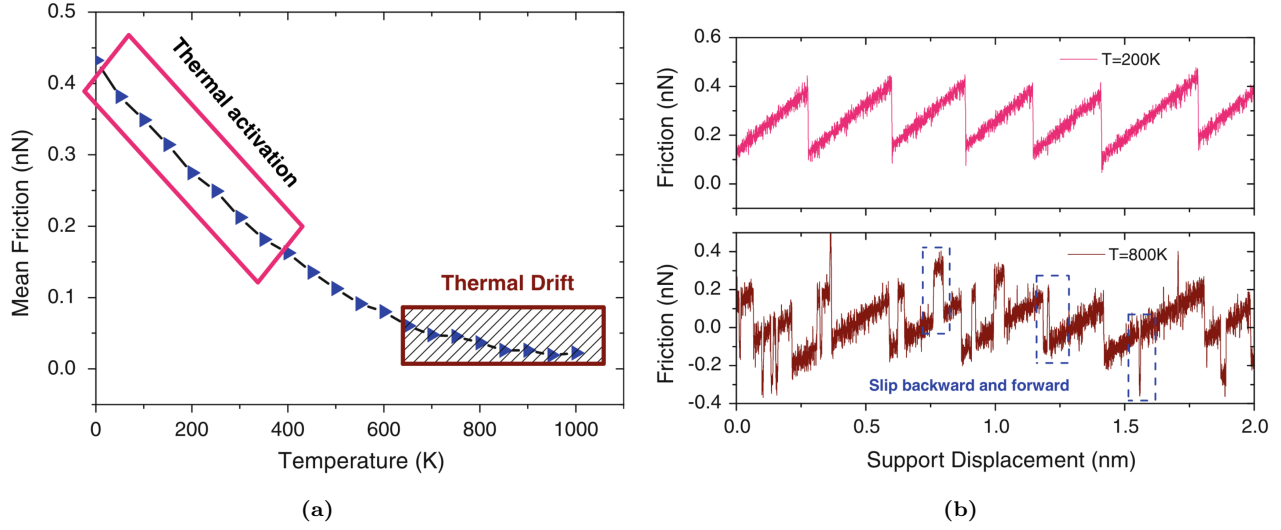


**Figure 2.5:** Illustration of the temperature difference between the thermal activation regime and the thermal drift regime. (a) shows the mean friction as a function of temperature showcasing the regime transition. The figure corresponds to the numerical results of Dong et al. [49] of a Prandtl–Tomlinson model with model parameters:  $m = 10^{-12}$  kg,  $U_0 = 0.6\text{eV}$ ,  $v = 4 \times 10^3$  nm/s,  $\mu = 2\sqrt{k/m}$ ,  $a = 0.288$  nm. (b) shows the force traces of a simulation in the thermal activation regime (top) and thermal drift regime (bottom) with several characteristic forward and backward slips identified by dashed lines for the latter case. Figures from [49] Rights and permission.

#### 2.4.1.2 Sliding speed

In the thermal activation regime (low temperature) and at low sliding speeds, the friction relation follows Eq. (2.7) which means that friction increases logarithmically with speed. For higher speeds, above the critical velocity  $v > v_c$ , if only thermal effects are considered, Eq. (2.7) predicts that friction will eventually saturate and come to a plateau at  $F_{\text{fric}} = F_C$ . This is illustrated in Fig. 2.6 with this prediction being represented by the dotted line. However, as given away by the figure, for higher speeds the model will enter an *athermal* regime where the thermal effects are negligible compared to other contributions [56]. In the athermal regime, the damping term  $\mu\dot{x}$  will dominate yielding  $F_{\text{fric}} \propto v$ . The athermal regime is often observed in reduced-models if the system is overdamped or at high speeds. This concept is related to MD simulations as well where the accessible speeds often fall into the athermal regime [57]. It is unclear how this affects real physical systems for which there exist more dissipation channels than just a single viscous term [58]. For the thermal drift regime, at higher temperatures, friction increase linearly with sliding speed  $F_{\text{fric}} \propto v$  as given by Eq. (2.8).

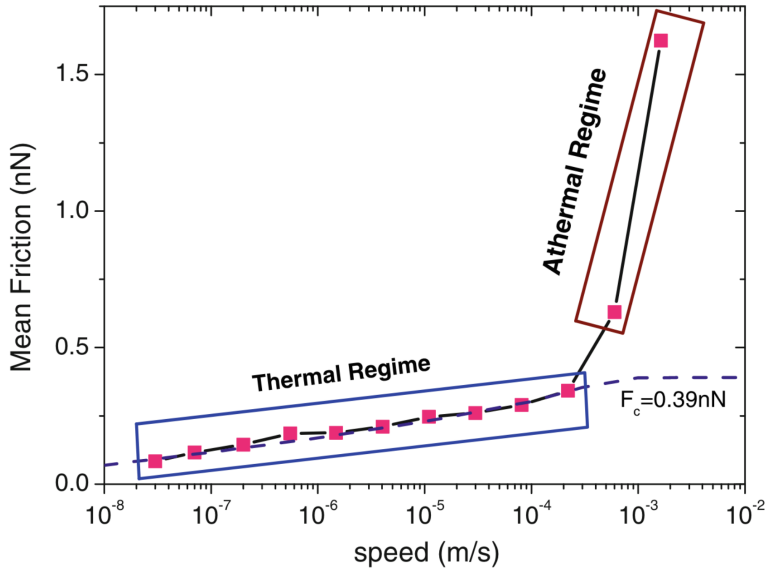


**Figure 2.6:** The friction dependence on sliding speed for the simulated Prandtl–Tomlinson by Dong et al. [49] revealing two different regimes. In the thermal regime, friction increases logarithmically with speed, and in the athermal regime, friction is governed by damping such that  $F \propto v$ . The friction plateau ( $F_c = 0.39$  nN) predicted by thermal activation is shown as a dotted line. Other model parameters:  $m = 10^{-12}$  kg,  $U_0 = 0.6$  eV,  $T = 300$  K,  $\mu = 2\sqrt{k/m}$ ,  $a = 0.288$  nm. Figure from [49] [Rights and permission](#)

#### 2.4.1.3 Tip mass

The mass of the tip affects the dynamics due to a change of inertia, which changes the attempt rate  $f_0$ . Smaller inertia leads to a larger attempt rate and vice versa. Effectively, this will affect the transition point for the temperature and speed regimes described previously. A smaller inertia, giving a larger attempt rate, will cause an earlier transition (i.e. at a lower temperature) to the thermal drift regime. Additionally, this will result in a later speed saturation such that it transitions to the athermal regime at a higher speed.

#### 2.4.1.4 Friction Regimes: Smooth Sliding, Single Slip, and Multiple Slip

Stick-slip motion is a crucial instability mechanism associated with high energy dissipation and high friction. Thus, controlling the transition between smooth sliding and stick-slip is considered key to controlling friction. We can divide the frictional stick-slip behavior into three regimes: 1) Smooth sliding, where the tip slides smoothly on the substrate. 2) Single slip, where the tip sticks at one potential well before jumping one lattice spacing to the next. 3) Multiple slip, where the tip jumps more than one lattice spacing for a slip event. The underlying mechanisms behind these regimes can be understood through static and dynamic contributions.

To understand the static mechanism we consider a quasistatic process for which temperature, speed and damping can be neglected. For a quasistatic process, we require  $\partial(V)/\partial x = 0$ . This simplifies Eq. (2.3) to

$$\frac{\pi U_0}{a} \sin\left(\frac{2\pi x}{a}\right) \frac{2\pi}{a} = K(vt - x). \quad (2.9)$$

The friction regime is determined by the number of solutions  $x$  to Eq. (2.9). Only one solution corresponds to smooth sliding, two solutions to a single slip and so on. It turns out that the regimes can be defined by the parameter  $\eta = 2\pi^2 U_0 / a^2 K$  [59, 60] yielding transitions at  $\eta = 1, 4.6, 7.79, 10.95, \dots$ , such that  $\eta \leq 1$  corresponds to smooth sliding,  $1 < \eta \leq 4.6$  to a single slip and so on. These static derivations lay out the fundamental probabilities for being in one of the stick-slip regimes. Notice that increasing the spring constant  $K$  (stiff spring) will decrease the possibilities for stick-slip behavior. Similarly, the potential corrugation  $U_0$  can be altered by an increasing load [61].

Considering the dynamics on top, one finds that damping, speed and temperature will affect this probability. High damping, equivalent to a high transfer of kinetic energy to heat, will result in less energy available for the

slip events. This will make multiple slip less likely. By a similar argument, we find that increasing the speed will contribute to more kinetic energy which will increase the likelihood of multiple slip. Finally, the temperature will contribute to earlier slips, due to thermal activation, such that less potential energy can be accumulated and it will result in fewer multiple slip.

### 2.4.2 Frenkel-Kontorova

The Frenkel-Kontorova (FK) model [62] extends the Prandtl–Tomlinson model by considering a chain of atoms in contrast to just a single particle (tip). This extension is useful for understanding the importance of the alignment between the atoms and the substrate, the so-called *commensurability*. Our review of the Frenkel-Kontorova is based on [24, 61].

The standard Frenkel-Kontorova model consists of a 1D chain of  $N$  classical particles of equal mass, representing atoms, interacting via harmonic forces and moving in a sinusoidal potential as sketched in Fig. 2.7 [24]. The Hamiltonian is

$$H = \sum_{i=1}^N \left[ \frac{p_i^2}{2m} + \frac{1}{2}K(x_{i+1} - x_i - a_c)^2 + \frac{1}{2}U_0 \cos\left(\frac{2\pi x_i}{a_b}\right) \right], \quad (2.10)$$

where the atoms are labelled sequentially  $i = 1, \dots, N$ . The first term  $p_i^2/2m$  represents the kinetic energy with momentum  $p_i$  and mass  $m$ . Often the effects of inertia are neglected, referred to as the static Frenkel-Kontorova model, while the inclusion in Eq. (2.10) is known as the dynamic Frenkel-Kontorova model [63]. The next term describes the harmonic interaction with elastic constant  $K$ , nearest neighbor distance  $\Delta x = x_{i+1} - x_i$  and corresponding nearest neighbor equilibrium distance  $a_c$ . The final term represents the periodic corrugation potential, with amplitude  $U_0$  and period  $a_b$ . By comparison to the potential used in the Prandtl–Tomlinson model Eq. (2.3), the difference is the introduction of a harmonic coupling between particles in the chain as opposed to the moving body. Different boundary choices can be made where both free ends and periodic conditions give similar results. The choice of fixed ends however makes the chain incapable of sliding.

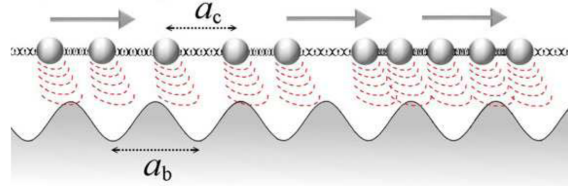


**Figure 1.** A sketch of the FK model, showing the two competing lengths: the average interparticle spacing and the lattice periodicity of the substrate.

**Figure 2.7:** Waiting for reuse permission figure from [24]

To probe static friction one can apply an external adiabatically increasing force until sliding occurs, i.e. without loss or gain of heat. This corresponds to the static Frenkel-Kontorova model, and it turns out that the sliding properties are entirely governed by its topological excitations referred to as so-called *kinks* and *antikinks*.

#### 2.4.2.1 Commensurability

We can subdivide the frictional behavior in terms of commensurability, that is, how well the spacing of the atoms matches the periodic substrate potential. We describe this by the length ratio  $\theta = a_b/a_c = N/M$  where  $M$  denotes the number of minima in the potential within the length of the chain. A rational number for  $\theta$  means that we can achieve a perfect alignment between the atoms in the chain and the potential minima, without stretching the chain, corresponding to a *commensurate* case. If  $\theta$  is irrational the chain and substrate cannot fully align without some stretching of the chain, and we denote this as being *incommensurate*.

We begin with the simplest commensurate case of  $\theta = 1$  where the spacing of the atoms matches perfectly with the substrate potential periodicity, i.e.  $a_c = a_b$ ,  $N = M$ . The ground state (GS) is the configuration

where each atom is aligned with one of the substrate minima. By adding an extra atom to the chain we would effectively shift some of the atoms, out of this ideal state, giving rise to a kink excitation. This leads to the case where two atoms will have to “share” the same potential corrugation as sketched in Fig. 2.9. On the other hand, removing an atom from the chain results in an antikink excitation where one potential corrugation will be left “atomless”. In order to reach a local minimum the kink (antikink) will expand in space over a finite length such that the chain undertakes a local compression (expansion). Notice that for low ratios of  $\theta$ , fewer atoms than minima, the chain will not be able to fill each corrugation well in any case. In this case, commensurability can instead be thought of as whether the atoms are forced to deviate, by a lattice spacing, from the spacing otherwise dictated by the spring forces in-between. When applying a tangential force to the chain it is much easier for an excitation to move along the chain than it is for the non-excited atoms since the activation energy for a kink/antikink displacement is systematically smaller (often much smaller) than the potential barrier  $U_0$ . Thus, the motion of kinks (antikinks), i.e. the displacement of extra atoms (atom vacancies), is representing the fundamental mechanism for mass transport. These displacements are responsible for the mobility, diffusivity and conductivity within this model.

In the zero temperature commensurable case with an adiabatical increase in force, all atoms would be put into an accelerating motion as soon as the potential barrier energy is present. However, similar to our discussion on the Prandtl-Tomlinson model, thermal activations will excite the system at an earlier stage resulting in kink-antikink pairs traveling down the chain. For a chain of finite length, these often occur at the end of the chain running in opposite directions. This cascade of kink-antikink excitations is shown in Fig. 2.8. Notice, that for the 2D case, where an island (flake) is deposited on a surface, we generally also expect the sliding to be initiated by kink-antikink pairs at the boundaries.

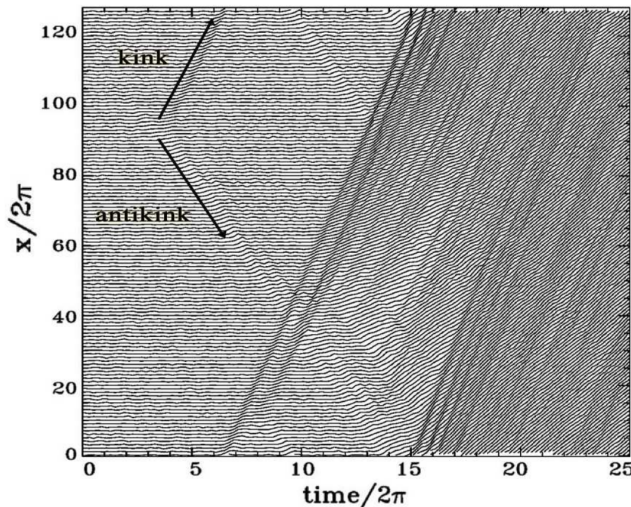


**Figure 2.** Time dependence of the atomic trajectories for the fully matched ( $\theta = 1$ ) FK model at the (low-temperature) onset of depinning. Motion starts with the nucleation of a kink-antikink pair. The kink and the antikink depart in opposite directions cross the periodic boundary conditions, and collide quasielastically. A second kink-antikink pair forms in the wake of the initial kink. Further kink-antikink pairs are generated, with an avalanche-like increase of the kink-antikink concentration, eventually leading to a sliding state. Adapted from Ref. [21], Copyright (1997) by The American Physical Society.

**Figure 2.8:** Waiting for reuse permission figure from [24]



**Figure 2.9:** **Temporary** figure from url`http://www.iop.kiev.ua/obraun/myreprints/surveyfk.pdf` p. 14. Incommensurable case ( $\theta = ?$ ) where atoms sits slightly closer than otherwise dictated by the substrate potential for which this regular result in a kink here seen as the presence of two atoms closely together in one of the potential corrugations.

For the case of incommensurability, i.e.  $\theta = a_b/a_c$  being irrational, the GS is characterized by a sort of “staircase” deformation. That is, the chain will exhibit regular periods of regions with approximate commensurability separated by regularly spaced kinks or antikinks.

The incommensurable Frenkel-Kontorova model contains a critical elastic constant  $K_c$ , such that for  $K > K_c$  the static friction  $F_s$  drops to zero, making the chain able to initiate a slide at no energy cost, while the low-velocity kinetic friction is dramatically reduced. This can be explained by the fact that the displacement occurring in the incommensurable case will yield just as many atoms climbing up a corrugation as atoms climbing down. For a big (infinite) chain this will exactly balance the forces making it non-resistant to sliding. Generally, incommensurability guarantees that the total energy (at  $T = 0$ ) is independent of the relative position to the potential. However, when sliding freely, a single atom will eventually occupy a maximum of the potential, and thus when increasing the potential magnitude  $U_0$  or softening the chain stiffness, lowering  $K$ , the possibility to occupy such a maximum disappears. This marks the so-called Aubry transition, at the critical elastic constant  $K = K_c(U_0, \theta)$ , where the chain goes from a free sliding to a *pinned* state with nonzero static friction.  $K_c$  is a discontinuous function of the ratio  $\theta$ , due to the reliance on irrational numbers for incommensurability. The minimal value  $K_c \simeq 1.0291926$  in units  $[2U_0(\pi/a_b)^2]$  is achieved for the golden-mean ratio  $\theta = (1 + \sqrt{5}/2)$ . The Aubry transition can be investigated as a first-order phase transition for which power laws can be defined for the order parameter, but this is beyond the scope of this thesis.

The phenomena of non-pinned configurations are named *superlubricity* in tribological context. Despite the misleading name, this refers to the case where the static friction is zero while the kinetic friction is nonzero, but reduced. For the case of a 2D sheet, it is possible to alter the commensurability, not only by changing the lattice spacing through material choice but also by changing the orientation of the sheet relative to the substrate. Dienwiebel et al. [64] have shown that the kinetic friction, for a graphene flake sliding over a graphite surface (multiple layers of graphene), exhibits extremely low friction at certain orientations as shown in Fig. 2.10. As the orientation is changed they observed two spikes of considerable friction while the remaining valleys correspond to effectively zero friction in consideration of the measurement uncertainty. This phenomenon relates to the transition between frictional regimes, as introduced through the Prandtl–Tomlinson model, since the change in orientation affects the effective substrate potential. Merely from the static consideration, we found that lowering the potential amplitude  $U_0$  will decrease the parameter  $\eta = 2\pi^2 U_0/a^2 K$  shifting away from the regime of multiple slips towards smooth sliding associated with low friction. Such transitions will also be affected by the shape of the potential and corresponding 2D effects of the sliding path [49].

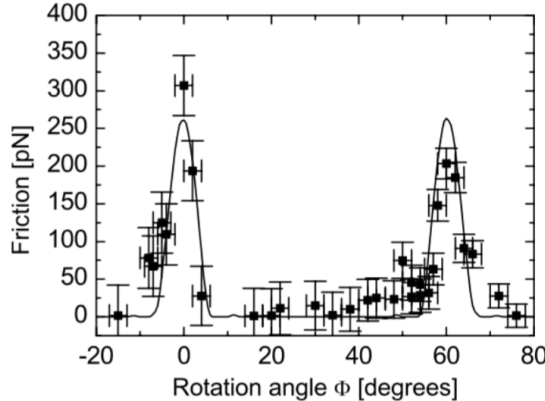


Fig. 6. Average friction force versus rotation angle  $\Phi$  of the graphite sample around an axis normal to the sample surface. Two narrow peaks of high friction are observed at  $0^\circ$  and  $61^\circ$ , respectively. Between these peaks a wide angular range with ultra-low friction, close the detection limit of the instrument, is found. The first peak has a maximum friction force of  $306 \pm 40$  pN, and the second peak has a maximum of  $203 \pm 20$  pN. The curve through the data points shows results from a Tomlinson model for a symmetric 96-atom graphite flake sliding over the graphite surface (for details about the calculation see [39]).

**Figure 2.10:** [Temporary] figure from [64] showing superlubricity for incommensurable orientations between graphene and graphite. [temporary]

#### 2.4.2.2 Velocity resonance

While many of the same arguments used for the Prandtl–Tomlinson model regarding velocity dependence for friction can be made for the Frenkel-Kontorova model, the addition of multiple atoms introduces the possibility of resonance. In the Frenkel-Kontorova model, the kinetic friction is primarily attributed to resonance between the sliding-induced vibrations and phonon modes in the chain [63]. The specific dynamics are found to be highly model and dimension specific, and even for the 1D case, this is rather complex. However, we make a simplified analysis of the 1D rigid chain in order to showcase the reasoning behind the phenomena.

When all atoms are sliding rigidly with center of mass (CM) velocity  $v_{\text{CM}}$  the atoms will pass the potential maxima with the so-called *washboard frequency*  $\Omega = 2\pi v_{\text{CM}}/a_b$ . For a weak coupling between the chain and the potential we can use the zero potential case as an approximation for which the known dispersion relation for the 1D harmonic chain is given [65, p. 92]

$$\omega_k = \sqrt{\frac{4K}{m}} \left| \sin\left(\frac{k}{2}\right) \right|,$$

where  $\omega_k$  is the phonon frequency and  $k = 2\pi i/N$  the wavenumber with  $i \in [N/2, N/2]$ . Resonance will occur when the washboard frequency  $\Omega$  is close to the frequency of the phonon modes  $\omega_q$  in the chain with wavenumber  $q = 2\pi a_c/a_b = 2\pi\theta^{-1}$  or its harmonics  $nq$  for  $n = 1, 2, 3, \dots$  [66]. Thus, we can approximate the resonance CM speed as

$$\begin{aligned} n\Omega &\sim \omega_{nq} \\ n\frac{2\pi v_{\text{CM}}}{a_b} &\sim \sqrt{\frac{4K}{m}} \left| \sin\left(\frac{2n\pi\theta^{-1}}{2}\right) \right| \\ v_{\text{CM}} &\sim \frac{\sin(n\pi\theta^{-1})}{n\pi} \sqrt{\frac{Ka_b^2}{m}}. \end{aligned}$$

When the chain slides with a velocity around resonance speed, the washboard frequency can excite acoustic phonons which will dissipate to other phonon modes as well. At zero temperature, the energy will transform

back and forth between internal degrees of freedom and CM movement of the chain. Without any dissipation mechanism, this is theorized to speed up the translational decay [63]. However, as soon as we add a dissipation channel through the substrate, energy will dissipate from the chain to the substrate's degrees of freedom. This suggests that certain sliding speeds will exhibit relatively high kinetic friction while others will be subject to relatively low kinetic friction. Simulations of concentric nanotubes in relative motion (telescopic sliding) support this idea as it has revealed the occurrence of certain velocities at which the friction is enhanced, corresponding to the washboard frequency of the system [67, 68]. The friction response was observed to be highly non-linear as the resonance velocities were approached.

The analysis of the phonon dynamics is highly simplified here, and a numerical study of the Frenkel-Kontorova by Norell et al. [63] showed that the behavior was highly dependent on model parameter choices, but that the friction generally increased with velocity and temperature. Here the latter observation differs qualitatively from that of the Prandtl-Tomlinson model.

### 2.4.3 Frenkel-Kontorova-Tomlinson

A final extension of the atomic models worth mentioning here is the Frenkel-Kontorova-Tomlinson (FKT) model [69], which introduces a harmonic coupling of the sliding atom chain to the moving body, effectively combining Prandtl-Tomlinson and Frenkel-Kontorova (see Fig. 2.3). This introduces more degrees of freedom to the model which is based on the intention of getting a more realistic connection between the moving body and the chain. Dong et al. [49] carried out a numerical analysis using the 1D Frenkel-Kontorova-Tomlinson model to investigate the effect of chain length. They observed that the friction increased linearly with the number of atoms in the chain on a long range, but certain lattice mismatches resulted in local non-linear relationships as shown in Sec. 2.4.3. Similarly, by extending the Frenkel-Kontorova-Tomlinson model to 2D they were able to achieve a similar sensitivity to commensurability as observed experimentally by [64] (see Fig. 2.10) with the numerical result shown in Sec. 2.4.3. Besides a demonstration of the commensurability effect in 2D they also observed increasing friction with an increasing flake size. Combined, the 1D and 2D results support the idea of increasing friction with contact size although it might showcase non-linear behavior depending on commensurability.

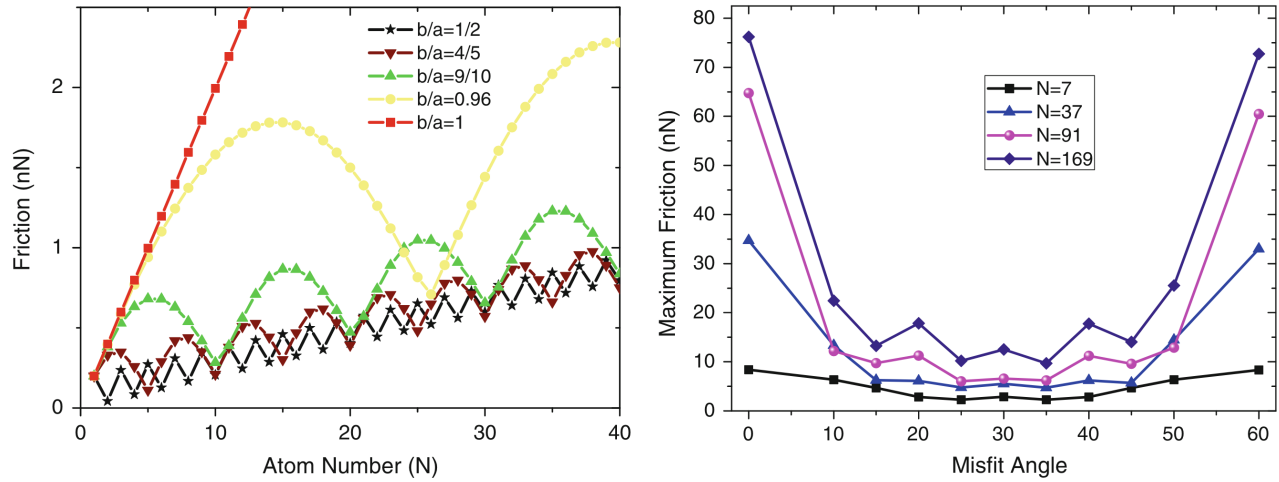


**Figure 2.11:** Friction in the Frenkel-Kontorova-Tomlinson model for varying size and Commensurability corresponding to numerical result by Dong et al. [49].  $K_t$  describes the interatomic spring constant and  $K$  the coupling to the moving body. (a) The 1D case with an increasing number of atoms in the chain and different mismatch length ratios  $\theta = a_b/a_c$ , given as  $a/b$  in their notation. The model parameters are  $K = 5 \text{ N/m}$ ,  $K_t = 50 \text{ N/m}$ . (b) The 2D case with varying angles (misfit angle) between the flake and the substrate. The model parameters are  $K = 10 \text{ N/m}$ ,  $K_t = 50 \text{ N/m}$ . Figure from [49]. Rights and permission.

### 2.4.4 Shortcomings of reduced-models

It should be noted that the reduced-models presented in this work provide a simplified description of the friction behavior. One major limitation is that all models assume a rigid substrate with a sinusoidal potential shape,

whereas in reality, the substrate reaction to sliding motion results in a constantly changing potential, making the dynamics more intricate. Moreover, the energy dissipation is simplified through a viscous term  $-m\mu\dot{x}$  in the Langevin equations Eq. (2.4), which neglects the complexity associated with electron and phonon dissipation. For example, considering phonon dissipation, there exist many vibration modes ( $3N$ ), and thus many dissipation channels for the tip. Lastly, it should be mentioned that the moving body is simplified as a constantly moving rigid body, whereas in reality, it may exhibit a more complicated dynamic behavior.

## 2.4.5 Experimental procedures

Experimentally, the study of nanoscale friction is challenging due to the low forces on the scale of nano-newtons along with the difficulties of mapping the nano-scale topography of the sample. In contrast to numerical simulations, which provide full transparency regarding atomic-scale structures, sampling of forces, velocities and temperature, the experimental results are limited by the state-of-the-art experimental methods. To facilitate the comparison of numerical and experimental results, we will address a few of the most relevant experimental methods.

### 2.4.5.1 Scanning Probe Microscopy

Scanning probe microscopy (SPM) includes a variety of experimental methods which are used to examine surfaces with atomic resolution [70, pp. 6-27]. This was originally developed for surface topography imaging, but today it plays a crucial role in nanoscale science as it is used for probe-sampling regarding tribological, electronic, magnetic, biological and chemical character. The family of methods involving the measurement of forces is generally referred to as *scanning force microscopies* (SFM) or for friction purposes *friction force microscopes* (FFM).

One such method arose from the *atomic force microscope* AFM, which consists of a sharp micro-fabricated tip attached to a cantilever force sensor, usually with a sensitivity below 1 nN all the way down to pN. The force is measured by recording the bending of the cantilever, either as a change in electrical conduction or more commonly, by a light beam reflected from the back of the cantilever into a photodetector [1, p. 183] as shown in Fig. 2.12. By adjusting the tip-sample height to keep a constant normal force while scanning across the surface, the AFM can be used to produce a surface topography map. However, when scanning perpendicularly to the cantilever axis, the frictional force can be measured as the torsion of the cantilever. By utilizing a photodetector with four quadrants (as depicted in Figure 2.12), the normal force and friction force can be simultaneously measured as the probes scan across the surface. However, when scanning perpendicularly to the cantilever axis, one is also able to measure the frictional force as torsion of the cantilever. By having four quadrants in the photodetector (see Fig. 2.12), one can simultaneously measure the normal force and friction force as the probes scan across the surface. AFM can also be utilized to drag a nanoflake across the substrate, as demonstrated by Dienwiebel et al. [64], who attached a graphene flake to a FFM tip and dragged it across graphite. However, it should be noted that this method concentrates the normal loading to a single point on the flake, rather than achieving an evenly distributed load.

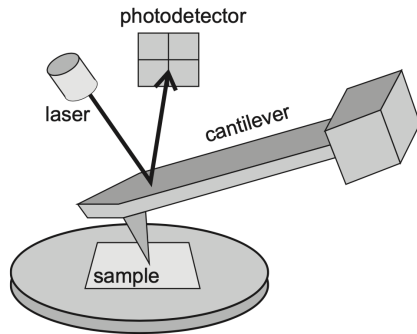


Figure 17.1 Schematic diagram of a beam-deflection atomic force microscope.

**Figure 2.12:** Schematic diagram of a beam-deflection atomic force microscope. Figure and caption from [1, p. 184]  
Rights and permission

#### 2.4.5.2 Surface Force Apparatus

Finally, it is worth mentioning the Surface Force Apparatus (SFA), which consists of two curved, molecularly smooth surfaces brought into contact [1, p. 188]. The material of choice is usually mica since it can be easily cleaved into atomically flat surfaces over macroscopic areas. The sample is then placed between the two surfaces as a lubricant film, and the friction properties can be studied by applying a tangential force to the surfaces.

## 2.5 Summary of previous results

Several studies have investigated the frictional behavior of graphene by varying different parameters such as normal force, sliding velocity, temperature, commensurability and graphene thickness [71]. In general, we find three types of relevant systems being studied: 1) An FFM type setup where the graphene, either resting on a substrate or suspended, is probed by an AFM tip scanning across the surface. 2) A SFA setup with the graphene “sandwiched” in between two substrate layers moving relative to each other using the graphene as a solid lubricant. 3) A graphene flake sliding on a substrate, either being dragged by an AFM tip or by a more complex arrangement in numerical simulations. Considering that even the sharpest AFM tip will effectively put multiple atoms in contact with the sample, all methods are relatable to the study of nanoscale surface contacts. However, the FFM type is more closely related to asperity theory since it is expected to deform under increasing load, while the latter two are more aligned with the Prandtl–Tomlinson type models and our specific system of interest. Nonetheless, we will consider results across all three types of systems. The majority of the studies considered are summarized in Table 2.1 for convenience.

**Table 2.1:** A summary of the main studies considered for the review of previous results in Sec. 2.5. The table provides a distinction between the different types of systems in the study: FFM, SFA or flake on a substrate, as well as whether they were numerically (num.) or experimentally.

System	Type	Year	Researcher	Materials	Keywords
FFM	Exp.	2007 [72]	Zhao et al.	Si <sub>3</sub> N <sub>4</sub> tip on graphite.	Temperature dependence.
		2015 [73]	G. Paolicelli et al.	Si tip, graphene on SiO <sub>2</sub> and Ni(111) substrate	Load, environment, graphene layers.
	Both	2019 [74]	Zhang et al.	Monolayer graphene	Straining of graphene sheet.
		2015 [75]	Yoon et al.	Si tip, graphene on SiO <sub>2</sub>	Stick-slip: tip size, scan angle, layer thickness, substrate flexibility.
	Num.	2016 [76]	Li et al.	Si tip, graphene on a-Si substrate	Graphene layers, friction strengthening, stick-slip
SFA	Num.	2011 [77]	Wijn et al.	Graphene flakes between graphite	Commensurability, rotational dynamics, superlubricity, temperature.
		2012 [37]	H. J. Kim and D. E. Kim.	Carbon sheet	Corrugated nano-structured surfaces
	Exp.	2005 [64]	Dienwiebel et al.	Graphene on graphite	Commensurability, superlubricity, load.
Flake	Exp.	2013 [78]	Feng et al.	Graphene on graphite	Commensurability, superlubricity, temperature.
		2009 [79]	Bonelli et al.	Graphene on graphite	Tight-binding, commensurability, load, flake size.
	Num.	2012 [80]	Reguzzoni et al.	Graphene on graphite	Graphite layers.
		2014 [81]	Liu et al.	Graphene on graphite	High speed, superlubricity, rotational dynamics, sheet strain.
		2018 [82]	P. Zhu and Li	Graphene on gold	Stick-slip, commensurability, flake size and shape.
		2019 [83]	Zhang et al.	Graphene on diamond	Temperature, commensurability, friction coefficient.

One of the earliest tribological simulations of graphene was carried out by Bonelli et al. [79] in 2009 using a tight-binding<sup>3</sup> method (excluding thermal excitations) to simulate a graphene flake on an infinite graphene sheet [71]. They implemented a Frenkel-Kontorova-Tomlinson-like setup where each atom in the flake is coupled horizontally to a rigid support by elastic springs. They recovered the stick-slip behavior, which is also observed in FFM setups both experimentally [72, 74] and numerically [76, 82]. Moreover, they found an agreement with the qualitative observation that soft springs allow for a clean stick-slip motion while hard springs ( $\sim 40 \text{ N/m}$ ) inhibited it, which also aligns with the Prandtl–Tomlinson model. In AFM and SFA experiments, the stick-slip motion tends to transition into smooth sliding when the speed exceeds  $\sim 1 \mu\text{s}$  while in MD modeling the same transition is observed in the  $\sim 1 \text{ m/s}$  region [24]. More precisely Liu et al. [81] finds this transition in MD simulations at  $15 \text{ m/s}$ . This 6-order-of-magnitude discrepancy has been largely discussed in connection to simplifying assumptions in MD simulations. On the other hand, the Prandtl–Tomlinson model qualitatively disagrees as it predicts smooth sliding for low speeds only. However, in an extension of the Prandtl–Tomlinson

<sup>3</sup>The tight-binding method involves computing the electronic structure of the system, but it uses a semi-empirical approach to reduce the computational cost of those calculations. Thus, this method lies between traditional MD and more expensive ab initio methods [84].

for the study of nanoscale rolling friction by Sircar and Patra [85], they found smooth sliding for high speeds as well.

Bonelli et al. [79] also found that commensurability, through orientation of the flake and the direction of sliding, had a great impact on the frictional behavior which generally aligns with the predictions of the Frenkel-Kontorova models. They confirmed qualitatively the observation of superlubricity for certain incommensurable orientations which has been reported in experiments by Dienwiebel et al.[64] and further supported by experimental measurements of interaction energies by Feng et al. [78]. The importance of commensurability is also reported for MD simulations [77, 82, 83]. Bonelli et al. found the friction force and coefficient to be one order of magnitude higher than that of the experimental results which they attribute to the details of the numerical modeling. Generally, the experimental coefficients between graphite and most materials lie in the range of 0.08–0.18 [64]. While Dienwiebel et al. [64] reported a wide range of frictional forces from  $28 \pm 16$  pN to  $453 \pm 16$  pN with loads  $\sim [-10, 20]$  nN, the change in friction with applied load was as low as 0.05–0.4% for the incommensurable orientations. When using the slope definition for the frictional coefficient (Eq. (2.2b)), this corresponds to a coefficient in the range of 0.0005–0.004. Bonelli et al. attribute the low dependency to a lacking change in contact area as the flake is loaded.

Furthermore, Bonelli et al. [79] found friction to decrease with increasing flake size which is also reported in MD simulations for graphene on gold [82]. Bonelli et al. mainly attribute this to boundary effects, but also note that the coupling to the support made for decreased rotational freedom as flake size was increased. Thus, they hypothesized that the decreased freedom led to the graphene taking a more forced path which is associated with a decreased stick-slip behavior. However, the general observation disagrees with the Frenkel-Kontorova models which predict the reverse; an increase in friction with increasing size.

An additional numerical study of monolayer islands of krypton on copper by Reguzzoni and Righi [86] supports the importance of commensurability regarding size effects. They report that the effective commensurability increase drastically below a critical flake radius on the order of 10 Å. In a numerical study by Varini et al. [87], based on Kr islands adsorbed on Pb(111), this is further elaborated as they found that finite size effects are especially important for static friction due to a pinning barrier arising from the edge, preventing otherwise superlubricity due to incommensurability. They reported a relationship  $F_s \sim A^{\gamma_s}$  not only sublinear,  $\gamma_s < 1$ , but also sublinear with respect to the island perimeter,  $P \propto A^{1/2}$ , by having  $\gamma_s = 0.25$  for a hexagonal edge and  $\gamma_s = 0.37$  when circular, indicating that only a subset of the edge is responsible for the pinning effect. This aligns with the general change in friction found by [82] for different flake geometries (square, triangle, circle). Additionally, Varini et al. found the edge pinning effect to decrease with increasing temperature as the edge energy barriers are reduced. Bringing all this together, the main picture forming is that flake size, which can be related to contact area, is affecting friction through a commensurability mechanism. If the flake is constrained in some way we might not observe the same dependency. While flake size nor contact area is easily measured in experimental FFM, Mo et al. [34] found in an MD simulation that friction is proportional to contact area for an indenting sphere on a nanoscale.

Evolution effects, or so-called friction strengthening, are also observed. That is, friction increases during the initial stick-slip cycles, which is observed experimentally by Zhang et al. [74] and numerically by Li et al. [76]. However, this is only found when having the graphene sheet resting on a substrate [74], as opposed to a suspended sheet. It is also found to diminish with an increasing number of graphene layers stacked (graphite) [76]. Multiple studies report a general decrease in friction with an increasing number of layers [73, 75, 76, 88, 89], but a few do also point towards the opposite trend [80].

A few numerical studies investigate friction under mechanical deformations. Zhang et al. [74] found that straining a suspended graphene sheet will lower the kinetic friction. They attribute this to a modulation of flexibility which consequently changes the local pinning capability of the contact interface. Liu et al. [81] carried out an MD simulation of high-speed (400 m/s) ballistic nanofriction of graphene on graphite. They found that a biaxial stretching of the graphitic substrate could be used to suppress frictional scattering and achieve persistent superlubricity. Another surface manipulating study was performed by H. J. Kim and D. E. Kim [37] who investigated the effects of corrugated nano-structured surfaces. The study revealed that corrugated surfaces, with altered contact areas and structural stiffness, could result in both increased or slightly decreased friction under certain load ranges. Altogether, these studies highlight the importance of surface structure and mechanical conditions.

The friction dependency of normal load turns out to be a complex matter and has proven to be a highly system-dependent feature. As already mentioned, asperity theory mainly points to a sublinear relationship between friction and load, while the reduced-models point to a more intricate relationship through the change of

the effective substrate potential which leads to an altering of the commensurability and the phonon dynamics. Experimentally rather different trends have been observed, although the majority agree on increasing friction with increasing load [1, p. 200]. For the graphene flake, Dienwiebel et al. [64] found a seemingly non-dependent relationship while FFM study by G. Paolicelli et al. [73] found a sublinear relationship matching the predictions of Maugis-Dugdale theory ( $F_f \propto (F_N - F_{N,0})^{2/3}$ ). The discrepancy might be attributed to the difference in system type; A spherical tip indenting the graphene sheet as opposed to the atomic flatness of the graphene-graphite interface, which does not make for a changing contact area under load. However, numerical studies using a graphene-graphite interface still find both sublinear [79] and linear [74, 83] load dependencies.

In an experimental FFM study by Deng et al. [15] it was discovered that the friction force kept increasing after unloading the probe tip from the graphite surface. This has been argued to be a general phenomenon related to hysteresis in the adhesive interaction between two sliding bodies [90]. Following the slope definition for the friction coefficient, these results correspond to a negative friction coefficient. More recently, a negative friction coefficient has also been observed for the loading phase by Liu et al. [16] in an experimental study of the interface between graphite and muscovite mica heterojunction. With supporting numerical modeling this is attributed to “synergetic and nontrivial redistribution of water molecules at the interface”. Similar results are also reported numerically by [17] for graphite in contact with hexagonal boron nitride heterojunctions which is attributed to “load-induced suppression of the moiré superstructure out-of-plane distortions leading to a less dissipative interfacial dynamics”. Thus, the concept of a negative friction coefficient has been proven for the unloading phase of adhesive contacts and in the loading phase for a few systems.

The dependency of velocity is generally found to increase logarithmically with velocity in experimental AFM studies [1, p. 201] which match the low-velocity regime of the Prandtl–Tomlinson type models. At higher velocities, thermally activated processes are less important and friction becomes independent of velocity according to the Prandtl–Tomlinson model result Eq. (2.7) when ignoring the athermal regime. Saturation of the velocity dependency has been observed numerically for Si tips interacting with diamond, graphite and amorphous carbon surfaces respectively with scan velocities above  $1\text{ }\mu\text{/s}$  [91]. Guerra et al. [92], studying gold clusters on graphite using MD simulations, found a viscous friction response, friction being proportional to sliding velocity, in both low and high speed domains. However, thermal effects reversed as they found friction to decrease with increasing temperature at low speed (diffusive regime) but found friction to increase with temperature at high speed (ballistic regime). This crossover from the ballistic to diffusive regime occurred between  $10$  and  $1\text{ m/s}$ .

Regarding temperature, the general experimental trend is decreasing friction with increasing temperature as found by Zhao et al. [72] in a series of AFM graphene on graphite experiments yielding  $F_{\text{fric}} \propto \exp(1/T)$ . This agrees with the thermal drift regime of the Prandtl–Tomlinson model even though the exact temperature range does not agree. Moreover, Wijn et al. [77] found that friction commensurability can be lost at higher temperatures (above  $200\text{ K}$ ) where they found a power law behavior  $F_k \propto T^{-1.13 \pm 0.04}$ . Numerically, Zhang et al. [83] found that friction increased with temperature, using a sliding speed of  $10\text{ m/s}$ . Considering the findings of [92] this qualitative different behavior might be attributed to an MD related effect associated with the transition from low speed diffusive behavior to high speed ballistic behavior.

From the review of previous results, we find several gaps and discrepancies in the description of friction provided by the reduced-models, MD simulations and experimental methods respectively. Some of the discrepancies can be attributed to the fact that different physical mechanisms are considered in the numerical modeling. The reduced-models provide a simplistic description, while the MD simulations are expected to capture a more complex behavior. We might also point to differences in the studied systems as an important factor to consider. This includes the physical conditions such as sliding speed and temperature, but also higher-level features related to the mechanical properties of the system. For instance, the FFM based results consider an asperity-like system where the tip is expected to deform under loading, which gives rise to a change in the contact area. This feature is lacking in the flat flake-/sheet-systems, and thus we might question the role of the contact area in these systems. More precisely, when inflicting an out-of-plane buckling through Kirigami cuts and stretching, the contact area is expected to decrease as well. Based on the asperity theory, we can expect a decrease in friction during the transition. However, as the system undergoes deformation, it may also lead to a change in commensurability, which can result in significant modifications to the frictional behavior due to its effect on stick-slip behavior. Based on the results obtained from a non-cut sheet under tension, there are indications that stretching can lead to a reduction in friction, even without taking into account the contact area. Similarly, the findings from a corrugated nano surface suggest that surface stiffness may also be a significant factor in determining friction.

## 2.6 Research questions

Based on the review of friction presented in Chapter 2, it is evident that the behavior of friction is influenced by various factors, such as the specific system under investigation, the numerical modeling approach, and the physical conditions related to the environment and the probing of friction. In our study, we aim to investigate the frictional behavior of a Kirigami sheet under the effects of strain. Previous studies have demonstrated that strained Kirigami sheets are prone to out-of-plane buckling [6, 7] which is indicative of a possible transition between two distinct systems: An atomically flat interface and an asperity system. These systems are usually only studied separately, and therefore, our primary objective is to investigate the possible frictional effects linked to strain-induced system transformations. In particular, we want to investigate the significance of the contact area and evaluate the hypothesis that reducing the contact area will lead to a decrease in friction. Additionally, we seek to examine the relationship between the friction-load curve and this phenomenon. For the sake of contributing new insight to the field of nanoscale friction, we are interested in non-linear dependencies between friction and stretching of various Kirigami designs. Drawing on this perspective, we aim to investigate the prospects of achieving a negative friction coefficient for a system of coupled load and strain. In order to contextualize our findings within the theoretical framework, we will take into account the results from prior studies.

To gain a more comprehensive understanding of the potential applications of Kirigami design, we aim to develop a dataset based on MD simulations that capture the frictional effects on Kirigami designs when subjected to strain and load. We intend to employ machine learning techniques to discern any meaningful trends in the data that may be used to inform future research endeavors. Specifically, we seek to leverage the machine learning model to facilitate an accelerated search for optimizing specific frictional properties. Our focus will be on evaluating the prospects of reducing or increasing the friction force, as well as reducing or increasing the friction coefficient for a coupled system of load and strain. Our main research questions can be summarized as follows.

1. How can we design an MD simulation that provides a reliable foundation for an investigation of the frictional behavior for a Kirigami graphene sheet sliding on a substrate? How do physical conditions such as temperature and sliding speed control friction?
2. How can we design an ensemble of Kirigami patterns for the investigation of its frictional properties with the scope of getting out-of-plane buckling and also randomized design features?
3. Can we control friction for a Kirigami sheet through Kirigami pattern design and straining of the sheet?
  - (a) Does friction dependent on a changing contact area?
  - (b) How does the friction-load curve relate to strained Kirigami sheets?
  - (c) Are the effects of strain and pattern design significant when considered independently?
4. Is it possible to utilize machine learning techniques to identify general trends in the relationship between friction and kirigami patterns, strain and load?
5. Can we use a trained machine learning model to predict new designs through an accelerated search?
6. What are the prospects of achieving a negative friction coefficient for a system of coupled load and strain through Kirigami design?

## **Part II**

# **Simulations**



# Chapter 3

## Pilot study

Having defined our system, we carry out an initial study of the frictional properties. First, we evaluate the numerical results for a non-cut sheet in order to define suitable metrics for a numerical evaluation of friction and justify some of the default parameter choices. This provides a basis for the following study where we consider the Tetrahedron and Honeycomb Kirigami patterns as well. We conduct a more systematic investigation of the friction dependencies to temperature, sliding speed, spring constant and timestep. Finally, we consider the mean friction of all three configurations when stretched. This includes an analysis of the dependence to contact area and the friction-load curves.

### 3.1 Friction simulation parameters

The MD simulations we will carry out to measure friction are governed by a small set of parameters. For the purpose of creating a machine learning we need to standardize these parameters. This we keep most of them constant with only a small subset of parameters being varied: sheet configuration, strain and load. Instead of starting with the parameter selection process, we first state the final choice in Table 3.1. Due to the great number of parameters, we do not make an exhaustive search of all parameters before deciding on the final settings. Instead, we take a basis in parameters used in similar friction simulations [75, 76, 81–83] and adjust accordingly to the aim of getting stable measurements and reducing computation time where possible. Parameters such as initial relaxation time, pauses and strain speed are chosen mainly from the results of initial stability tests. The sheet and pull block sizes are chosen with a consideration of the balance between Kirigami design options and computational resources. The scan direction is chosen to be parallel to the connection line between the pull blocks. This is mainly chosen in order to avoid unecessary complexity in the motion since it can be hypothesized that the center of the sheet can drag behind for other scan directions. The remaining parameters: Temperature  $T$ , sliding speed  $v_{\text{slide}}$ , spring constant  $K$ , normal load  $F_N$ , timestep  $dt$  and sliding distance have been chosen because the friction output remains relatively stable with moderate perturbations around these default values. We will explain this in more detail later in the chapter. Note that the default values in Table 3.1 will be used when nothing else is stated explicitly.

**Table 3.1:** Parameters involved for the numerical MD simulation for measuring friction. The default values correspond to the final choice used for the dataset. The shaded cells denote the parameters varied in the ML dataset.

Parameter	Default value	Description
$T$	300 K	Temperature of the system.
$v_{\text{slide}}$	20 m/s	Sliding speed for the sheet translation.
$K$	$\infty$	Spring constant for the coupling between the virtual atom and the sheet pull blocks.
Scan direction	$(x, y) = (0, 1)$ (zigzag direction)	The direction for which we translate the sheet.
Sheet configuration	Contiguous	Binary mapping describing which atoms are removed (0) and which is still present (1) in the graphene sheet.
Strain amount	[0, rupture]	The ratio of change in length to the original length.
$F_N$	[0.1, 10] nN	Applied normal force to the pull blocks.
$dt$	1 fs	MD integration timestep.
Initial relaxation time	15 ps	Initial relaxation time before straining.
Pauses	5 ps	Relaxation pauses after strain, and during the normal load phase (before translating the sheet).
Strain Speed	$0.01 \text{ ps}^{-1}$	The rate of straining for the sheet.
Slide distance	400 Å	How far the sheet is translated.
Sheet size	$130.029 \times 163.219 \text{ \AA}$	Spatial 2D size of the sheet.
Pull block size	$2 \times 130.029 \times 15.183 \text{ \AA}$	Spatial 2D size of the pull blocks.

## 3.2 Force traces

We begin by assessing the friction force traces, i.e. force vs. time curves, for a single friction simulation using the default parameters shown in Table 3.1 for a non-cut sheet with no stretch applied and a normal load of 1 nN.

### 3.2.1 Force oscillations

We evaluate the friction force as the force acting on the sheet from the substrate. We consider initially the force component  $F_{\parallel}$  parallel to the drag direction as plotted in Fig. 3.1. We use a sample rate of  $10 \text{ ps}^{-1} = 100 \text{ timesteps}^{-1}$  for which each sample is the mean value of the preceding 100 timesteps. We observe immediately that the data carries oscillations on different time scales which match our general expectations for sliding involving periodic surfaces. By applying a Savgol filter to the data with a polynomial order of 5 and a window length of 150 timesteps (corresponding to a sliding distance of 3 Å or a time window of 15 ps) we can qualitatively point out at least two different frequencies of oscillation. During the first 10 Å of sliding, seen in Fig. 3.1a, we see roughly three waves on the Savgol filter corresponding to a relatively high frequency, while for the duration of 100 Å of sliding, seen in Fig. 3.1b, the same Savgol filter reveals a lower frequency on top, creating the visual pattern of a wavepacket. The data does not indicate clear signs of stick-slip behavior as otherwise found in other studies, e.g. by Zhu and Li [82] for graphene on gold, who saw a more typical saw tooth shape in the force trace. Besides the difference in the substrate material, using gold instead of silicon, they used a lower sliding speed of 10 m/s and a soft spring of  $K = 10 \text{ N/m}$ . By adopting these parameters we get a slightly different force trace behavior as shown in Fig. 3.1c and Fig. 3.1d. This change breaks the symmetry in the force oscillations but still does not produce any significant discontinuities in the trace. By keeping the spring constant  $K = 10 \text{ N/m}$  and lowering the sliding speed further down to 1 m/s we are able to demonstrate a proper stick-slip behavior as shown in Fig. 3.1e and Fig. 3.1f. Considering all three simulations we might classify the results from the default settings,  $K = \text{inf}$ ,  $v = 20 \text{ m/s}$ , as smooth sliding,  $K = 10 \text{ N/m}$ ,  $v = 10 \text{ m/s}$ , as a transition phase with possible occasional slipping, and  $K = 10 \text{ N/m}$ ,  $v = 1 \text{ m/s}$  as certain stick-slip behaviour.

This confirms the qualitative observation the stick-slip behavior is suppressed with stiff springs [79] springs and high sliding velocity [81]. Having a low sliding speed comes with a high computational cost which is the reason that we choose a relatively high sliding speed of 20 m/s. The choice of an infinite spring constant is related to the stability of the measurements and is discussed later in this chapter make sure it is, maybe make a reference.

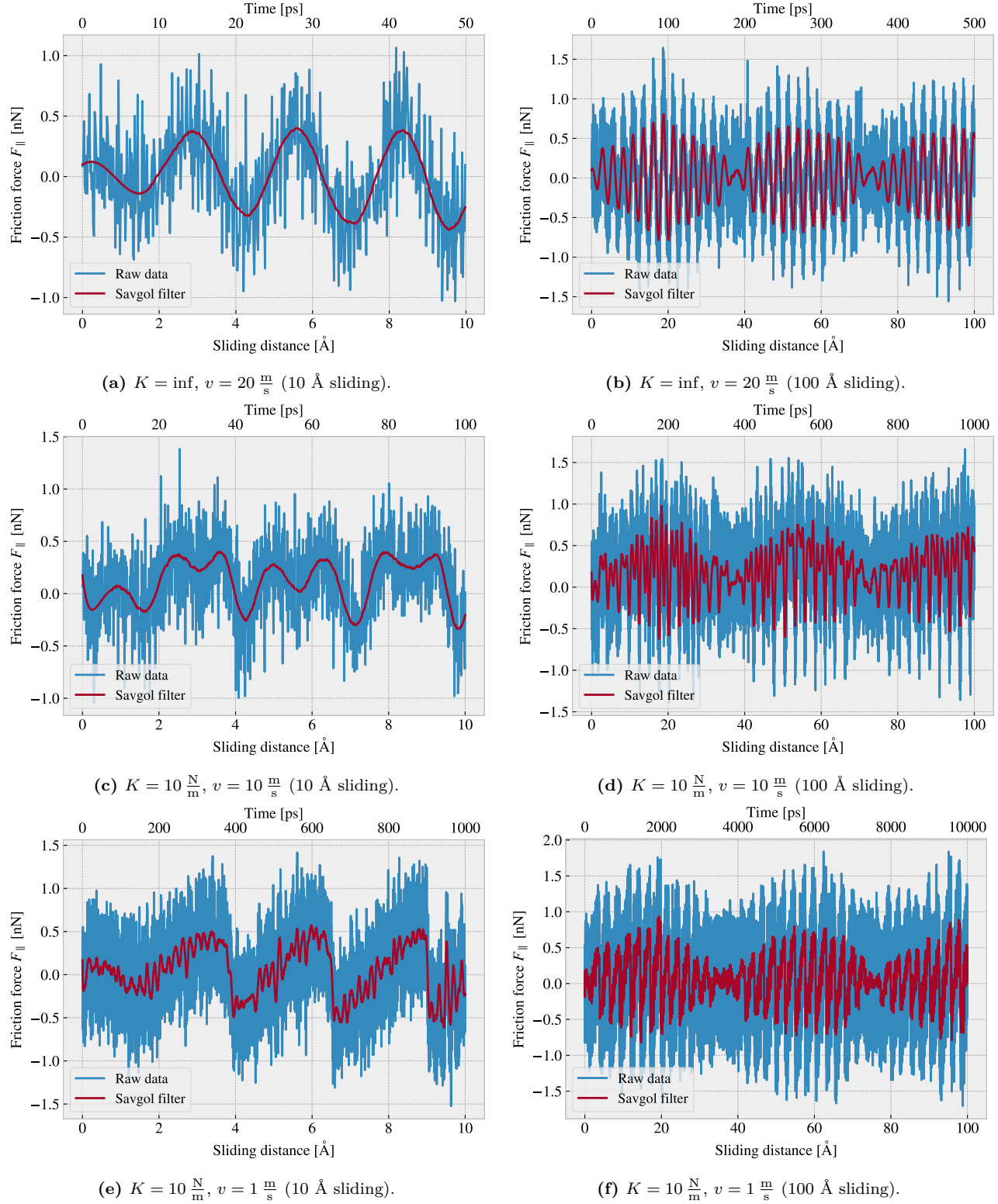


**Figure 3.1:** Force traces of the friction force  $F_{\parallel}$  with respect to the drag direction acting from the substrate on the full sheet. The force traces are plotted against the sliding distance (lower x-axis) and the corresponding sliding time (upper x-axis). The sliding distance is measured by the displacement of the virtual atom tethering the sheet. The red line represents a Savgol filter with polynomial order 5 and a window length of 150 timesteps (corresponding to a sliding distance of 3 Å or a time window of 15 ps). Each row, (a,b), (c,d), (e,f), represents a different choice of the spring constant  $K$  and sliding speed  $v$ , while the columns show the same result for two different time scales. The default settings are represented in figure (a) and (b).

By performing a Fourier Transform on the data, using the default parameters, we can quantify the leading frequencies observed in figure Fig. 3.1a and Fig. 3.1b. The Fourier transform is shown in Fig. 3.2a, and by plotting the two most dominant frequencies  $f_1 = 0.0074 \text{ ps}^{-1}$  and  $f_2 = 0.0079 \text{ ps}^{-1}$  as a sine sum,  $\sin(2\pi f_1) + \sin(2\pi f_2)$ , we find a qualitatively convincing fit to the observed wavepacket shape as seen in Fig. 3.2b. We can convert the frequencies according to that of a wavepacket. By using the trigonometric identity

$$\begin{aligned}\sin(a+b) &= \sin(a)\cos(b) + \cos(a)\sin(b), \\ \sin(a-b) &= \sin(a)\cos(b) - \cos(a)\sin(b),\end{aligned}$$

and decomposing the frequencies as  $f_1 = a - b$ ,  $f_2 = a + b$ , we can rewrite the sine sum as the sinusoidal product

$$\begin{aligned}\sin(2\pi f_1) + \sin(2\pi f_2) &= \sin(2\pi(a-b)) + \sin(2\pi(a+b)) \\ &= \sin(2\pi a)\cos(2\pi b) + \cancel{\cos(2\pi a)\sin(2\pi b)} + \sin(2\pi a)\cos(2\pi b) - \cancel{\cos(2\pi a)\sin(2\pi b)} \\ &= 2\sin(2\pi a)\cos(2\pi b),\end{aligned}$$

with

$$\begin{aligned}a &= \frac{f_1 + f_2}{2} = 0.0763 \pm 0.0005 \text{ ps}^{-1}, & b &= \frac{f_2 - f_1}{2} = 0.0028 \pm 0.0005 \text{ ps}^{-1}, \\ &= 0.381 \pm 0.003 \text{ \AA}^{-1}, & &= 0.014 \pm 0.003 \text{ \AA}^{-1}.\end{aligned}$$

In the latter transition, we have denoted the frequency with respect to the sliding distance by considering the default sliding speed of 20 m/s = 0.2 Å/ps. This makes us recognize the high oscillation frequency as  $a$  and the low frequency as  $b$ . The faster one has a period of  $T_a = 2.62 \pm 0.02 \text{ \AA}$ <sup>4</sup> which corresponds well with the magnitude of the lattice spacing and especially that of graphene at 2.46 Å as expected theoretically. The longer period  $T_b = 71 \pm 15 \text{ \AA}$  is not obviously explained. We notice a similarly long period oscillation for all three cases Fig. 3.1b, Fig. 3.1d and Fig. 3.1f, and thus we have no reason to believe that this is dependent on the stick-slip behavior. The initial build-up in friction force is reminiscent of friction strengthening, which is often reported [74, 76], but the periodicity goes against this idea. Instead, we might attribute it to some phonon resonance which could be a physical phenomenon or simply a feature of our MD modeling.

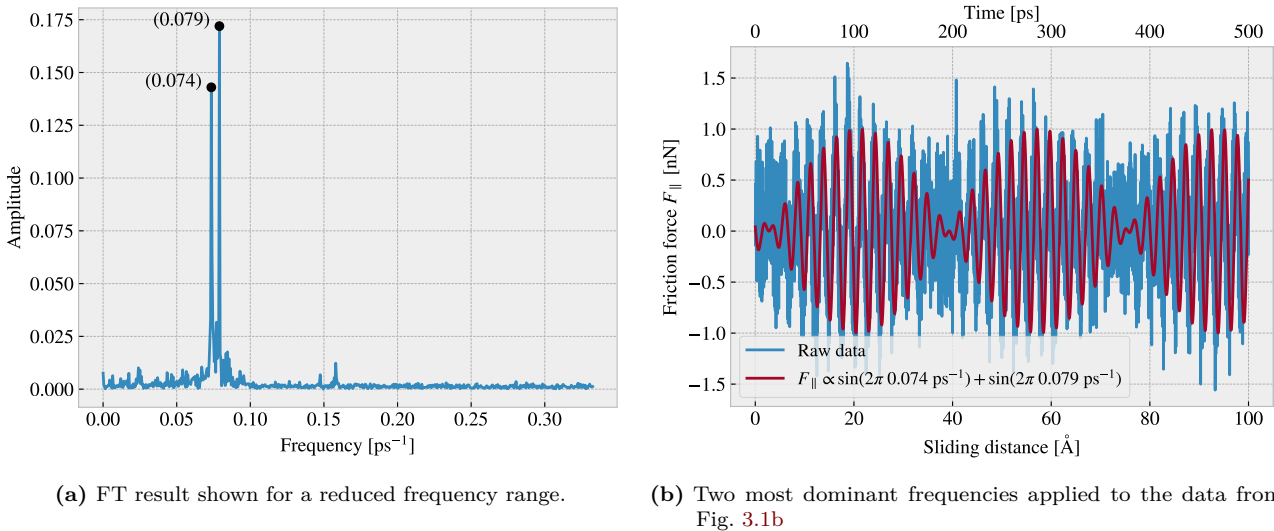


**Figure 3.2:** Fourier transform analysis of the full friction force data (all 400 Å sliding distance) shown in Fig. 3.1. (a) shows the two most dominant frequency peaks. Note that no significant peaks were found in a higher frequency than included here. (b) shows a comparison between the raw data and the wavefunction corresponding to the two peaks in figure (a).

<sup>4</sup>The uncertainty  $\Delta y$  is calculated as  $\Delta y = \left| \frac{\partial y}{\partial x} \Delta x \right|$  for uncertainty  $\Delta x$  and  $y(x)$

### 3.2.2 Decompositions

In the previous analysis, we looked only at the friction force for the full sheet, including the rigid pull blocks, and with respect to the drag direction. We found this way of measuring the friction force to be the most intuitive and reliable, but we will present the underlying arguments for this choice in the following.

Since we are only applying cuts to the inner sheet, and not the pull blocks, it might appear more natural to only consider the friction inner sheet. If the desired frictional properties can be achieved by altering the inner sheet one can argue that any opposing effects from the pull blocks can be mitigated by simply scaling the relative size between the inner sheet and the pull blocks. However, when looking at the force traces decomposed with respect to the inner sheet and pull block regions respectively in Fig. 3.3a, we observe that the friction force arising from those parts is seemingly antisymmetric. That is, the distribution of the frictional pull from the substrate on the sheet is oscillating between the inner sheet and the pull blocks. Keeping in mind that normal force is only applied to the pull blocks we might take this as an intrinsic feature of the system that does not necessarily disappear with a scaling of the spatial ratio between the inner sheet and pull blocks. Any interesting friction properties might depend on this internal distribution of forces. Hence, we hedge our bets and use the full sheet friction force as a holistic approach to avoid excluding relevant information in the measurement data.

Similarly, we might question the decision of only considering the frictional force projected onto the sliding direction as we are then neglecting the “side shift” induced during sliding. In Fig. 3.3b we show the decomposition in terms of the force components parallel  $F_{\parallel}$  and perpendicular  $F_{\perp}$  to the sliding direction respectively. We notice that the most dominant trend appears for the parallel component. If we want to include the perpendicular component as well we would have to evaluate friction as the length of the force vector instead. However, this would remove the sign of the force direction and shift the mean friction force up as we see both negative and positive contributions in the parallel force trace. One option to accommodate this issue is by using the vector length for the magnitude but keeping the sign from the parallel component. However, we omit such compromises as this might make the measurement interpretation unnecessary complex, and we use only the parallel component going forward.

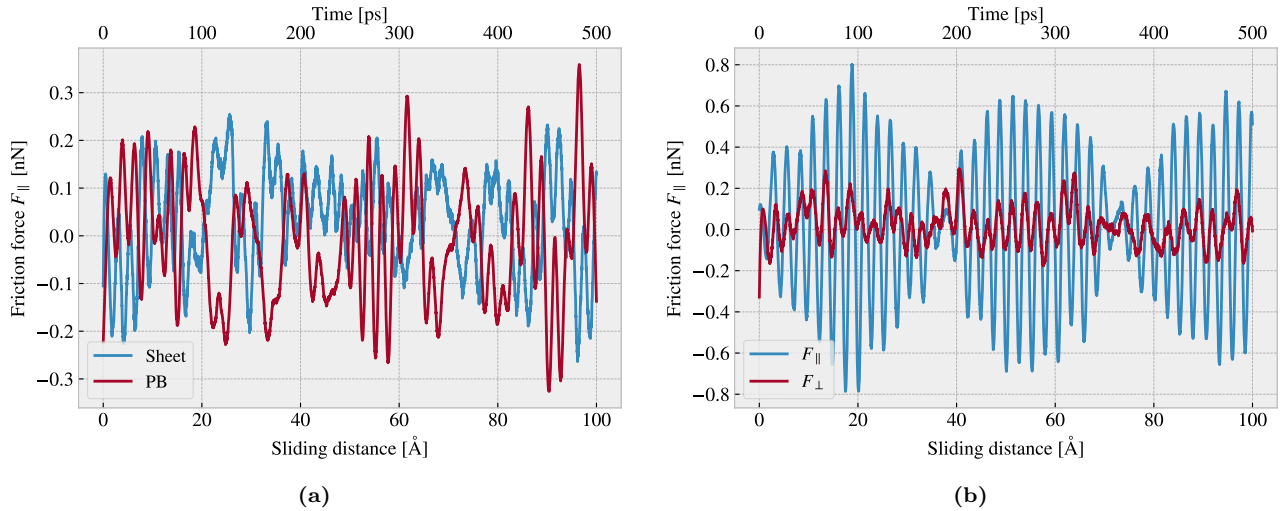


**Figure 3.3:** Friction force decomposition on the default parameter force trace shown in Fig. 3.1 showing only the applied Savgol filters. (a) Decomposition into group inner sheet (sheet) and pull blocks (PB). (b) Decomposition into parallel ( $F_{\parallel}$ ) and perpendicular ( $F_{\perp}$ ) to drag sliding direction.

### 3.2.3 Center of mass path

From the previous observations of the force traces in Fig. 3.1 we found both smooth sliding and stick-slip behavior depending on the sliding speed and spring constant. Considering the force decomposition in Fig. 3.3b we know that a frictional force in the perpendicular direction to sliding is also present. By looking at the  $x, y$ -position for the sheet Center of Mass (CM) we find a qualitatively different behavior when reconsidering the spring constants and sliding speeds investigated in Fig. 3.1. These results are shown in Fig. 3.4. The default case in Fig. 3.4a shows a rather straight path forward with only a small side motion in comparison to the cases

in Fig. 3.4b and Fig. 3.4c. However, the CM accelerates and deaccelerates with a high frequency, much too high to be associated with the lattice spacing on the order of  $2.46\text{ \AA}$ . One possible explanation is that the sheet and substrate constitute an incommensurable contact for which traveling kink excitations make the atoms move in such a way that the sheet CM is incremented in small ‘‘burst’’. When looking at the  $K = 10 \frac{\text{N}}{\text{m}}$ ,  $v = 10 \frac{\text{m}}{\text{s}}$  case in Fig. 3.4b we see a completely different CM path where the rapid movements aligns visually better with the force oscillations shown earlier in Fig. 3.1d. The CM accelerates forward and then deaccelerates in combination with a side motion that leads to the CM path making a loop as it slows down. Finally we have the  $K = 10 \frac{\text{N}}{\text{m}}$ ,  $v = 1 \frac{\text{m}}{\text{s}}$  in Fig. 3.4b which is confirmed to have stick-slip behavior in Fig. 3.1f. Here the CM path shows a more chaotic movement between acceleration, but with the rapid parts aligning which also visually well with the timing of the slips seen in Fig. 3.1f. The chaotic motion is not connected to the stick-slip motion, but we might associate it with the thermal contributions being dominant in this regime.

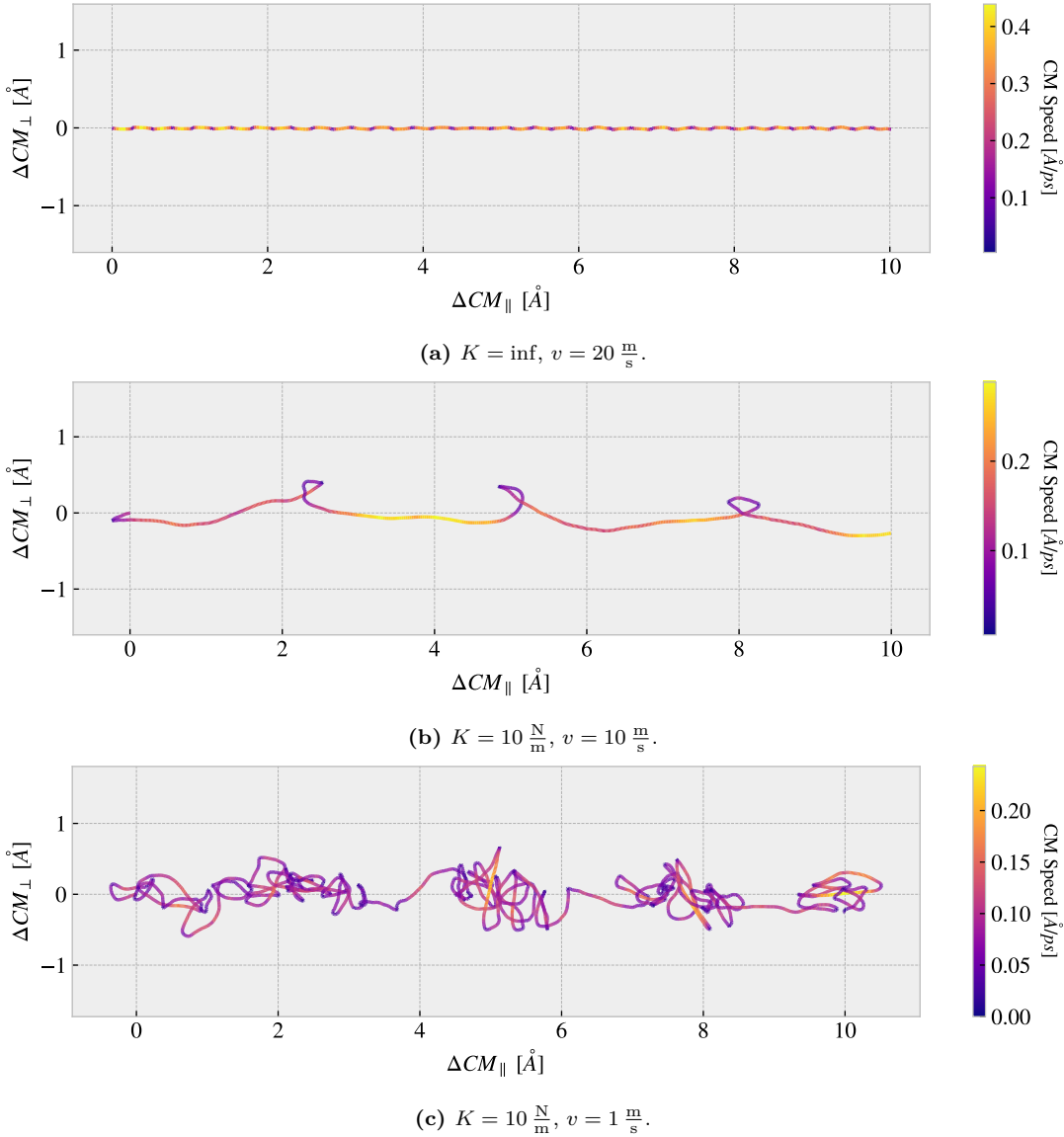


**Figure 3.4:** Center of Mass (CM) position relative to the start of the sliding phase in terms of the direction parallel to the sliding direction  $\Delta COM_{\parallel}$  and the axis perpendicular to the sliding direction  $\Delta COM_{\perp}$ . The colorbar denotes the absolute speed of the CM motion. Figure a-c shows different parameters used for the spring constant  $K$  and sliding speed  $v$  similar to that used in Fig. 3.1. (a) Default:  $K = \infty$ ,  $v = 20 \frac{\text{m}}{\text{s}}$ . (b)  $K = 10 \frac{\text{N}}{\text{m}}$ ,  $v = 10 \frac{\text{m}}{\text{s}}$ . (c)  $K = 10 \frac{\text{N}}{\text{m}}$ ,  $v = 1 \frac{\text{m}}{\text{s}}$

### 3.3 Defining metrics for friction

In order to evaluate the frictional properties of the sheet we aim to reduce the force trace results, addressed in section Sec. 3.2, into single metrics describing the kinetic and static friction respectively.

#### 3.3.1 Kinetic friction

We measure kinetic friction as the mean of the friction force trace. More precisely, we take the mean value of the last half of the dataset in order to ensure that we are sampling from a stable system. For a full sliding simulation of 400 Å our mean value will be founded on the last 200 Å (1000 ps) of sliding. In Fig. 3.5a we have shown the force trace for the first 10 Å of sliding together with a 50% running mean window. The choice of such a short sliding distance is merely to illustrate the sampling procedure, and we see that the final mean estimate (marked with a dot) takes a negative value due to the specific cut-off of the few oscillations captured here. Nonetheless, one approach to quantify the uncertainty of the final mean estimate is to consider the variation of the running mean preceding the final mean value. The more the running mean fluctuates the more uncertainty associated with the final estimate. Only the running mean “close” to the ending should be considered, since the first part will rely on data from the beginning of the simulation. From the Fourier analyze in section Sec. 3.2.1 we found the longest significant oscillation period to be  $\sim 71$  Å. Hence, we find it reasonable to use the standard deviation (std) for the last  $\sim 71$  Å of the running mean window to evaluate the fluctuations. When including the full sliding length this corresponds to the last  $\sim 35\%$  of the running mean window. We consider the std as an estimate of the absolute error and calculate the relative error by a division of the final mean value. In Fig. 3.5b we showcase a running relative error based on the std, with a window of length 35% the mean window, in a continuation of the illustrative case of a 10 Å sliding from Fig. 3.5a. In this case, we get an extremely high relative error of  $\sim 257\%$ , but this is consistent with the fact that the short sampling period leads to an unphysical negative value which should be associated with high uncertainty.

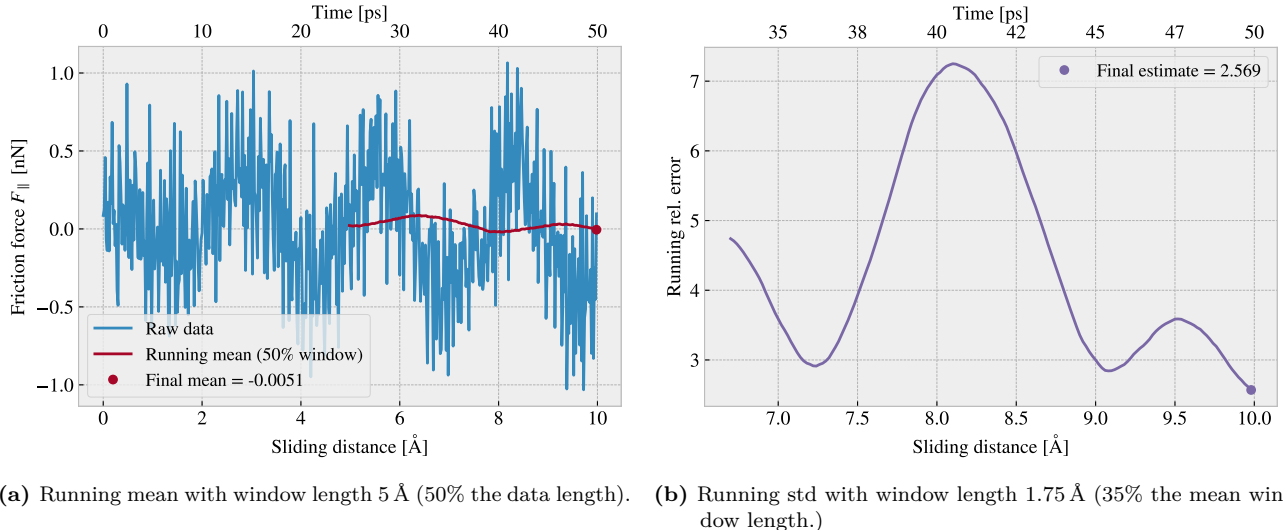


**Figure 3.5:** Running mean (a) and running relative error (std) (b) on the friction force data from a reduced sliding distance of 10 Å. The running mean window is 50% the data length while the running std window is 35% the running mean window length. The values are plotted at the end of their respective windows such that window precedes the actual point on the graph.

When including the full dataset of 400 Å of sliding, such that the std window actually matches with the longest period of oscillations expected, we get a final relative error of  $\sim 12\%$  as shown in fig Fig. 3.6. This is arguable just at the limit of an acceptable error, but as we shall see later on in Sec. 3.6 this high relative error is mainly associated with the cases of low friction. When investigating different configurations under variation of load and strain we see a considerably lower relative error as the mean friction evaluates to higher values. One interpretation of this finding is simply that the oscillations in the running mean are to some degree independent of the magnitude of the friction. In that case, the relative error will spike for the low friction cases, and the

absolute error might be the more reliable measure, i.e. using simply the std without dividing by the final mean value.

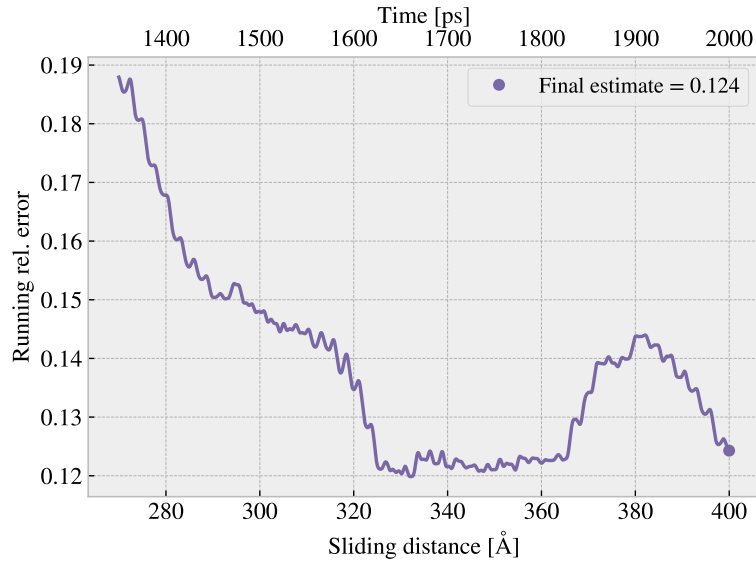


**Figure 3.6:** Running standard deviation (std) for a full 400 Å sliding simulation. The running std window is 70 Å (35% the running mean window of 50% the data length).

### 3.3.2 Static friction

The maximum value is one of the common choices for addressing static friction, even though the definition of static friction is a bit vague. When considering the force traces in Fig. 3.1 we observe that the force oscillations increase in magnitude toward a global peak at  $\sim 20$  Å. Thus, one could be inclined to identify this peak as the maximum value associated with the static friction force. However, as we have already clarified, this steady increase in friction is part of a slower oscillation that repeats by a period of  $\sim 71$  Å. By plotting the top three max values recorded during a full 400 Å simulation, for 30 logarithmically spaced load values in the range [0.1, 100] nN, we observe that the global max rarely falls within this first oscillation period as shown in Fig. 3.7. Only 2 out of 30 global maxima and 4 out of 90 top three maxima can be associated with the start of the sliding by this definition. Thus, this result suggests that our default system does not yield a static friction response in the sense of an initial increase in friction due to a depinning of the sheet from the static state. Some parameter changes that might increase the likelihood of seeing a significant static friction response are either extending the relaxation period since static friction is theorized to increase logarithmically with time [28], or increasing the sliding force more slowly through a soft spring tethering. As an attempt to test the latter part of this hypothesis we run a series of simulations with varying spring constant,  $K \in [5, 200]$  nN including also  $K = \infty$ , but keeping the relaxation time and sliding speed at the default values. The result is shown in Fig. 3.8 and do not show any support for the hypothesis that a softening of the spring constant will eventually lead to the friction maximum occurring in the first period of sliding. We note that this might be suppressed by having a too short relaxation period or a too high sliding speed (related to the initial force increase), but due to the ambiguousness in the assessment of the static friction we will mainly concern ourselves with the kinetic friction in the remaining of this thesis.

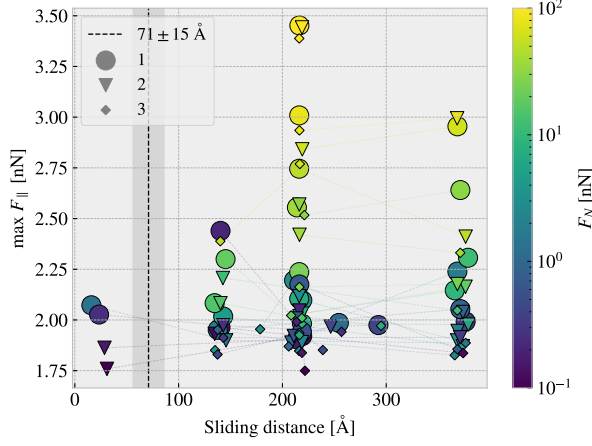


**Figure 3.7:** Distribution of top three max friction force peaks for 30 uniformly sampled normal forces  $F_N \in [0.1, 10]$  nN. The dotted line and the grey area mark the slowest significant oscillation period found in the data and thus marking a dividing line for whether a peak falls within the “beginning” of the sliding simulation.

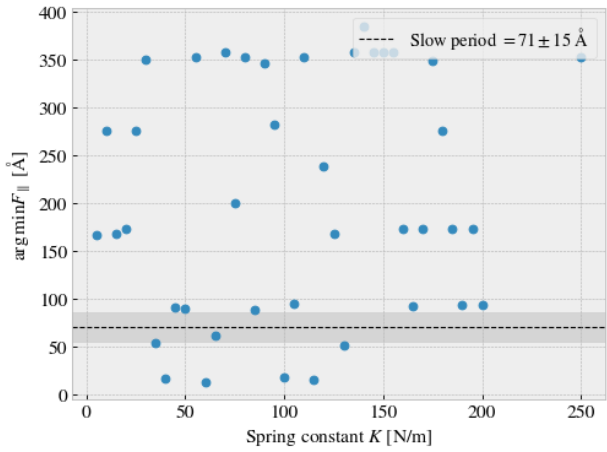


**Figure 3.8:** Sliding displacement for the max friction peak to appear as a function of spring constant. Fixmove is tmp mapped to  $K = 200$  here without any discontinuous lines.

### 3.4 Out-of-plane buckling

The out-of-plane buckling is one of the motivations for investigating the application of Kirigami cuts in the context of friction properties. Therefore, we perform a stretch simulation, at low temperature ( $T = 5$  K) without any substrate, in order to verify that we can reproduce an out-of-plane buckling with the Tetrahedron and Honeycomb patterns intended for our study (see ??). For this investigation we consider the Tetrahedron (7, 5, 1) and the Honeycomb (2, 2, 1, 5) pattern in comparison to the non-cut sheet. We quantify the out-of-plane buckling by assessing the distribution of atoms along the z-direction (perpendicular to the plane) during stretching. We calculate the minimum and maximum z-value as well as the atom count quartiles 1%, 10%, 25%, 50% (median), 75%, 90% and 99% as shown in Fig. 3.9. The results show significant buckling for the Tetrahedron and Honeycomb patterns in comparison to the non-cut sheet which only exhibits minor buckling of  $\sim 2$  Å which is on the same order as the lattice spacing. Moreover, we notice that the Tetrahedron pattern buckles more in consideration to the min. and max. peaks while the remaining quantiles seem to be more closely spaced than for the Honeycomb. By addressing the simulation results visually, using the *Open Visualization Tool OVITO*, we find that this can be attributed to fringes on the edge “flapping around” and thus increasing the min. and max. values.

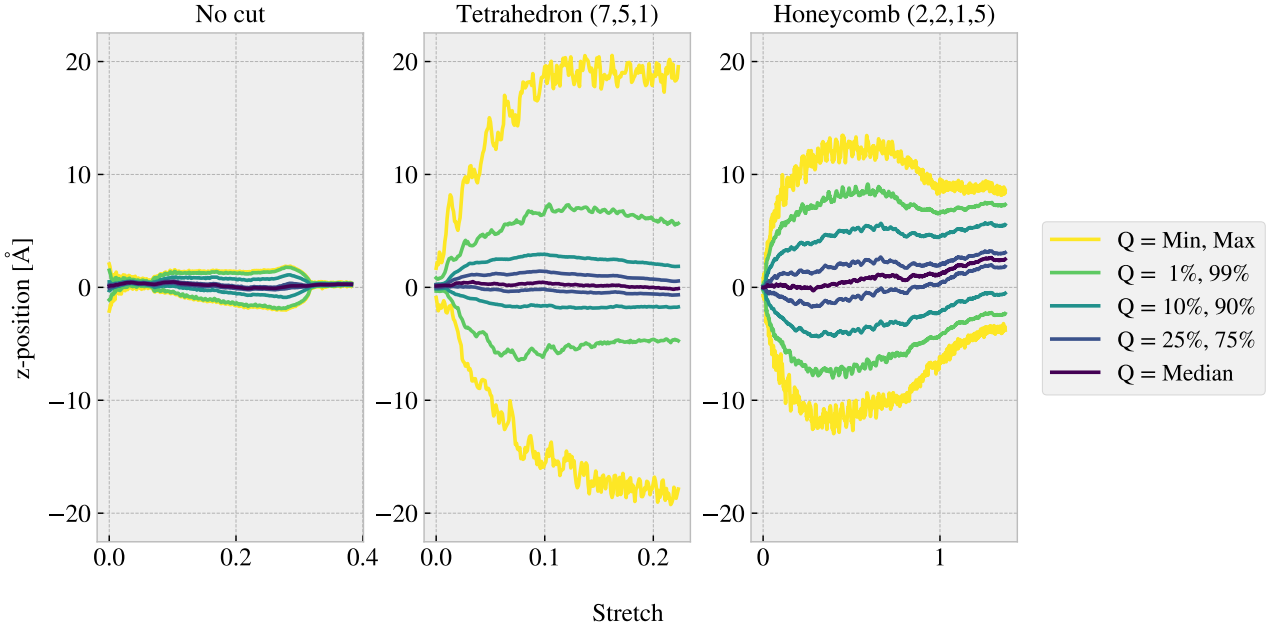


**Figure 3.9:** Out-of-plane buckling during stretching of the No cut, Tetrahedron (7, 5, 1) and Honeycomb (2, 2, 1, 5) sheet respectively in vacuum at low temperature  $T = 5$  K. The buckling is measured by the distribution of the atom z-position (perpendicular to the sheet plane), for which the colors indicates selected quantiles. The yield strain were, reading from left to right, 0.38, 0.22 and 1.37.

Given the confirmation of out-of-plane buckling in a vacuum, as seen in Fig. 3.9, we reintroduce the substrate in order to investigate whether this effect carries over to a changing contact area. For this simulation we raise the temperature to the default value of  $T = 300$  K. We keep the normal force off and let the sheet stick purely by the adhesion forces between the sheet and substrate. We quantify the contact area through the relative amount of atoms in the sheet within chemical range of the substrate. The cut-off for this interaction is set to 4 Å, inspired by [76], corresponding to  $\sim 120\%$  the LJ equilibrium distance. Usually, the contact area is calculated as the number of contacting atoms multiplied by an associated area for each atom. However, since we are not interested in the absolute value of the area, but rather the relative change, we omit the multiplication factor. That is, we consider the relative number of atoms within the contact range, which is proportional to the contact area, as our metric of choice. The relative contact for the three configurations (No cut, Tetrahedron (7, 5, 1) and Honeycomb (2, 2, 1, 5)) during stretching are shown in figure Fig. 3.10. The figure reveals a significant drop in contact as the sheets are stretched, which agrees qualitatively with the buckling observed in Fig. 3.9 without the substrate. The Honeycomb pattern turns out to be both the most stretchable, with a rupture strain of 1.27, and the one with the biggest decrease in relative contact with a minimum of approximately 43%. Notice, that the relative contact is never actual 1.0 but instead reaches a maximum of 96% with no stretching. This is attributed to the temperature fluctuations and the choice of cut-off. Thus we might

Selected frames from the simulation result are shown in ?? which reveals a bit more information on how the buckling occurs. The Tetrahedron pattern deforms rather quickly and smoothly into small tetrahedron spikes, as the name suggests. In the Honeycomb pattern, on the other hand, the deformations initiate from one side first. As the sheet stretches more rows of the pattern are activated, producing the honeycomb-looking shape when seen from above. Both patterns exhibit a small increase in relative contact when they are approaching their yield strain, which agrees with the results from Fig. 3.9 where the buckling reduces slightly towards the rupture strain.

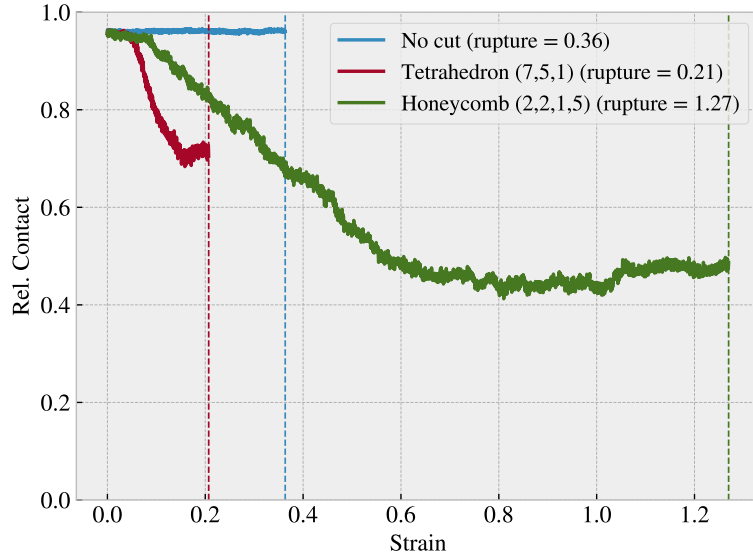


**Figure 3.10:** Relative contact, given as the relative number of atoms in the sheet being within chemical interaction range, vs. strain of the sheet. The cut-off for the interaction range is  $4\text{\AA}$  corresponding to  $\sim 120\%$  the LJ equilibrium distance. No normal force is applied and temperature is kept at  $T = 300\text{ K}$ .

Compare figure Fig. 3.10 to that of figure ?? where multiple simulations constitute the stretch-contact curve.

### 3.5 Investigating default parameters

We carry out a more extensive investigation of the friction dependence on temperature  $T$ , sliding speed  $v_{\text{slide}}$ , spring constant  $K$ , and timestep  $dt$ . This is done partly to understand how the dependencies relate to the theoretical, numerical and experimental results, and partly to understand how these parameters affect the stability of our system. We use the default parameters presented in Table 3.1 and investigate the results as we change parameters, one at a time. We keep the load at  $1\text{ nN}$ . We consider the mean friction force, sampled from the last half of the simulation as described in Sec. 3.3, representing the kinetic friction. The results are shown in Fig. 3.11, where the shaded area (connected linearly) denotes the absolute error defined by the std as described in Sec. 3.3.

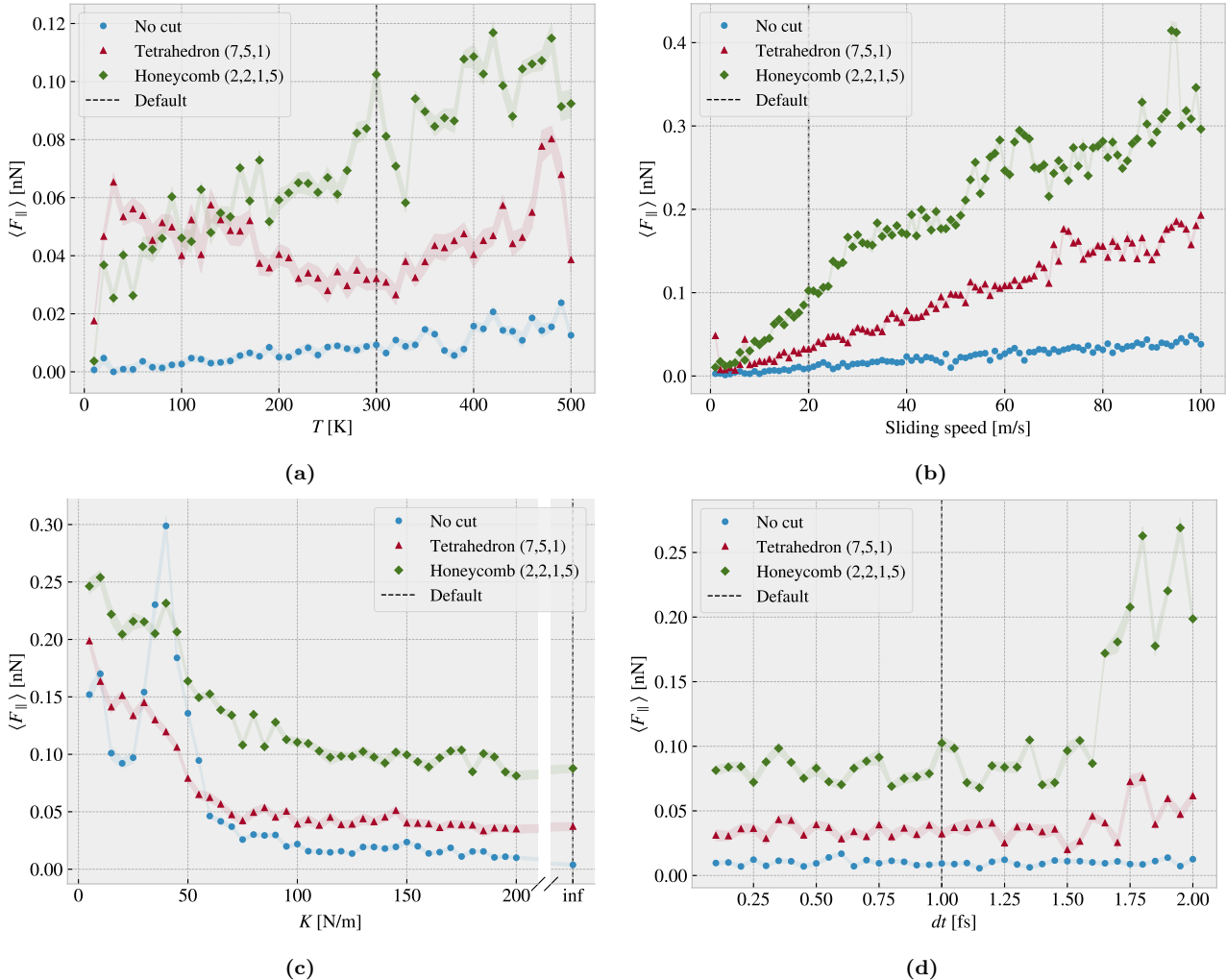


**Figure 3.11:** Main parameters investigation. Kinetic friction force

From the temperature investigation in Fig. 3.11a we find an increasing kinetic friction with temperature for both the non-cut sheet and the Honeycomb pattern. The Tetrahedron pattern shows both decreasing and increasing trends. The general trend shows a convex curve in the range (30–480 K) with a minimum around our default choice of 300 K, but with rapid fluctuations at the start (10–30 K) and end region (480–500 K). Similar fluctuations are also seen from the Honeycomb pattern, although it shows an underlying increasing trend throughout. When comparing the non-cut sheet and the Honeycomb pattern we observe that the slope for the increasing trend is high for the Honeycomb. From a theoretical and experimental point of view, we would expect a decrease in friction with temperature (see Sec. 2.5). However, an increasing trend is also observed in other MD simulation, for instance by Zhang et al. [83] sliding at 10 m/s, which is attributed to the high sliding speed associated with the ballistic motion. The default choice is initially based on the common choice of using the temperature  $T = 300$  K. The non-cut and Tetrahedron friction seems to be rather stable around that point, but we do see some significant fluctuations for the Honeycomb pattern in this range. However, we do not regard this as a critical feature.

From the sliding speed investigation in Fig. 3.11b we generally find increasing friction with velocity. Due to the relatively high velocities used and the effects from the thermostat, we expect a viscous friction  $F_k \propto v_{\text{sliding}}$  which matches rather well with these results. However, the Tetrahedron and Honeycomb sheets seem to fall slightly into a sublinear relationship as it approaches higher velocities. Furthermore, these sheets display indications of local fluctuations that could potentially be attributed to resonance effects, as discussed in relation to the phonon dynamics. Our choice of sliding speed at 20 m/s mainly reflects a consideration of computational cost, but the fact that no immediate resonance fluctuations appear in the proximity of this value supports the choice.

From the investigation of the spring constant parameter in Fig. 3.11c we observe a significant decrease in friction as the springs stiffen. This can be attributed to the transition from a stick-slip influenced regime to a smooth sliding regime as we saw for the force traces in Fig. 3.1. For soft springs the results are quite sensitive to the specific choice of spring constant which is especially seen for the non-cut sheet around  $K = 40 \text{ N/m}$ . Thus, in order to avoid this domain we settled for the infinitely stiff spring. This is also considered a more favorable option due to its ability to provide greater standardization of the simulations.

Finally, we consider the numerical stability of the result as we vary the simulation timestep in Fig. 3.11d. The general trend shows a stable plateau below  $\sim 1.5 \text{ fs}$  for which higher values show signs of arising instabilities for the cut sheets (Tetrahedron and Honeycomb). This mainly confirms that our choice of timestep is within a reasonable range. However, we do see some fluctuations which are more significant for the cut sheets.

The observed fluctuations suggest that randomness plays a role in our simulations and also indicate that the cut sheets are relatively unstable. Further investigation through varying the random seed for the initial velocity and thermostat could shed more light on this matter. In the meantime, we may consider these fluctuations as a sign that the uncertainty in our results is higher than what was estimated using the running mean and running std evaluation. For the Honeycomb sheet, these fluctuations are on the order  $\pm 0.017 \text{ nN}$ .

### 3.5.1 Computational cost

We run the simulations on a CPU cluster made available by the University of Oslo. This allows us to run multiple simulations at once and with each simulation running in parallel on multiple CPU cores as well. As we decide on the simulation parameters we must also consider the computational cost. When selecting simulation parameters, we also need to keep in mind the computational cost. Given that the chosen parameters will be applied to multiple simulations, any increase in computational time will be multiplied by the number of intended simulations, which is expected to be around 10,000. The computational cost is especially dependent on the timestep and the sliding speed as this will affect the number of computations. As an extension of the analysis in Sec. 3.5 we report on the computational times associated with temperature, sliding speed, spring constant and dt. By retrieving the computational time used for the parameter investigation in Fig. 3.11 we get the timing as shown in Fig. 3.12. Note that these timings are only based on a single simulation for each parameter as opposed to an average over multiple runs which is necessary for more reliable data.

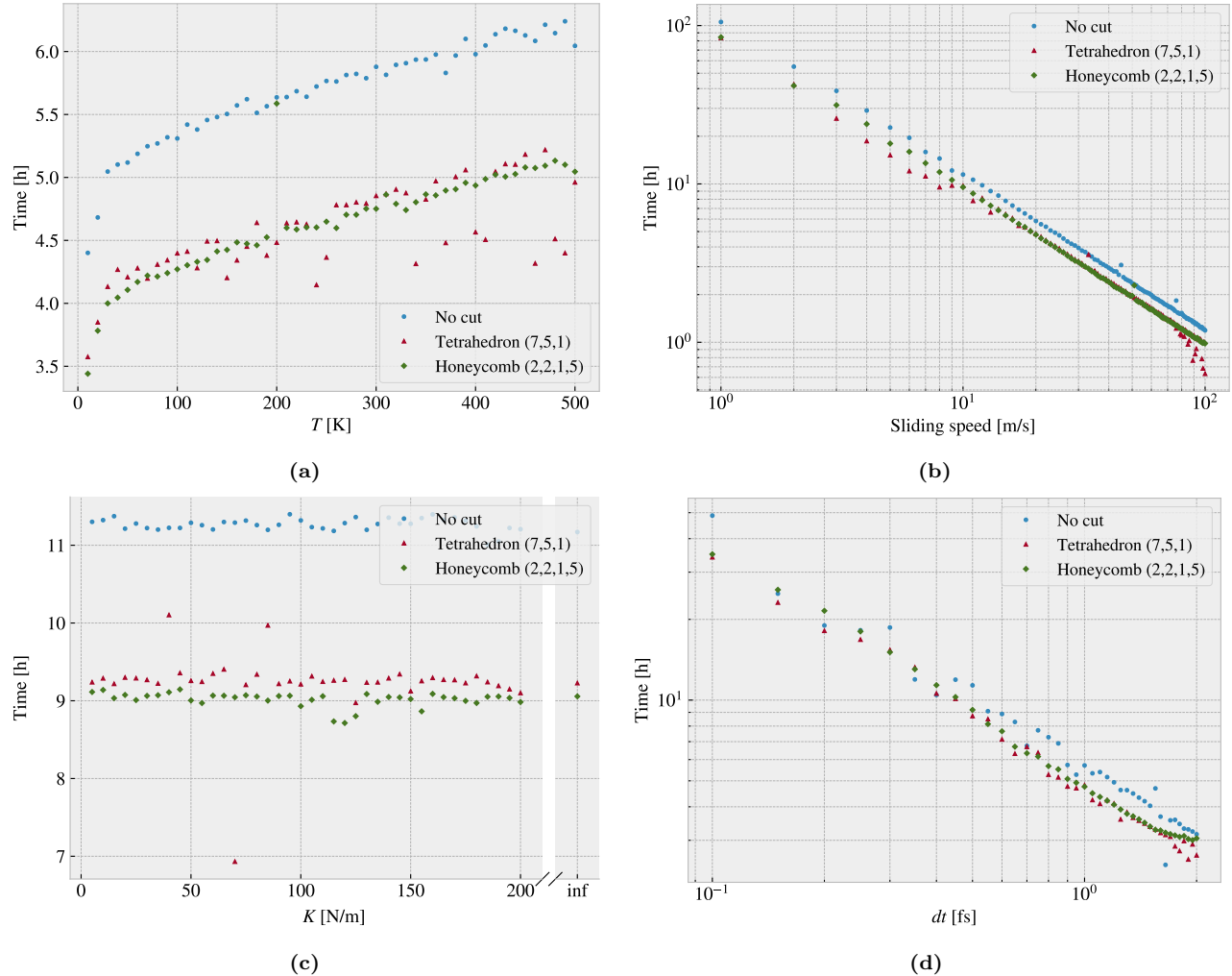


**Figure 3.12:** Computational cost related to temperature, sliding speed, spring constant and  $dt$  parameter in terms of CPU hours running on 16 cores on the cluster. Sliding speed follows  $t \propto v^{-0.977 \pm 0.005}$  and  $dt$  follows  $t \propto dt^{-0.87 \pm 0.02}$

The computational time is governed by the number of timesteps in the simulation and the time used per timestep. For a fixed sliding distance, the number of timesteps in the simulation are inversely proportional to sliding speed and similar inversely proportional to timestep  $dt$ . From the timings in Fig. 3.12 we find the sliding speed to obey this expectation rather well by  $t \propto v^{-0.977 \pm 0.005}$  while the timing did not increase as strongly with timestep, falling below the  $1/dt$  relation with  $t \propto dt^{-0.87 \pm 0.02}$ . Moreover, we find that increasing temperature also makes for an increased computation time. This can be attributed to an increase in the computation time associated with the force calculations. The rising temperature gives rise to more fluctuations in the system which might yield more atoms within the force calculation cutoffs for each computation. This kind of consideration can also be attributed to the reason for the deviating timing for  $dt$ . Finally, for the spring parameter, we did not see any noticeable effect on timing.

In general, we have selected our simulation parameters: temperature, sliding speed, spring constant, and timestep, based on numerical stability and computational cost. For the timestep, we found that a value of 1 fs, commonly used in similar studies [81, 82], produced stable results while higher values were prone to instabilities and lower values were computationally expensive. The sliding speed was chosen primarily based on computational cost, with a default value of 20 m/s being a reasonable compromise between computational efficiency and the lower values more commonly used in other studies. Although a lower sliding speed could lead to more commonly observed stick-slip motion, it represents a factor of 20 increase in computational time. Since stick-slip motion is out of reach based on the chosen sliding speed, we found that using an infinitely stiff spring  $K = \infty$  was the

most reasonable option to ensure stable results. Finally, the temperature investigation did not provide much guidance for a specific choice, so we settled for the standard choice of room temperature  $T = 300\text{ K}$ .

## 3.6 Load and stretch dependencies

So far, we have carried out a general analysis of the system behavior under the influence of various simulation parameters. This lays the foundation for the remaining study as we now shift our intention towards the friction dependence of strain and load.

### 3.6.1 Pressure reference for normal load

We consider a load range of  $0.1\text{--}10\text{ nN}$  which coincide with the general investigated range in other MD studies [76, 82]. In order to relate the magnitude of this load we provide a short calculation of the corresponding pressure. We will use the pressure underneath a stiletto-heeled shoe as a high-pressure reference from our macroscale perspective. The diameter of a stiletto-heeled shoe can be less than  $1\text{ cm}$  [93], and hence an  $80\text{ kg}$  man<sup>5</sup> standing on one stiletto heel, with all the weight on the heel, will correspond to a pressure

$$P = \frac{F}{A} = \frac{mg}{r^2\pi} = \frac{80\text{ kg} \cdot 9.8 \frac{\text{m}}{\text{s}^2}}{\left(\frac{10^{-2}\text{ m}}{2}\right)^2\pi} = 9.98 \text{ MPa.}$$

The fact that the pressure under a stiletto heel can get this high, actually greater than the pressure under an elephant foot, is an interesting realization in itself that is often used in introductory physics courses [94], but this also serves as a reasonable upper bound for human executed pressure. With a full sheet area of  $\sim 21 \times 10^3 \text{ \AA}^2$  our load range of  $0.1\text{--}10\text{ nN}$  corresponds to a pressure of  $0.47\text{--}47\text{ MPa}$  which relates nicely to our macroscale reference. This pressure might be incompatible with various industrial purposes, but with no specific application in mind, this serves as a decent reference point. Notice, that if we consider a human foot with area  $113\text{ cm}^2$  [95] the pressure drops to a mere  $70\text{ kPa}$  corresponding to only  $\sim 0.01\text{ nN}$ .

### 3.6.2 Strain dependency

We consider the effects of stretching the sheet using the non-cut, Tetrahedron (7, 5, 1) and Honeycomb (2, 2, 1, 5) sheet as used so far. For each configuration, we run a rupture test where the given sheet is stretched under zero load, but still under the influence of adhesion from the substrate. The rupture strain is then recorded, and multiple new simulations are initiated with strain values between zero and the rupture strain. For the sampling of the stretch values in the available range, we use a pseudo-uniform distribution, meaning that we divide the given interval into equal segments and pick a value from each segment by a uniform distribution. This is due to numerical limitations in LAMMPS<sup>6</sup>, but we find that this gives evenly spaced values which also carry some randomness. For the load we use  $0.1$ ,  $1$  and  $10\text{ nN}$ .

First, we aim to reproduce the contact investigation from Fig. 3.10. We quantify the relative contact as described in Sec. 3.4, but we convert this into a single metric for a given simulation by considering the average of the last 50% of data points, similar to what we have done for the mean friction. We also adopt a similar method for quantifying the error (see Sec. 3.3). The results are shown in Fig. 3.10 where we observe a significant decrease in relative contact for the kirigami patterns which qualitatively agrees with the non-loaded continuous stretch simulation in Fig. 3.10. This result implies that the change in contact is not governed by a momentum effect during stretching, as each simulation now keeps the strain constant throughout the simulation. The absolute error for the mean rel. contact was generally quite low on the order of 0.01 for all configurations.

From an asperity theory point of view, this reduction in contact is theorized to induce a similar reduction in friction. However, when considering the kinetic friction in Fig. 3.13b we find that this is not the case. For the Tetrahedron and Honeycomb patterns, we find that the friction initially increases with a decreasing contact

<sup>5</sup>Yes, a man can certainly wear stiletto heels.

<sup>6</sup>In LAMMPS, we sample the various strain values by storing restart files during the straining of the sheet. The restart values are stored at specific timesteps governed by a LAMMPS variable. Such variables allow for a vector of uniform randomly chosen values, but unfortunately, we are not able to sort the vector for ascending values. This will lead to the script waiting to store each restart file according to the timesteps in the unsorted vector. As soon as the next timestep value is less than the current timestep the program will stop producing restart files and thus skip most of them. However, by first defining a series of intervals we can draw a uniform number for each interval without getting into trouble.

area. Yet, these are not simply inversely proportional as the friction force suddenly dips down and up again, in the strain range of 0.08–0.11 for the Tetrahedron and 0.73–1.05 for the Honeycomb pattern. When considering the non-cut sheet, we find that both the contact area and friction remain seemingly unaffected by strain. This indicates that the contact area is not a dominating mechanism for friction in our system, but the underlying mechanism might make for a correlation between a decreasing contact area and the non-linear friction-strain curve observed here. The latter point can be supported by the fact that the contact-strain and friction-strain curve both show signs of a discontinuous jump around a strain of 0.32. Since the non-cut sheet exhibits a flat friction-strain profile we cannot attribute the behavior to an increased tension either. The friction effect of tension of a graphene sheet has been investigated by Zhang et al. [74]. However, they report a decreasing friction with tension which qualitatively contradicts our observation as the direction of the effect is opposite. Instead, we might point to a commensurability effect or perhaps a change in the structural stiffness which is reported as an important feature by [37]. We observe that the initial friction value of the non-strained sheet varies across configurations, with the initial friction increasing from the non-cut sheet, through the Tetrahedron sheet, to the Honeycomb sheet. This is more evident from the parameter investigation from Fig. 3.11, but the size of this effect is within a range on the order of [0.01, 0.1] nN. We notice also that the two orders of magnitude increase in normal load did not make a significant difference in the results. The estimated absolute error marked by a shaded area in Fig. 3.13b were fairly low for both friction on the order  $10^{-3}$  nN and relative contact on the order of  $10^{-4}$ .

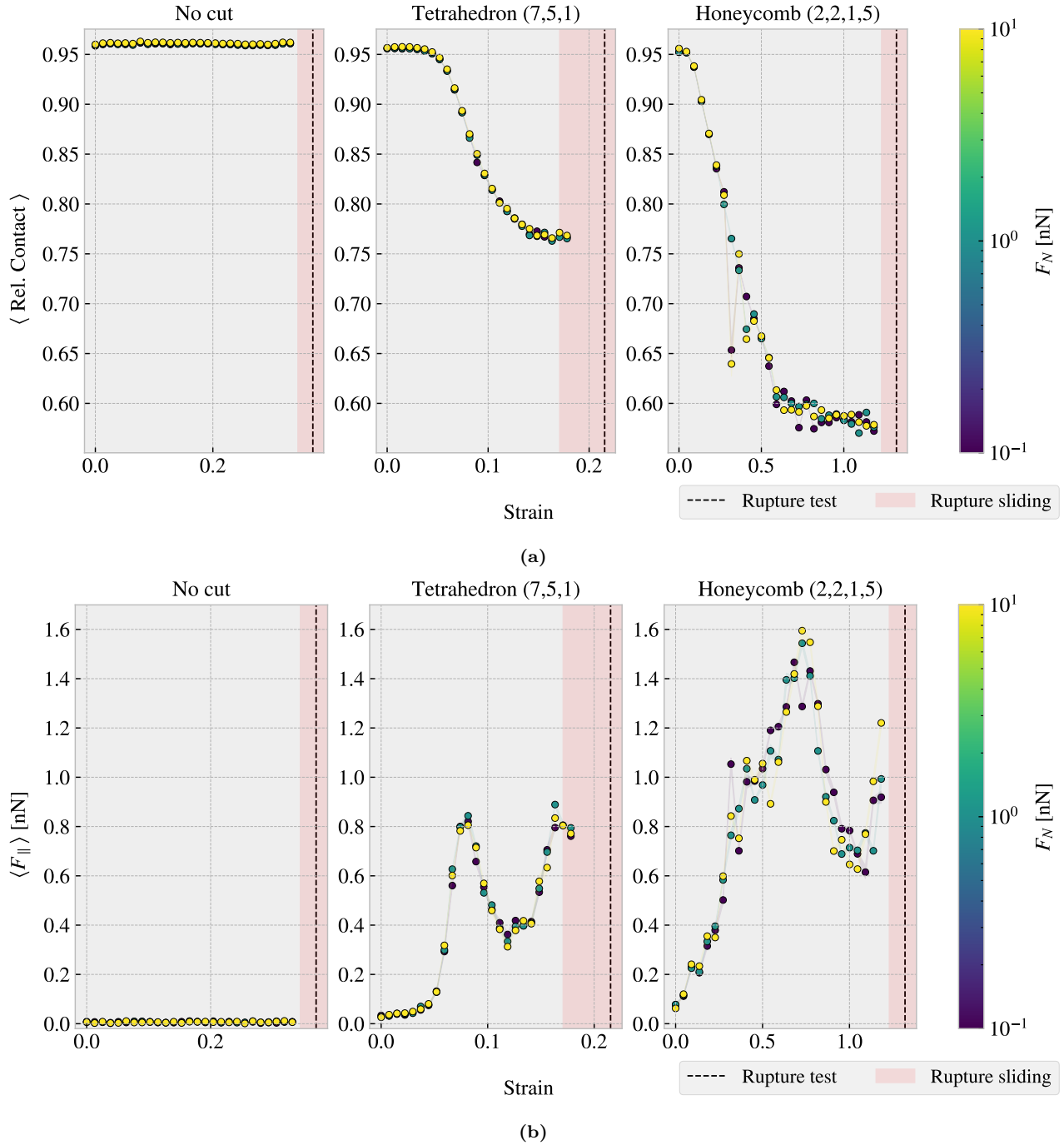


**Figure 3.13:** Average relative contact and average friction for multiple simulations, consisting of 30 stretch values sampled from a pseudo uniform distribution between 0 and the rupture point in combination with loads 0.1, 1 and 10 nN, for each of the configurations: non-cut, Tetrahedron (7,5,1) and Honeycomb (2,2,1,5). The average is taken over the last half of the sliding phase. The red shade denotes the stretch range where ruptures accoured during sliding while the black-dotted line represent the rupture point in the no load rupture test. (a) The average relative contact defined as the relative number of atoms within a contact threshold of 4 Å to the substarte. The absolute error is on the order 0.01 (b) The average mean friction force parallel to the sliding direction. The absolute error for the mean friction is on the order 0.001–0.01 nN. Mention error for contact being on the order e-4–e-5

By considering the increase in friction from zero strain towards the first peak of the friction-strain curve we find that the Tetrahedron pattern exhibits a relative friction increase of  $\sim 27.7$  while the Honeycomb pattern

exhibits a relative increase of  $\sim 22.4$ . This is in itself a remarkable result, but considering that the friction drops almost as dramatically afterward makes for an even more unexpected behavior. For the Tetrahedron sheet the friction drops by  $\sim 0.51$  nN during an increased strain  $\Delta\varepsilon \sim 0.04$  while Honeycomb drops  $\sim 0.98$  nN during a strain increase of  $\Delta\varepsilon \sim 0.36$ . These results are promising for the aim of demonstrating a negative friction coefficient for a system with coupled load and stretch. We will discuss this further at the end of this chapter in Sec. 3.6.4.

Be sure to mention the independent effect from Kirigami sheet without strain as this is mentioned in the hypothesis in the summary

### 3.6.3 Load dependency

From the investigation of the stretch dependency we saw that increasing the normal load from 0.1 to 10 nN did not make a considerable impact on the friction in comparison to the effect associated with strain. One special feature of our system is that we only apply load to the pull blocks, and thus one might suspect this to be of importance. Therefore, we investigate the friction under varying loads for a non-cut sheet comparing the case of loading the pull block against a more traditional uniform loading of the sheet as shown in Fig. 3.14. Both load distributions show a seemingly non-dependent relationship between friction and load considering the size of our estimated error. Nonetheless, we do not see any indications that the uniform loading changes the qualitative behavior.

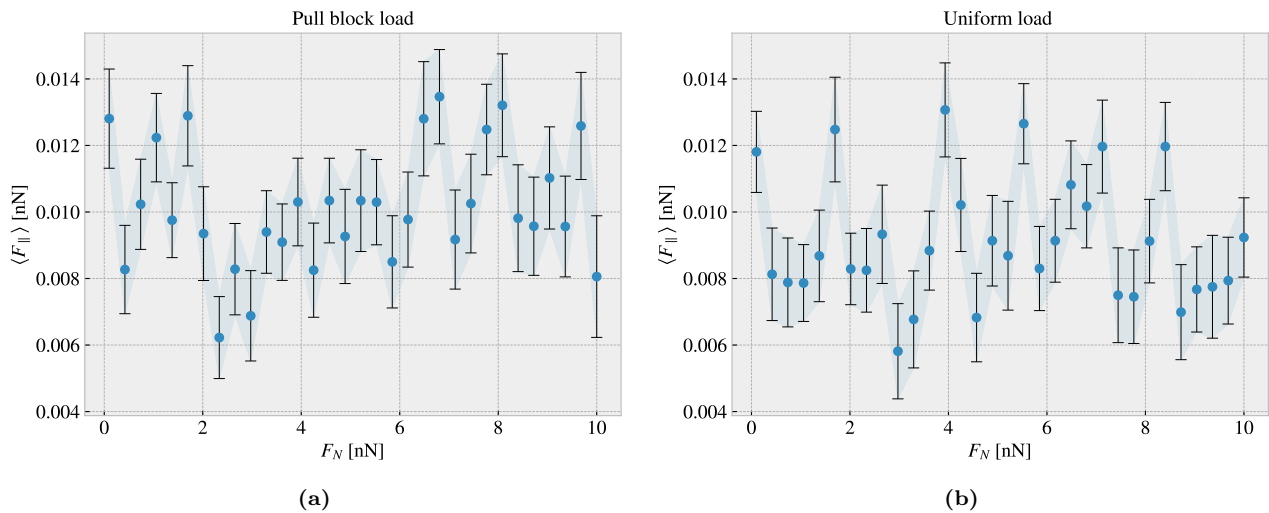


**Figure 3.14:** Multiple simulations of non-cut sheet under different load. Mean friction is plotted against load for two different variations of loading distribution. (a) Normal loading is applied to the pull blocks. (b) Normal loading is applied uniformly to the sheet.

In order to further investigate the friction dependency of normal load for the Kirigami patterns as they are stretched, we select a subset of stretch stages from Fig. 3.13b and perform additional simulations with a logarithmically increasing normal load in the extended load range 0.1–100 nN, using 30 load data points for each strain. The results are shown in Fig. 3.15. When spanning three orders of magnitude for the normal load we find some increase in friction with load. This goes for all patterns, but it is only really visible for the non-cut sheet as the values on the friction axis show a more narrow range. Notice that the load is plotted for a logarithmic axis which makes any seemingly linear trends on the figure sublinear. However, as the normal load approaches 100 nN we do start to see an increase that is more reminiscent of a linear relationship, but this is difficult to judge given that the change in friction is small in comparison to the noise in the data. Note that we omitted the error bars for visual purposes but they are on the same order of magnitude as shown in Fig. 3.14.

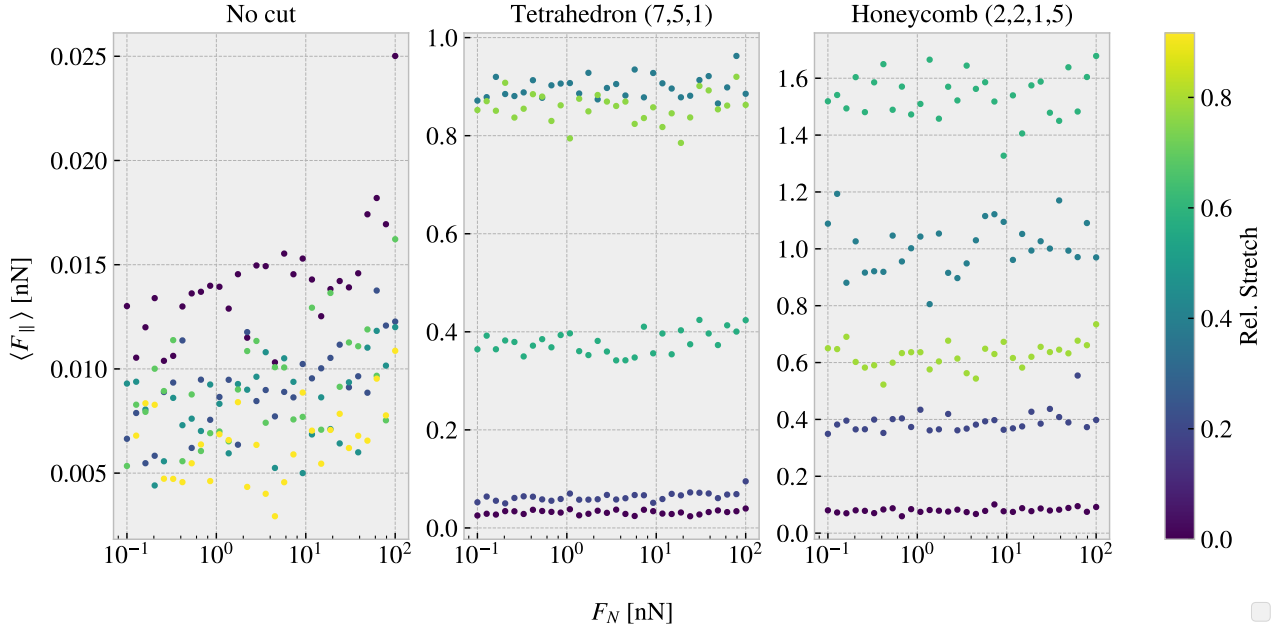


**Figure 3.15:** Mean friction force vs. load in the range 0.1–100 nN, for the non-cut, Tetrahedron (7, 5, 1) and Honeycomb (2, 2, 1, 5) sheet resepectively, at different stretch stages relative to their rupture point.

From the friction measurements in Fig. 3.15 we see that the non-cut sheet generally produces a friction force in the order of 0.005–0.0025 nN throughout the 0.1–100 nN load range. Using a ratio based friction coefficient definition Eq. (2.2a),  $\mu_1 = F_{\text{fric}}/F_N$ , this would lead to a coefficient roughly in the range

$$\mu_1, \text{ Eq. (2.2a): } \text{No cut} \sim [10^{-4}, 0.13], \quad \text{Tetrahedron} \sim [4 \times 10^{-4}, 8.7], \quad \text{Honeycomb} \sim [9 \times 10^{-4}, 15.2].$$

However, these values mainly reflect the poorness of this definition, as we find the values to diverge at low load and decrease towards high load due to the lacking linear relationship and an offset in the load curve corresponding to a finite friction at zero load. This offset is drastically enhanced for the Kirigami patterns under strain. Due to the small changes in friction compared to the noise in the data, it is not sensible to calculate the slope  $dF_{\text{fric}}/dF_N$  as a function of load. Nonetheless, if we force a linear fit for the whole range and use the second definition Eq. (2.2b) as  $\langle \mu_2 \rangle = \Delta F_{\text{fric}}/\Delta F_N$ , we get average coefficients in the range

$$\mu_2, \text{ Eq. (2.2b): } \text{No cut} \sim [4, 9] \times 10^{-5}, \quad \text{Tetrahedron} \sim 5 \times [10^{-5}, 10^{-4}], \quad \text{Honeycomb} \sim [1, 9] \times 10^{-4},$$

depending on the strain values. These numbers should be interpreted cautiously, but we can take it as a rough estimate of the friction coefficient being on the order  $10^{-4}$ – $10^{-5}$ . This relates to the finding by [64] who reported a seemingly non-existing relationship between friction and normal load with change in friction that corresponds to friction coefficients in the range  $10^{-3}$ – $10^{-4}$  when using the slope definition Eq. (2.2b). This supports the idea that the graphene sheet does in fact exhibit superlubric behavior in these conditions. Moreover, the fact that the increase with load is relatively unaffected by the stretching points to the fact that the strain-induced effect mainly shifts the load curve towards higher friction but does not significantly alter its slope.

### 3.6.4 Prospects of a negative friction coefficient

Considering the results from Sec. 3.6.2 and Sec. 3.6.3 we find that strain-induced friction effects, on the order of  $/SI1nN$ , are generally dominating in comparison to load-induced effects on the order of 0.01 nN given a load range of  $10^2$  nN. This is promising for the idea of achieving a negative friction coefficient for a nanomachine system that couples load and strain. By applying load on the nanomachine we would increase both the load and the strain on the sheet simultaneously. However, since the friction dependency to strain dominates in comparison to load effects such a system can be designed entirely by considering the strain dependency. The friction coefficient is by our definition (Eq. (2.2b)) given as the slope of the friction  $F_f$  vs. normal force  $F_N$  curve.

Hence, for two points  $\{(F_{N,1}, F_{f,1}), (F_{N,2}, F_{f,2})\}$ ,  $F_{N,1} < F_{N,2}$  we can evaluate the associated friction coefficient  $\mu_{1,2}$  as

$$\mu_{1,2} = \frac{F_{f,2} - F_{f,1}}{F_{N,2} - F_{N,1}} = \frac{\Delta F_f}{\Delta F_N}.$$

If we neglect load effects  $F_f(F_N, \varepsilon) \sim F_f(\varepsilon)$  and consider a coupling  $\varepsilon = RF_N$  with linear coupling ratio  $R$  we get

$$\mu_{1,2}(\varepsilon_1, \varepsilon_2) = \frac{\Delta F_f(\varepsilon_1, \varepsilon_2)}{\frac{1}{R}(\varepsilon_2 - \varepsilon_1)} = R \frac{\Delta F_f(\varepsilon_1, \varepsilon_2)}{\Delta \varepsilon}. \quad (3.1)$$

When considering the ratios found for the reduction in friction with strain for the Tetrahedron and Honeycomb patterns in Sec. 3.6.2 we find the corresponding coupled system friction coefficients to be

$$\text{Tetrahedron: } R \frac{-0.51 \text{ nN}}{0.04} = -R \cdot 12.75 \text{ nN}, \quad \text{Honeycomb: } R \frac{-0.98 \text{ nN}}{0.36} = -R \cdot 2.72 \text{ nN} \quad (3.2)$$

This showcases that we might be able to utilize the strain effect to achieve a negative friction for the system of coupled strain and load



# Chapter 4

## Summary

In this thesis, we have studied the nanoscale friction of a Kirigami graphene sheet under the influence of load and strain using MD simulations. We have developed a numerical framework for generating diverse Kirigami designs which we have utilized to create a dataset for the frictional behavior depending on Kirigami pattern, strain, and loading. Our findings suggest that the frictional behavior of a Kirigami sheet is highly dependent on the geometry of the pattern and the strain conditions. We observed that the out-of-plane buckling can be associated with a non-linear friction-strain curve which can be utilized to demonstrate a negative friction coefficient in a system with coupled load and strain. Moreover, we have investigated the possibility to use machine learning on this dataset and attempted an accelerated search. Our findings imply that machine learning can be feasible for this approach, additional data is required to establish a more reliable foundation for a search for new Kirigami patterns. In this chapter, we will provide a summary of our findings and draw conclusions based on the results obtained. Finally, we will suggest some topics for further research.

### 4.1 Summary and conclusions

#### 4.1.1 Designing an MD simulation

We have designed an MD simulation for the examination of friction for a graphene sheet sliding on a silicon substrate. The key system features were the introduction of the pull blocks, defined as the end regions of the sheet with respect to the sliding direction, which was utilized for applying normal load and sliding the sheet. The pull blocks were made partly rigid and used to employ a thermostat as well. Through an analysis of the friction forces retrieved from sliding simulations, we have established a standardized metric for kinetic friction. In particular, we measured the force exerted by the substrate on the full sheet, including the pull blocks, with respect to the sliding direction, and determined the kinetic friction as the mean value of the last half of the simulation. The uncertainties were estimated based on the fluctuations in the running mean. We found that the assessment of static friction was ambiguous for our simulation and did not pursue this further. From the analysis of the force traces, friction force vs. time, we identify the friction behavior in our simulation domain as being in the smooth sliding regime. This is attributed to the choice of a relatively high sliding speed (20 m/s) and infinitely stiff springs for the tethering of the sheet. This was supported by a demonstration of a transition to the stick-slip regime through the use of softer springs and a decrease in sliding speed. By conducting a more systematic investigation of the effects of temperature, sliding speed, spring constant and timestep, we identified a set of default values based on numerical stability and computational cost. During this process, we aimed to select the variables that would maintain a relatively stable measured friction with moderate perturbations around these default values. We found that friction increased with temperature which we attribute to being in the ballistic sliding regime. In the absence of clear indications from the investigation regarding an appropriate temperature, we opted for the standard choice of room temperature, 300 K. Furthermore, we found friction to increase with velocity as expected, with some signs of phonon resonance at certain sliding speeds as well. We chose a rather high velocity of 20 m/s mainly for the consideration of computational costs. For the spring constant, we found decreasing friction with increasing stiffness of the springs. This is associated with the transition from a stick-slip-influenced regime toward smooth sliding and can be attributed to an underlying change in commensurability. The choice of an infinitely stiff spring was made from an assessment of the variation

in friction with perturbations in the spring constant value. Finally, we confirmed that a timestep of 1 fs provides reasonable numerical stability. However, based on fluctuations with timestep we find that the uncertainty in the simulations might be higher than first estimated. For the non-strained Kirigami sheet, these fluctuations were on the order of  $\pm 0.017$  nN for the evaluation of the kinetic friction.

### 4.1.2 Generetig Kirigami patterns

In order to investigate the effects of Kirigami design we have created a numerical framework for generating various patterns. By defining an indexing system for the hexagonal lattice structure we were able to define the Kirigami designs as a 2D binary matrix for numerical implementation. We have selected two macroscale designs, which we denote the *Tetrahedron* and *Honeycomb* patterns, based on their ability to exhibit out-of-plane buckling when subjected to strain. By digitalizing the designs to match the hexagonal graphene lattice, we found that the characteristic design features can be translated to the nanoscale, as we observed similar out-of-plane buckling in MD simulations. Through our numerical framework we were able to create an ensemble of perturbed unique variations which yielded approximately  $135 \times 10^3$  and  $2.025 \times 10^6$  unique configurations for the Tetrahedron and Honeycomb patterns respectively. When considering the possibility to translate the periodic patterns on the graphene sheet the number of possible patterns can be increased by approximately a factor of 100. To introduce some random design features, we have developed a framework for generating Kirigami patterns based on random walks. The framework includes mechanisms such as bias, avoidance of existing cuts, preference for maintaining a direction, and procedures for repairing the sheet for simulation purposes. In general, we found that the capabilities of this numerical framework for generating Kirigami designs exceeded our computational resources with regard to performing MD simulation under different loads and strains for each of the designs. In general, we found that the computational capacity of our numerical framework for generating Kirigami designs surpassed our available resources for conducting MD simulations under various load and strain for each design. Our MD-based dataset only utilized a subset of configurations with 9660 data points based on 216 Kirigami configurations (Tetrahedron: 68, Honeycomb: 45, Random walk: 100, Pilot study: 3). Hence, we argue that the Kirigami generative framework can be valuable for further studies on an extended dataset.

### 4.1.3 Control friction using Kirigami

We have investigated the frictional behavior of the Tetrahedron and Honeycomb patterns in comparison to a non-cut sheet under various strains and loads. Initially, we observed that straining the Kirigami sheets in a vacuum resulted in an out-of-plane buckling. When adding the substrate to the simulation this translated into a decreasing contact area with strain. We found the Honeycomb sheet to exhibit the most significant buckling with a corresponding reduction of relative contact area to approximately 43%, whereas the non-cut sheet did not produce any significant buckling in comparison. For the Kirigami sheets, we found that friction initially increased with strain, which made for increasing friction with decreasing contact area. As the strain continued to increase the friction-strain curve exhibited highly non-linear trends with strong negative slopes as well (see Fig. 3.13). During the full strain, the contact area was decreasing monotonically except for a slight increase just before rupturing. These results contradict the asperity theory hypothesis of decreasing friction with decreasing contact area, and we conclude that no clear relationship between friction and contact area can be made. The non-cut sheet did not show any significant dependency on the strain as both the friction and the contact area remained constant with strain. Thus our findings suggest that a changing contact area and the strain-induced friction effects might be associated through an underlying mechanism connected to the buckling of the sheet. We did find some independent effects from the introduciton of Kirigami cuts before applying strain. We observed a small increase in friction between the non-cut sheet and the Kirigami sheet, but this was one order of magnitude lower than the effects associated with the strain in combination. Since the strained non-cut sheet did not exhibit any significant effects from strain we conclude that the independent effects from Kirigami cuts and tension in the sheet cannot be regarded as a dominating mechanism for friction. When considering the friction dependency with load, we generally found a weak dependency corresponding to a friction coefficient on the order of  $10^{-4}$ – $10^{-5}$  even though we could not confirm any clear relationship. This is best attributed to a superlubric state of the graphene sheet as seen in other studies as well. The slope of the friction-load curve was not considerably affected by the straining of the Kirigami sheet which led us to the conclusion that strain-induced effects are dominant in comparison to any load-related effects. In summary, we have found clear evidence that the friction in the Kirigami sheet system is controlled by strain.

When considering our findings in light of previous related results we find it plausible that the governing mechanism for the observed friction effects is related to commensurability. Since we have observed extremely low friction in our system, we argue that the non-deformed sheet corresponds to an incommensurable configuration. This is supported by the fact that we were not able to lower the friction from the original starting point. Additionally, this also aligns with the observation that the introduction of the non-strained Kirigami designs increased friction slightly. Since some atoms were removed from the lattice this can be hypothesized to relax the incommensurability to some degree. When the Kirigami sheet buckles during stretching, it allows for a considerable rearrangement of the atoms in contact with the substrate. Hence, it may transition in and out of commensurable configurations, which could explain the non-linear trend for the friction-strain curve. One way to test this hypothesis is to reorientate the sheet in order to reach a commensurable start configuration. Then we might find a transition from a commensurable to an incommensurable case during the initial straining which would result in a lowering in friction with respect to the starting point.

#### 4.1.4 Capturing trends in friction data with machine learning

By utilizing the numerical framework for generating Kirigami design we have created a MD-based dataset for the frictional behavior depending on Kirigami designs, load and strain. The dataset reveals some general correlations with mean friction, such as a positive correlation to strain (0.77) and porosity (0.60), and a negative correlation to contact area (-0.67). These results align with the finding in the pilot study, suggesting that the change in friction is associated with cuts in the sheet (porosity) and a changing contact area.

By defining the friction property metrics:  $\min F_{\text{fric}}$ ,  $\max F_{\text{fric}}$ ,  $\max \Delta F_{\text{fric}}$  and  $\max \text{drop}$  (maximum decrease in friction with strain), we investigated the top design candidates within our dataset. From these results, we found no indication for the possibility to reduce friction with the Kirigami approach since the non-cut sheet provided the lowest overall friction. Furthermore, among the top candidates, we found that a flat friction-strain profile is mainly associated with little decrease in the contact area and vice versa. These observations are consistent with the results of the pilot study and support the hypothesis that commensurability plays a key role in governing the behavior of the system. In terms of the maximum properties, we observed an improvement compared to the values obtained in the pilot study, with the Honeycomb pattern exhibiting the highest scores. This indicates that the data may be useful for optimizing these properties.

For the machine learning investigation, we have implemented a VGGNet-16-inspired convolutional neural network with a deep “stairlike” architecture: C32-C64-C128-C256-C512-C1024-D1024-D512-D256-D128-D64-D32, for convolutional layers  $C$  with the number denoting channels and fully connected (dense) layers  $D$  with the number denoting nodes. The final model contains  $1.3 \times 10^7$  parameters and was trained using the ADAM optimizer for a cyclic learning rate and momentum scheme. We trained the network for a total 1000 epochs while saving the best model during training based on the validation score. The model validation performance gives a mean friction  $R^2$  score of  $\sim 98\%$  and a rupture accuracy of  $\sim 96\%$ . However, we got lower scores for a selected subset of the Tetrahedon ( $R^2 \sim 88.7\%$ ) and Honeycomb ( $R^2 \sim 96.6\%$ ) pattern based on the top 10 max drop scores respectively. The scores obtained were lower, even though the selected configurations were partly included in the training data and the hyperparameter selection favored the performance on this selected set. Thus we conclude that these selected configurations, associated with a highly non-linear friction-strain curve, represent a bigger challenge for the machine learning prediction. One interpretation is that these involve the most complex dynamics and perhaps that this is not readily distinguished from the behavior of the other configurations which constitute the majority of the data set. By evaluating the ability of the model to rank the dataset based on property scores, we found that it was able to effectively represent the top three scores for the maximum categories. However, the ranking for the minimum friction property was lacking. We attribute this discrepancy to the fact that this property requires a higher level of precision, which the model was not able to achieve. To obtain a more accurate evaluation of the model’s performance, we generated a test set using MD simulations for the random walk based suggestions obtained from the accelerated search. The results showed a significantly worse performance compared to the validation set, with a two-order of magnitude higher loss and a negative  $R^2$  score for the mean friction property. The negative  $R^2$  score suggests that the model’s predictions were worse than simply predicting the mean value of the true data.

However, by reevaluating the hypertuning and choosing solely on the basis of validation loss, we still found poor results on the test set. This suggests that the inadequate performance is not solely due to biased hypertuning but rather because our original dataset did not sufficiently cover a diverse range of Kirigami configurations to accurately capture the full complexity of its frictional behavior. The validation scores indicate that the use of

machine learning is a feasible approach for addressing this problem, as we were able to identify some general trends in the data. Nonetheless, from the test scores, it is evident that further improvements to the dataset are necessary in order to develop a reliable model.

#### 4.1.5 Accelerated search

Using the ML model we performed two types of accelerated search. One by evaluating the property scores of an extended dataset and another with the use of the genetic algorithm approach. For the extended dataset search, we used the developed pattern generators to generate  $1.35 \times 10^6$  Tetrahedron,  $2.025 \times 10^7$  Honeycomb and 10 k Random walk patterns. The search results for the minimum friction property indicate a preference for low cut density or low porosity. This aligns with the overall observation that the dataset does not provide any suggestions to further reduction in friction, as the non-cut sheet has the lowest friction.

The search for the maximum properties resulted in some minor score increases but the suggested candidates were mainly overlapping with the original dataset. By investigating the sensitivity to translations of the Tetrahedron and Honeycomb patterns, we observed significant variations in the model's predictions with only minor translations. This can be attributed to a physical dependency since these translations affect the edge of the sheet. However, given the poor model performance on the test set, we believe it is more likely that this variation is due to an insufficiency in the model caused by the limitations of the dataset.

In our investigation of the genetic algorithm approach, we used a starting population that was based on the results from the extended dataset accelerated search, as well as some randomly generated initializations with different porosity values. However, this approach did not provide any noteworthy indication for new design structures worth more investigation. In general, the initialization of the population itself proved to be a more promising strategy than the genetic algorithm. We acknowledge that further effort could potentially yield useful results with the genetic algorithm approach. However, we believe that the current lack of promising results can be attributed to the uncertainty of the model which where the reason for not pursuing this any further.

By considering the Grad-CAM explanation method, we observed that the model predictions were often substantially reliant on the top and bottom edges of the Kirigami configurations. This was unexpected since these edges are not true edges but are connected to the pull blocks used in the simulation. Despite the model's uncertain predictions, we speculate that this may be due to the thermostat effects from the pull blocks. Therefore, we note this as a feature worth investigating in the simulations.

#### 4.1.6 Negative friction coefficient

Based on our initial investigations of the Kirigami sheet, we have discovered a highly non-linear friction-strain relationship. By proposing a linear coupling between load and strain with ratio  $R$ , we find that these results suggest the possibility to utilize the negative slope on the friction-strain curve to achieve a negative friction coefficient. Based on the drop from top to bottom of these curves, using the Tetrahedron (7, 5, 1) and Honeycomb (2, 2, 1, 5) pattern from the pilot study, we estimate that the average coefficient within this range will be  $-R12.75 \text{ nN}$  for the Tetrahedron pattern and  $-R \cdot 2.72 \text{ nN}$  for the Honeycomb pattern.

To investigate this hypothesis, we conducted a simulation with a coupling between load and sheet tension, mimicking a nanomachine attached to the sheet, using the Kirigami configurations from the Pilot study. We observed that the non-linear behavior in the friction-strain curve also translated into a non-linear friction-load relationship for the coupled system. Additionally, we found that the Honeycomb pattern exhibited a non-linear strain-tension curve which resulted in an almost discontinuous increase in friction for the initial increase in load. We attribute this feature to an unfolding process visually confirmed from the simulation frames. For the coupled system with a load-to-tension ratio of 6 we found regions in the friction-load curve with significant negative slopes. By considering the maximum and minimum points for such regions we estimated the average friction coefficient to be  $-0.31$  in the load range  $F_N = [4.65, 6.55] \text{ nN}$  for the Tetrahedron pattern and  $-0.38$  in the range  $F_N = [0.71, 4.31] \text{ nN}$  for the Honeycomb pattern. These results can be scaled by adjusting the load-to-tension ratio.

Based on our investigations, we have found that the combination of Kirigami cuts and strain has significant potential for controlling friction. Specifically, we have demonstrated that by enforcing a coupling between load and strain through tension, it is possible to achieve a negative friction coefficient. Therefore, we believe that this approach could be promising for developing novel friction-control strategies.

## 4.2 Outlook

In this thesis, we have successfully shown that certain Kirigami designs exhibit non-linear behavior with strain. This discovery was done through a focus on the exploration of the effects of different designs. This invites further investigation of the underlying mechanisms behind this phenomenon. By considering one or two design, based on Tetrahedron and Honeycomb patterns, it would be valuable to investigate the effects on the friction-strain curve under various physical parameters.

First of all, we suggest an investigation of how the friction-strain curve depends on temperature, sliding speed, spring constant, and loads for an increased range  $F_N > 100nN$ . This is especially interesting in the context of physical conditions leading to a stick-slip behavior since our study takes a basis in smooth sliding friction. Moreover, it would be valuable to verify that the choices for relaxation time, pauses, interatomic potentials and substrate material are not critical for the qualitative observations. Especially the Adaptive Intermolecular Reactive Empirical Bond Order (AIREBO) potential for the modeling of the graphene sheet might be of interest. In this context, it might also be useful to investigate the effects of excluding adhesion in the simulations. In order to gain further insight into the role of commensurability one could vary the scan angle as well. Since we suspect that our simulation corresponds to a incommensurable superlubric state, certain scan angles are hypothesized to yield higher friction. If the friction-strain curve is based on a commensurability effect this might yield qualitative different results and perhaps also allowing for a lowering of friction with strain. We might also consider investigating the friction-strain relationship under a uniform load to get insight into how the loading distribution effects the out-of-plane buckling and associated frictional effects.

Another topic worth studying is the relation to scale and edge effects. This includes an investigation of scaling effects, considering the ratio of the sheet to the edge, but also a translation of the sheet patterns to study the presence of any Kirigami-induced edge effects. The latter is motivated by the findings from the machine learning predictions. With this regard, we would also suggest a more detailed study of the effect of the thermostat in the pull blocks which is suggested to have a possibly importance when judging from the Grad-CAM analysis.

For the machine learning approach, our findings suggest that the dataset is extended considerably. This can be done with respect to the aim of exploring Kirigami configurations as done in this thesis, but it can also be done for a single configuration under variation of some of the simulation parameters to support some of the above mentioned investigations. In that context, one could consider more advanced model architectures and machine learning techniques. If successful this would invite further studies of inverse design methods such as GAN or diffusion models.



# Appendices



## **Appendix A**

## **Appendix A**



## **Appendix A**

## **Appendix B**



## **Appendix B**

## **Appendix C**



# Bibliography

- <sup>1</sup>E. Gnecco and E. Meyer, *Elements of friction theory and nanotribology* (Cambridge University Press, 2015).
- <sup>2</sup>Bhusnur, “Introduction”, in *Introduction to tribology* (John Wiley & Sons, Ltd, 2013) Chap. 1, 1–?
- <sup>3</sup>H.-J. Kim and D.-E. Kim, “Nano-scale friction: a review”, *International Journal of Precision Engineering and Manufacturing* **10**, 141–151 (2009).
- <sup>4</sup>K. Holmberg and A. Erdemir, “Influence of tribology on global energy consumption, costs and emissions”, *Friction* **5**, 263–284 (2017).
- <sup>5</sup>B. Bhushan, “Gecko feet: natural hairy attachment systems for smart adhesion – mechanism, modeling and development of bio-inspired materials”, in *Nanotribology and nanomechanics: an introduction* (Springer Berlin Heidelberg, Berlin, Heidelberg, 2008), pp. 1073–1134.
- <sup>6</sup>P. Z. Hanakata, E. D. Cubuk, D. K. Campbell, and H. S. Park, “Accelerated search and design of stretchable graphene kirigami using machine learning”, *Phys. Rev. Lett.* **121**, 255304 (2018).
- <sup>7</sup>P. Z. Hanakata, E. D. Cubuk, D. K. Campbell, and H. S. Park, “Forward and inverse design of kirigami via supervised autoencoder”, *Phys. Rev. Res.* **2**, 042006 (2020).
- <sup>8</sup>L.-K. Wan, Y.-X. Xue, J.-W. Jiang, and H. S. Park, “Machine learning accelerated search of the strongest graphene/h-bn interface with designed fracture properties”, *Journal of Applied Physics* **133**, 024302 (2023).
- <sup>9</sup>Y. Mao, Q. He, and X. Zhao, “Designing complex architectured materials with generative adversarial networks”, *Science Advances* **6**, eaaz4169 (2020).
- <sup>10</sup>Z. Yang, C.-H. Yu, and M. J. Buehler, “Deep learning model to predict complex stress and strain fields in hierarchical composites”, *Science Advances* **7**, eabd7416 (2021).
- <sup>11</sup>A. E. Forte, P. Z. Hanakata, L. Jin, E. Zari, A. Zareei, M. C. Fernandes, L. Sumner, J. Alvarez, and K. Bertoldi, “Inverse design of inflatable soft membranes through machine learning”, *Advanced Functional Materials* **32**, 2111610 (2022).
- <sup>12</sup>S. Chen, J. Chen, X. Zhang, Z.-Y. Li, and J. Li, “Kirigami/origami: unfolding the new regime of advanced 3D microfabrication/nanofabrication with “folding””, *Light: Science & Applications* **9**, 75 (2020).
- <sup>13</sup>OpenAI, *Dall-e2*, 2023.
- <sup>14</sup>Midjourney, *Midjourney*, 2023.
- <sup>15</sup>Z. Deng, A. Smolyanitsky, Q. Li, X.-Q. Feng, and R. J. Cannara, “Adhesion-dependent negative friction coefficient on chemically modified graphite at the nanoscale”, *Nature Materials* **11**, 1032–1037 (2012).
- <sup>16</sup>B. Liu, J. Wang, S. Zhao, C. Qu, Y. Liu, L. Ma, Z. Zhang, K. Liu, Q. Zheng, and M. Ma, “Negative friction coefficient in microscale graphite/mica layered heterojunctions”, *Science Advances* **6**, eaaz6787 (2020).
- <sup>17</sup>D. Mandelli, W. Ouyang, O. Hod, and M. Urbakh, “Negative friction coefficients in superlubric graphite–hexagonal boron nitride heterojunctions”, *Phys. Rev. Lett.* **122**, 076102 (2019).
- <sup>18</sup>R. W. Liefferink, B. Weber, C. Coulais, and D. Bonn, “Geometric control of sliding friction”, *Extreme Mechanics Letters* **49**, 101475 (2021).
- <sup>19</sup>M. Metzsch, *Tuning Frictional Properties of Kirigami Altered Graphene Sheets using Molecular Dynamics and Machine Learning*.

- <sup>20</sup>A. P. Thompson, H. M. Aktulga, R. Berger, D. S. Bolintineanu, W. M. Brown, P. S. Crozier, P. J. in 't Veld, A. Kohlmeyer, S. G. Moore, T. D. Nguyen, R. Shan, M. J. Stevens, J. Tranchida, C. Trott, and S. J. Plimpton, "LAMMPS - a flexible simulation tool for particle-based materials modeling at the atomic, meso, and continuum scales", *Comp. Phys. Comm.* **271**, 108171 (2022).
- <sup>21</sup>E. M. Nordhagen, *LAMMPS simulator*.
- <sup>22</sup>A. H. Larsen, J. J. Mortensen, J. Blomqvist, I. E. Castelli, R. Christensen, M. Dułak, J. Friis, M. N. Groves, B. Hammer, C. Hargus, E. D. Hermes, P. C. Jennings, P. B. Jensen, J. Kermode, J. R. Kitchin, E. L. Kolsbjergr, J. Kubal, K. Kaasbjergr, S. Lysgaard, J. B. Maronsson, T. Maxson, T. Olsen, L. Pastewka, A. Peterson, C. Rostgaard, J. Schiøtz, O. Schütt, M. Strange, K. S. Thygesen, T. Vegge, L. Vilhelmsen, M. Walter, Z. Zeng, and K. W. Jacobsen, "The atomic simulation environment—a python library for working with atoms", *Journal of Physics: Condensed Matter* **29**, 273002 (2017).
- <sup>23</sup>A. Paszke, S. Gross, F. Massa, A. Lerer, J. Bradbury, G. Chanan, T. Killeen, Z. Lin, N. Gimelshein, L. Antiga, A. Desmaison, A. Kopf, E. Yang, Z. DeVito, M. Raison, A. Tejani, S. Chilamkurthy, B. Steiner, L. Fang, J. Bai, and S. Chintala, "Pytorch: an imperative style, high-performance deep learning library", in *Advances in neural information processing systems 32* (Curran Associates, Inc., 2019), pp. 8024–8035.
- <sup>24</sup>N Manini, O. M. Braun, E Tosatti, R Guerra, and A Vanossi, "Friction and nonlinear dynamics", *Journal of Physics: Condensed Matter* **28**, 293001 (2016).
- <sup>25</sup>B. Bhushan and A. V. Kulkarni, "Effect of normal load on microscale friction measurements", *Thin Solid Films* **278**, 49–56 (1996).
- <sup>26</sup>B. P. Hung, P. Y. Huri, J. P. Temple, A. Dorafshar, and W. L. Grayson, "Chapter 10 - craniofacial bone", in *3d bioprinting and nanotechnology in tissue engineering and regenerative medicine*, edited by L. G. Zhang, J. P. Fisher, and K. W. Leong (Academic Press, 2015), pp. 215–230.
- <sup>27</sup>J. Gao, W. D. Luedtke, D. Gourdon, M. Ruths, J. N. Israelachvili, and U. Landman, "Frictional forces and amontons' law: from the molecular to the macroscopic scale", *The Journal of Physical Chemistry B* **108**, Publisher: American Chemical Society, 3410–3425 (2004).
- <sup>28</sup>J. H. Dieterich, "Time-dependent friction in rocks", *Journal of Geophysical Research (1896-1977)* **77**, 3690–3697 (1972).
- <sup>29</sup>R. Burridge and L. Knopoff, "Model and theoretical seismicity", *Bulletin of the Seismological Society of America* **57**, 341–371 (1967).
- <sup>30</sup>O. M. Braun and J. Röder, "Transition from stick-slip to smooth sliding: an earthquakelike model", *Phys. Rev. Lett.* **88**, 096102 (2002).
- <sup>31</sup>W. I. Newman and A. M. Gabrielov, "Failure of hierarchical distributions of fibre bundles. I", *International Journal of Fracture* **50**, 1–14 (1991).
- <sup>32</sup>R. F. Smalley Jr., D. L. Turcotte, and S. A. Solla, "A renormalization group approach to the stick-slip behavior of faults", *Journal of Geophysical Research: Solid Earth* **90**, 1894–1900 (1985).
- <sup>33</sup>P. Selvadurai, P. Galvez, P. Mai, and S. Glaser, "Modeling frictional precursory phenomena using a wear-based rate- and state-dependent friction model in the laboratory", *Tectonophysics* **847**, 229689 (2023).
- <sup>34</sup>Y. Mo, K. T. Turner, and I. Szlufarska, "Friction laws at the nanoscale", *Nature* **457**, 1116–1119 (2009).
- <sup>35</sup>G. Carbone and F. Bottiglione, "Asperity contact theories: do they predict linearity between contact area and load?", *Journal of the Mechanics and Physics of Solids* **56**, 2555–2572 (2008).
- <sup>36</sup>F. Bowden and D. Tabor, *The friction and lubrication of solids*, International series of monographs on physics vb. 1 (Clarendon Press, 2001).
- <sup>37</sup>H.-J. Kim and D.-E. Kim, "Molecular dynamics simulation of atomic-scale frictional behavior of corrugated nano-structured surfaces", *Nanoscale* **4**, 3937–3944 (2012).
- <sup>38</sup>W. Commons, *File:asperities.svg — wikimedia commons, the free media repository*, [Online; accessed 3-February-2023], 2023.
- <sup>39</sup>I. Szlufarska, M. Chandross, and R. W. Carpick, "Recent advances in single-asperity nanotribology", *Journal of Physics D: Applied Physics* **41**, 123001 (2008).
- <sup>40</sup>G. Binnig, C. F. Quate, and C. Gerber, "Atomic force microscope", *Phys. Rev. Lett.* **56**, 930–933 (1986).

- <sup>41</sup>S. S. Perry, “Scanning Probe Microscopy Measurements of Friction”, *MRS Bulletin* **29**, 478–483 (2004).
- <sup>42</sup>Hertz, “On the contact of elastic solids”, *Crelle's Journal* **92**, 156–171.
- <sup>43</sup>D. Maugis, “Adhesion of spheres: the jkr-dmt transition using a dugdale model”, *Journal of Colloid and Interface Science* **150**, 243–269 (1992).
- <sup>44</sup>M. H. Müser, “Rigorous field-theoretical approach to the contact mechanics of rough elastic solids”, *Phys. Rev. Lett.* **100**, 055504 (2008).
- <sup>45</sup>B. N. J. Persson, “Theory of rubber friction and contact mechanics”, *The Journal of Chemical Physics* **115**, 3840–3861 (2001).
- <sup>46</sup>J. A. Greenwood and J. B. P. Williamson, *Contact of nominally flat surfaces*, en, 1966.
- <sup>47</sup>A. Bush, R. Gibson, and T. Thomas, “The elastic contact of a rough surface”, *Wear* **35**, 87–111 (1975).
- <sup>48</sup>B. Luan and M. O. Robbins, “The breakdown of continuum models for mechanical contacts”, *Nature* **435**, 929–932 (2005).
- <sup>49</sup>Y. Dong, A. Vadakkepatt, and A. Martini, “Analytical models for atomic friction”, *Tribology Letters* **44**, 10.1007/s11249-011-9850-2 (2011).
- <sup>50</sup>E. Gnecco, R. Bennewitz, T. Gyalog, C. Loppacher, M. Bammerlin, E. Meyer, and H.-J. Güntherodt, “Velocity dependence of atomic friction”, *Phys. Rev. Lett.* **84**, 1172–1175 (2000).
- <sup>51</sup>P. Hänggi, P. Talkner, and M. Borkovec, “Reaction-rate theory: fifty years after kramers”, *Rev. Mod. Phys.* **62**, 251–341 (1990).
- <sup>52</sup>Y. Sang, M. Dubé, and M. Grant, “Thermal effects on atomic friction”, *Phys. Rev. Lett.* **87**, 174301 (2001).
- <sup>53</sup>S. Y. Krylov, K. B. Jinesh, H. Valk, M. Dienwiebel, and J. W. M. Frenken, “Thermally induced suppression of friction at the atomic scale”, *Phys. Rev. E* **71**, 065101 (2005).
- <sup>54</sup>S. Krylov and J. Frenken, “Thermal contact delocalization in atomic scale friction: a multitude of friction regimes”, English, *New Journal of Physics* **9**, 10.1088/1367-2630/9/10/398 (2007).
- <sup>55</sup>K. B. Jinesh, S. Y. Krylov, H. Valk, M. Dienwiebel, and J. W. M. Frenken, “Thermolubricity in atomic-scale friction”, *Phys. Rev. B* **78**, 155440 (2008).
- <sup>56</sup>M. H. Müser, “Nature of mechanical instabilities and their effect on kinetic friction”, *Phys. Rev. Lett.* **89**, 224301 (2002).
- <sup>57</sup>Q. Li, Y. Dong, D. Perez, A. Martini, and R. W. Carpick, “Speed dependence of atomic stick-slip friction in optimally matched experiments and molecular dynamics simulations”, *Phys. Rev. Lett.* **106**, 126101 (2011).
- <sup>58</sup>Y. Dong, Q. Li, and A. Martini, “Molecular dynamics simulation of atomic friction: a review and guide”, *Journal of Vacuum Science & Technology A* **31**, 030801 (2013).
- <sup>59</sup>K. Johnson and J. Woodhouse, “Stick-slip motion in the atomic force microscope”, *Tribology Letters* **5**, 155–160 (1998).
- <sup>60</sup>S. N. Medyanik, W. K. Liu, I.-H. Sung, and R. W. Carpick, “Predictions and observations of multiple slip modes in atomic-scale friction”, *Phys. Rev. Lett.* **97**, 136106 (2006).
- <sup>61</sup>A. Vanossi, N. Manini, M. Urbakh, S. Zapperi, and E. Tosatti, “Modeling friction: from nanoscale to mesoscale”, *Reviews of Modern Physics* **85**, 529–552 (2013).
- <sup>62</sup>J. Frenkel and T. Kontorova, “On the theory of plastic deformation and twinning”, *Phys. Z. Soviet.* **13** (1938).
- <sup>63</sup>J. Norell, A. Fasolino, and A. Wijn, “Emergent friction in two-dimensional frenkel-kontorova models”, *Physical Review E* **94**, 10.1103/PhysRevE.94.023001 (2016).
- <sup>64</sup>M. Dienwiebel, N. Pradeep, G. S. Verhoeven, H. W. Zandbergen, and J. W. Frenken, “Model experiments of superlubricity of graphite”, *Surface Science* **576**, 197–211 (2005).
- <sup>65</sup>C. Kittel, *Introduction to solid state physics*, 8th ed. (Wiley, 2004).
- <sup>66</sup>J. A. van den Ende, A. S. de Wijn, and A. Fasolino, “The effect of temperature and velocity on superlubricity”, *Journal of Physics: Condensed Matter* **24**, 445009 (2012).
- <sup>67</sup>X.-H. Zhang, U. Tartaglino, G. E. Santoro, and E. Tosatti, “Velocity plateaus and jumps in carbon nanotube sliding”, *Surface Science* **601**, 3693–3696 (2007).

- <sup>68</sup>X. H. Zhang, G. E. Santoro, U. Tartaglino, and E. Tosatti, “Dynamical chiral symmetry breaking in sliding nanotubes”, *Phys. Rev. Lett.* **102**, 125502 (2009).
- <sup>69</sup>M. Weiss and F.-J. Elmer, “Dry friction in the Frenkel-Kontorova-Tomlinson model: dynamical properties”, *Zeitschrift für Physik B Condensed Matter* **104**, 55–69 (1997).
- <sup>70</sup>B. Bhushan, “Nanotribology and nanomechanics”, *Wear* **259**, 15th International Conference on Wear of Materials, 1–? (2005).
- <sup>71</sup>O. Penkov, H.-J. Kim, H.-J. Kim, and D.-E. Kim, “Tribology of graphene: A review”, *International Journal of Precision Engineering and Manufacturing* **15**, 577–585 (2014).
- <sup>72</sup>X. Zhao, M. Hamilton, W. G. Sawyer, and S. S. Perry, “Thermally activated friction”, *Tribology Letters* **27**, 113–117 (2007).
- <sup>73</sup>G Paolicelli, M Tripathi, V Corradini, A Candini, and S Valeri, “Nanoscale frictional behavior of graphene on sio<sub>2</sub> and ni(111) substrates”, *Nanotechnology* **26**, 055703 (2015).
- <sup>74</sup>S. Zhang, Y. Hou, S. Li, L. Liu, Z. Zhang, X.-Q. Feng, and Q. Li, “Tuning friction to a superlubric state via in-plane straining”, *Proceedings of the National Academy of Sciences* **116**, Publisher: Proceedings of the National Academy of Sciences, 24452–24456 (2019).
- <sup>75</sup>H. M. Yoon, Y. Jung, S. C. Jun, S. Kondaraju, and J. S. Lee, “Molecular dynamics simulations of nanoscale and sub-nanoscale friction behavior between graphene and a silicon tip: analysis of tip apex motion.”, *Nanoscale* **7** **14**, 6295–303 (2015).
- <sup>76</sup>S. Li, Q. Li, R. W. Carpick, P. Gumbsch, X. Z. Liu, X. Ding, J. Sun, and J. Li, “The evolving quality of frictional contact with graphene”, *Nature* **539**, Number: 7630, 541–545 (2016).
- <sup>77</sup>A. Wijn, A. Fasolino, A. Filippov, and M. Urbakh, “Low friction and rotational dynamics of crystalline flakes in solid lubrication”, *Europhysics Letters (epl)* **95**, 10.1209/0295-5075/95/66002 (2011).
- <sup>78</sup>X. Feng, S. Kwon, J. Y. Park, and M. Salmeron, “Superlubric sliding of graphene nanoflakes on graphene”, *ACS Nano* **7**, Publisher: American Chemical Society, 1718–1724 (2013).
- <sup>79</sup>F. Bonelli, N. Manini, E. Cadelano, and L. Colombo, “Atomistic simulations of the sliding friction of graphene flakes”, *The European Physical Journal B* **70**, 449–459 (2009).
- <sup>80</sup>M. Reguzzoni, A. Fasolino, E. Molinari, and M. C. Righi, “Friction by shear deformations in multilayer graphene”, *The Journal of Physical Chemistry C* **116**, 21104–21108 (2012).
- <sup>81</sup>Y. Liu, F. Grey, and Q. Zheng, “The high-speed sliding friction of graphene and novel routes to persistent superlubricity”, *Scientific Reports* **4**, 4875 (2014).
- <sup>82</sup>P. Zhu and R. Li, “Study of nanoscale friction behaviors of graphene on gold substrates using molecular dynamics”, *Nanoscale Research Letters* **13**, 34 (2018).
- <sup>83</sup>J. Zhang, E. Osloub, F. Siddiqui, W. Zhang, T. Ragab, and C. Basaran, “Anisotropy of graphene nanoflake–diamond interface frictional properties”, *Materials* **12**, 10.3390/ma12091425 (2019).
- <sup>84</sup>L. Colombo, “Tight-binding molecular dynamics: A primer”, *La Rivista del Nuovo Cimento* **28**, 1–59 (2005).
- <sup>85</sup>A. Sircar and P. K. Patra, “A simple generalization of Prandtl–Tomlinson model to study nanoscale rolling friction”, *Journal of Applied Physics* **127**, 135102, 10.1063/1.5143062 (2020).
- <sup>86</sup>M. Reguzzoni and M. C. Righi, “Size dependence of static friction between solid clusters and substrates”, *Phys. Rev. B* **85**, 201412 (2012).
- <sup>87</sup>N. Varini, A. Vanossi, R. Guerra, D. Mandelli, R. Capozza, and E. Tosatti, “Static friction scaling of physisorbed islands: the key is in the edge”, *Nanoscale* **7**, 2093–2101 (2015).
- <sup>88</sup>T. Fileteer, J. L. McChesney, A. Bostwick, E. Rotenberg, K. V. Emtsev, T. Seyller, K. Horn, and R. Bennewitz, “Friction and dissipation in epitaxial graphene films”, *Phys. Rev. Lett.* **102**, 086102 (2009).
- <sup>89</sup>C. Lee, Q. Li, W. Kalb, X. Liu, H. Berger, R. Carpick, and J. Hone, “Frictional characteristics of atomically thin sheets”, *Science (New York, N.Y.)* **328**, 76–80 (2010).
- <sup>90</sup>E. Thormann, “Negative friction coefficients”, *Nature Materials* **12**, 468–468 (2013).
- <sup>91</sup>O Zwörner, H Hölscher, U. Schwarz, and R Wiesendanger, “The velocity dependence of frictional forces in point-contact friction”, *APPLIED PHYSICS A MATERIALS SCIENCE AND PROCESSING* **66**, S263–S268 (1998).

- <sup>92</sup>R. Guerra, U. Tartaglino, A. Vanossi, and E. Tosatti, “Ballistic nanofriction”, *Nature Materials* **9**, 634–637 (2010).
- <sup>93</sup>H. Tomaç, Z. Guchan, and N. Altun, “How the stiletto heeled shoes which are popularly preferred by many women affect balance and functional skills?”, *Health Care for Women International* **43**, 1–11 (2020).
- <sup>94</sup>K. Gibbs, *Pressure*, (2020) [https://www.schoolphysics.co.uk/age16-19/Mechanics/Statics/text/Pressure\\_index.html](https://www.schoolphysics.co.uk/age16-19/Mechanics/Statics/text/Pressure_index.html).
- <sup>95</sup>F. B. Ltd, *Foot facts*, (2023) <https://www.footbionics.com/Patients/Foot+Facts.html>.